THE UNIVERSITY
OF ADELAIDE
AUSTRALIA

SUB CRUCE LUMEN

Investigation of Passive Control Devices for Potential Application to a Launch Vehicle Structure to Reduce the Interior Noise Levels During Launch

Report for Stage 4
Tasks 1 and 2

July 2004

Prepared For:	AFOSR	Prepared by:	Dr. Carl Q. Howard
Contract Number:	F62562-03-C-0029		Professor Colin H. Hansen
Solicitation Number:	F62562-03-R-0058		Mr. Rick Morgans
			Dr. Anthony C. Zander
		Address:	School of Mechanical Engineering
			The University of Adelaide
			SA 5005
			Australia

Contents

Executive Summary

The work described here is directed at optimising passive vibration and acoustic devices to minimise the transmission of low frequency rocket motor noise into structures that represent launch vehicle fairings. The work was divided into four stages and this report describes the results for the first two sub-tasks in the fourth stage of the work.

In the stage 1 study, the optimal configuration of a Passive Vibro-Acoustic Device (PVAD) mounted to the interior of a small cylinder was investigated. The PVAD consisted of an acoustic absorber and a vibration absorber (Tuned Mass Damper, TMD) in the one device, and it was mounted to a flexible aluminum panel used as the cylinder end cap. A mathematical framework was developed that used the modal analysis results from a finite element model to calculate the interior acoustic pressure and structural vibration levels, using a modal coupling method. The study found that the optimal PVAD design used the TMD essentially as a mass, as the uncoupled resonance frequency of the TMD was just below the upper bound of the frequency band of interest and that the optimal loudspeaker diaphragm configuration was highly lossy so that it reduced the modal amplitude of a single acoustic mode.

The objectives of the Stage 2 task were to transfer the techniques developed in the stage 1 task to the optimisation of structures that more realistically represent real launch vehicles; in particular, a large composite cylinder constructed at Boeing, and a Representative Small Launch Vehicle Fairing (RSLVF). The modal coupling framework was extended to include the effects of the PVADs. A Genetic Algorithm was used to find optimum parameters for the PVADs that would reduce a cost function, the interior acoustic potential energy in this case. It was found that the calculation of the cost function took

an excessive length of time, and attempts were made to reduce the calculation time by reducing the number of modes in the analysis. Vibration and acoustic modes that did not significantly contribute to the acoustic potential energy were removed from the matrices, which decreased the calculation time. However, this action resulted in a reduction in the number of possible optimum configurations where the vibro-acoustic energy would be re-arranged into poor radiating modes.

The results from the Stage 3 tasks were the creation of a distributed computing network using 200 desktop computers. A parallel genetic algorithm was developed for use with the distributed computing network. These two tools were used to optimise the location and parameters of PVADs on a composite cylinder made by Boeing. The time taken to conduct the optimisations was reduced by approximately 25 times compared to using a single computer. It was found that an integer representation of the chromosomes in the genetic algorithm converged to the optimum faster than using a binary string representation.

The work completed in this stage involves the application of the tools developed in the previous stages to the Representative Small Launch Vehicle Fairing (RSLVF). An improved mathematical framework is developed for calculating the vibro-acoustic response of the system, which reduced the calculation time by approximately 50%. This faster technique was used to identify trends on an example problem of a rectangular cavity with a simply supported rectangular plate, which had tuned vibration dampers attached to the plate to reduce the sound transmission into the cavity. The results showed that for a fixed added mass to the plate, the greatest noise reduction was achieved by attaching a large number of light-weight tuned vibration dampers to the plate, compared to a small number of heavy-weight tuned vibration dampers attached to the plate. This also had the advantage that the noise reduction that was achieved was relatively insensitive to the location of the dampers on the plate. This method was also applied to the RSLVF and similar trends were identified as shown in the example problem of the rectangular cavity and plate. The second task in this stage involved developing mathematical tools to analyse multiple degree of freedom tuned vibration dampers that are capable of transmitting

both translational forces and rotational moments to the structure. Optimisations were conducted to determine the noise reduction that could be achieved with these multiple degree of freedom absorbers. The results showed that for the same added mass to the fairing, the same amount of noise reduction was obtained when 20 PVADs with multiple degrees of freedom, and 500 PVADs with a single degree of freedom were used. However, further investigation is required to assess the sensitivity of these solutions to variations in the acoustic excitation of the fairing, which is the subject of a future task in this project. It is hypothesised that the use of a large number of light-weight single degree of freedom absorbers will provide the most robust solution.

Chapter 1

Task 1: RSLVF optimal and sub-optimal performance evaluation

This task was labelled 'Stage 4 Task 1' in the original proposal in which the work statement was as follows.

The design tools developed in stage 3 will be applied to the Representative Scale Launch Vehicle Fairing (RSLVF) model. The reduction of interior noise levels shall be investigated for different design approaches for the RSLVF. Performance of the tools shall be assessed. The investigation shall include the performance of VADs, which represent vibration and acoustic absorbers at the same location, and the possible benefit of separating them shall be investigated.

1.1 Introduction

During the launch of a rocket containing a satellite, high sound pressure levels are generated by the rocket engines, which vibrate and possibly damage the components on the satellite. It has been estimated that 70% of the mass of the satellite is used just to survive the severe launch conditions [1]. It costs approximately $US10,000 per pound to launch objects into space, and hence there are obvious financial benefits that can be realised by making satellites lighter. One of the aims of this project is investigate the application of

light-weight acoustic and vibration devices to the fairing walls to reduce the transmission of sound into the payload bay that contains a satellite.

The worked discussed in the following report was undertaken as a result of the work done by Dr. Steve Griffin of the Air Force Research Lab at Kirtland AFB, New Mexico during his participation in the AFOSR Windows on Science program at the University of Adelaide, South Australia in 1998. The previous work involved an investigation of the application of active feedback control of launch vehicle structural vibration using radiation mode vibration levels as the cost function to minimise interior noise levels and led to the publication of three papers. The small benefit of active control, compared to the passive effect of the un-excited actuators attached to the structure has been the impetus behind the work conducted here, which is directed at optimising the passive effect of vibration reducing devices. The current work was divided into four stages and this report is primarily intended to provide the results for the first two tasks of the fourth stage of the work.

In previous stages of this project, mathematical tools were developed to determine optimum parameters for the locations, stiffness, mass and damping of Helmholtz Resonators (HRs) and Tuned Mass Dampers (TMDs) attached to the circumference of a rocket fairing. The combination of these two devices to control the structural vibration and acoustic response is called a Passive Vibro-Acoustic Device (PVAD). Finite element models were used in Stages 2 and 3A to represent the Boeing cylinder, which was made from a composite material. The same mathematical tools can be used to analyse the Representative Scale Launch Vehicle Fairing (RSLVF). A Nastran finite element model, which was supplied by Boeing SVS, was re-interpreted into the ANSYS finite element software package and modal analyses were conducted to extract the in-vacuo mode shapes and resonance frequencies for the structure and acoustic cavity. Comparisons of the mode shapes predicted using Nastran and ANSYS were presented in the report for Stage 2 of this project. These mode shapes and resonance frequencies were used by the Matlab modal coupling software to calculate the response of the coupled structural cavity system to a specified

acoustic input.

The purpose of the current task (Stage 4 Task 1) is to apply the tools that were developed to analyse the Boeing cylinder, to the analysis of the Representative Scale Launch Vehicle Fairing (RSLVF). This is described in details in the sections to follow.

Section 1.2 describes the development of an alternative mathematical model to describe the coupled vibro-acoustic response of a structure-cavity system. The reformulation of the equations reduced the calculation time by about half compared to the mathematical models developed in previous tasks.

An optimisation technique using a genetic algorithm is used to determine parameters that results in the minimisation of the global sound field inside the cavity. This technique is fully described Stage 3A [2] and Stage 3B [3]. The genetic algorithm was adapted for use on a distributed computing network, where unused desktop computers in a computing pool were used by the genetic algorithm to evaluate the sound field in the cavity. This distributed computing network of about 200 desktop computers had a measured computational speed of about 100 GigaFLOPS, and enabled the optimisations to be completed in a reasonable time frame.

Sections 1.3 to 1.7 describe the mathematical derivation of the equations of motion for the Tuned Mass Dampers, the Helmholtz resonators, the integration of the TMDs and the HRs into the coupled vibro-acoustic equations, and an example to verify that the improved mathematical model calculates the same results as method described in Stage 3A, only in a shorter amount of time.

Section 1.8 consists of an example problem to demonstrate the vibro-acoustic theory and the genetic algorithm optimisation. These tools were used to determine the parameters that would minimise the sound pressure level inside a rectangular cavity that had a rectangular plate attached it, and TMDs attached to the plate to reduce the transmission of sound into the cavity. The genetic algorithm was used to optimise the locations, stiffness, and damping of the TMDs on the plate. The mass that was added to the plate from the TMDs was kept constant at 10% of the weight of the rectangular panel, and

it was evenly divided amongst the TMDs. The results showed that the lowest acoustic energy was obtained by using a large number of light-weight TMDs attached to the plate, compared to using a few heavy-weight TMDs. The light-weight solution also had the advantage that it was less sensitive to loading conditions than the heavy-weight solution.

Section 1.9 contains the results of the optimisation of the PVADs applied to the RSLVF. The hypothesis was that the same trends that were seen in the results from the analysis of the rectangular cavity and rectangular plate should be seen in the analysis of the RSLVF. The results showed that indeed the same trends occurred; that is using a large number of light-weight PVADs achieved greater noise reduction than using few heavy weight PVADs.

1.2   Coupled Structural Acoustic Equations

The following sections describe an improved mathematical framework for calculating the coupled vibro-acoustic response of a structural-cavity system. The improved formulation reduces the time taken to calculate the acoustic potential energy inside the cavity by about half, compared to the formulation used in the previous stages of this project. The equations that describe the coupled vibro-acoustic system are presented in this section. The equations of motion for the TMDs are developed in Section 1.3 and then incorporated into the structural response. Section 1.4 describes the equations that describe the effect of HRs on the acoustic field, which are incorporated into the equations that describe the acoustic field within the cavity. Section 1.5 describes the re-assembly of the structural and acoustic equations into the coupled vibro-acoustic response, which incorporates the effect of the TMDs and the HRs.

The theory that was developed in Stage 3A [2] to describe the coupled response of passive vibro-acoustic dampers attached to a structural acoustic system was based on the work by Cazzolato [4]. As suggested in Stage 3B [3], there were indications that reformulation of the theory to follow the work of Fahy [5] could lead to a reduction in the time taken to calculate the fully coupled vibro-acoustic response. A typical calculation of

the response of the Boeing cylinder with 30 PVADs attached to the structure would take approximately 6 minutes on a Pentium 4, 3GHz desktop computer using the theory from Stage 3A. When the reformulated theory was used, the time taken to calculate the same response was just under 3 minutes. The reason for the reduction in the calculation time is likely due to the reduction in the number of matrix multiplications required at each frequency step, and also to the formation of symmetric matrices to describe the coupled response.

Fahy [5, p249] describes equations for the coupled structural-acoustic response of a system in terms of the summation of structural and acoustic mode shapes. The structural displacement is described in terms of a summation over the *in vacuo* normal modes as

$$w(\mathbf{r}_s) = \sum_{p=1}^{\infty} w_p \, \phi_p(\mathbf{r}_s) \tag{1.1}$$

where ϕ_p is the structural mode shape of the pth mode, $\mathbf{r}_s$ is an arbitrary location on the surface of the structure, and w_p is the modal participation factor of the pth mode.

The acoustic pressure is described in terms of a summation of the acoustic modes of the fluid volume with rigid boundaries as

$$p(\mathbf{r}) = \sum_{n=0}^{\infty} p_n(t) \, \psi_n(\mathbf{r}) \tag{1.2}$$

where ψ_n is the acoustic mode shape of the nth mode, $\mathbf{r}$ is an arbitrary location within the volume of fluid, and p_n is the modal participation factor of the nth mode.

The equation for the coupled response of the structure is given by [5, Eq. (6.27)]

$$\ddot{w}_p + \omega_p^2 \, w_p = \frac{S}{\Lambda_p} \sum_n p_n C_{np} + \frac{F_p}{\Lambda_p} \tag{1.3}$$

where ω_p are the structural resonance frequencies, Λ_p are the modal masses, F_p are the modal forces applied to the structure, S is the surface area of the structure, and C_{np} is the dimensionless coupling coefficient, namely the integral of the product of the structural

(ϕ_p) and acoustic (ψ_n) mode shape functions over the surface of the structure, given by

$$C_{np} = \frac{1}{S} \int_S \psi_n(\mathbf{r}_s)\, \phi_p(\mathbf{r}_s)\, dS \tag{1.4}$$

The equation for the coupled response of the fluid is given by [5, Eq. (6.28)]

$$\ddot{p}_n + \omega_n^2 p_n = -\left(\frac{\rho_0 c^2 S}{\Lambda_n}\right) \sum_p \ddot{w}_p C_{np} + \left(\frac{\rho_0 c^2}{\Lambda_n}\right) \dot{Q}_n \tag{1.5}$$

where ω_n are the resonance frequencies of the cavity, ρ_0 is the density of the fluid, c is the speed of sound in the fluid, Λ_n is the modal volume, and Q_n is the source strength with units of volume velocity (hence $\dot{Q}_n$ has units of volume acceleration).

1.3   Equations of Motion for the Tuned Mass Dampers

Tuned mass dampers can be used to alter the vibration response of a structure by reducing the vibration level, or cause the structure to vibrate in a different way by re-arranging the modal responses of the structure.

This section describes the equations of motion for a single degree of freedom Tuned Mass Damper, and incorporates the effect of the damper into the vibration response of the structure.

The equations that describe the effect of a Tuned Mass Damper attached to a structure are similar to those described in Stage 3A [2], except that the response of the structure is described in terms of displacement instead of velocity, and the impedance of the structure is presented differently, using Eq. (1.3) as a basis.

A model of a TMD is shown in Figure 1.1, where m_1 is the mass of the damper, k_1 is the stiffness, F_1 is the harmonic force directly applied to the mass, which is typically zero, and F_c is the force at the attachment point between the spring and the structure. Note that at this stage, the model does not have any damping included; however damping terms are added later by using a complex stiffness. The equations of motion for the TMD
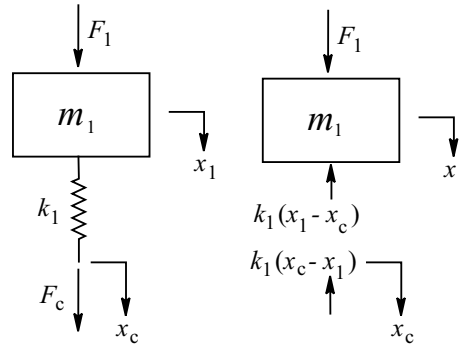
FIG. 1.1: Model of a one degree of freedom spring-mass system, to be used as a Tuned Vibration Damper (TMD).

can be written succinctly in matrix form as

$$
\begin{bmatrix} k_1 - m_1\omega^2 & -k_1 \\ -k_1 & k_1 \end{bmatrix} \begin{bmatrix} x_1 \\ x_c \end{bmatrix} = \begin{bmatrix} F_1 \\ F_c \end{bmatrix}
\tag{1.6}
$$

where k_1 is the spring stiffness, m_1 is the mass, F_1 is the force applied directly to the TMD which is usually $F_1 = 0$, ω is the driving frequency in radians / sec, x_1 is the displacement of the TMD, x_c is the displacement of the connection of the isolator to the structure, and F_c is the force applied by the structure to the TMD, which is equal and opposite to the force from the spring.

One can assume that at the point of attachment, the displacement of the structure and the position of the end of the spring are the same. If the dynamics of the structure are introduced into Eq. (1.6) by using the theory from section 1.2, then the equations of motion for multiple TMDs attached to a structure can be written as

$$
\ddot{w}_p + \omega_p^2\, w_p = \frac{S}{\Lambda_p}\sum_n p_n C_{np} + \frac{F_p}{\Lambda_p}
$$
$$
+ \frac{1}{\Lambda_p}\left\{[\psi_J]^{\mathrm{T}} k_J^{\mathrm{TMD}}(x_J^{\mathrm{TMD}} - [\psi_J]w_p)\right\}
\tag{1.7}
$$

for the equation of motion of the structure and

$$
-\omega^2 m_J^{\mathrm{TMD}} x_J^{\mathrm{TMD}} + k_J^{\mathrm{TMD}}(x_J^{\mathrm{TMD}} - [\psi_J]w_p) = 0
\tag{1.8}
$$

for the equation of motion of the TMD. Eqs. (1.7) and (1.8) can be written in matrix form as (neglecting the C_{np} term for the vibro-acoustic coupling for the moment)

$$
\begin{bmatrix}
k_J^{\text{TMD}} - \omega^2 m_J^{\text{TMD}} & -k_J^{\text{TMD}}[\psi_J] \\
-[\psi_J]^{\text{T}} k_J^{\text{TMD}} & \Lambda_p(\omega_p^2 - \omega^2) + [\psi_J]^{\text{T}} k_J [\psi_J]
\end{bmatrix}
\begin{bmatrix}
x_J^{\text{TMD}} \\
w_p
\end{bmatrix}
=
\begin{bmatrix}
0 \\
F_p
\end{bmatrix}
\tag{1.9}
$$

where $[\boldsymbol{\psi}_J]$ is the structural mode shape vector evaluated at the Jth connection point of the TMD to the structure, and $^{\text{T}}$ is the matrix transpose operator. Note that the matrix $[\boldsymbol{\Psi}]$ contains all the mode shapes for all the nodes and has dimensions $(N_{\text{s nodes}} \times N_s)$, the number of structural nodes $\times$ the number of structural modes. Hence, each row of the matrix contains N_s entries for the normal structural displacement for each mode, and so the vector $[\boldsymbol{\psi}_1]$ has dimensions $(1 \times N_s)$. Eq. (1.9) can be extended to the general case, where there are multiple TMDs that each have multiple degrees of freedom, as shown in Refs. [6, 7].

1.4 Equations of Motion for the Helmholtz Resonators

A Helmholtz resonator is a passive acoustic device that can be used to reduce the sound pressure level inside a cavity. The device consists of a compliant volume and a neck that connects the compliant volume to the cavity. This section describes the equations for the acoustic response of a Helmholtz resonator and integrates them with the acoustic response of a cavity. In a similar way that tuned mass dampers can alter the vibration response of a structure, Helmholtz resonators can also alter the acoustic response of a cavity. They can reduce the sound pressure level inside the cavity, or alter the acoustic response by modal re-arrangement.

A Helmholtz resonator can be thought of as a piston attached to a cavity, with the dynamics of an equivalent mass-spring system, as shown in Figure 1.2.

The equation for the coupled response of the fluid, described in Eq. (1.5), includes a term for the application of acoustic sources Q_n. The modal volume velocity sources inside the cavity comprise the point sources from Helmholtz resonators, $\mathbf{Q}_J^{\text{HR}}$, and from internal
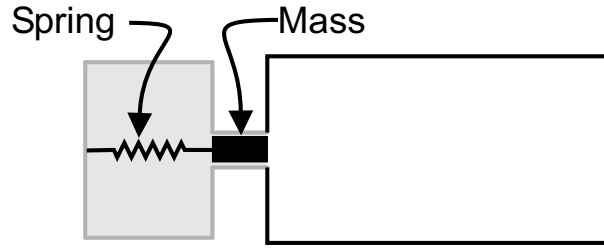
FIG. 1.2: A Helmholtz resonator attached to a cavity can be thought of as a mass-spring system.

sources such as speakers or other noise generating devices $\mathbf{Q}_K^{\text{int}}$; hence the total volume velocity inside the cavity is given by

$$\mathbf{Q}^{\text{T}} = \sum_{J=1}^{N_{\text{HR}}} \mathbf{Q}_J^{\text{HR}} + \sum_{K=1}^{N_{\text{int}}} \mathbf{Q}_K^{\text{int}} \tag{1.10}$$

where N_{HR} is the number of Helmholtz resonators, and N_{int} is the number of interior acoustic sources. However in this case, there are no interior acoustic sources. All the acoustic excitation occurs on the exterior of the structure. These terms would only be used if there were loudspeakers placed in the cavity, such as would be used in an active noise control system, or in experimental testing to determine the acoustic characteristics of the cavity.

The equation of motion for the simple mass-spring system shown in Figure 1.3 is

$$-\omega^2 m_J^{\text{HR}} x_J^{\text{HR}} = F_J^{\text{HR}} - k_J^{\text{HR}} x_J^{\text{HR}} \tag{1.11}$$

where F_J^{HR} is the force applied by the back pressure from the cavity, k_J^{HR} is the equivalent spring stiffness of the compliant volume, and m_J^{HR} is the equivalent mass of the volume of fluid inside the neck of the resonator. These terms are given by [8]

$$F = P_J A_J^{\text{HR}} \tag{1.12}$$

$$k = \frac{\rho c^2 A_{\text{neck}}^2}{V_{\text{HR}}} \tag{1.13}$$

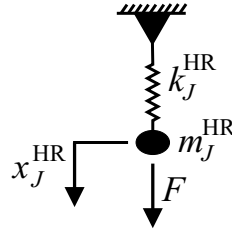$$m = \rho A_{\text{neck}} L_{\text{eff}} \tag{1.14}$$

FIG. 1.3: A Helmholtz resonator attached to a cavity can be thought of as a mass-spring system.

where A_J^{HR} is the area associated with the node attaching the spring to the acoustic cavity, P_J is the nodal pressure at the attachment point, V_{HR} is the volume of the Helmholtz resonator, A_{neck} is the cross sectional area of the neck, L_{eff} is the effective length of the neck given by $L_{\text{eff}} = L_{\text{neck}} + 1.7a$, where L_{neck} is the length of the neck, and a is the radius of the neck.

The volume acceleration from the Helmholtz resonator is given by

$$\dot{\mathbf{Q}}_J^{\text{HR}} = -\omega^2 A_J^{\text{HR}}[\boldsymbol{\phi}_J]^{\text{T}} x_J^{\text{HR}} \tag{1.15}$$

Hence the equation for the response of the fluid can be written as

$$\ddot{p}_n + \omega_n^2 p_n = -\left(\frac{\rho_0 c^2 S}{\Lambda_n}\right) \sum_p \ddot{w}_p C_{np}$$
$$+ \left(\frac{\rho_0 c^2}{\Lambda_n}\right) \left(\dot{Q}_n - \omega^2 A_J^{\text{HR}}[\boldsymbol{\phi}_J]^{\text{T}} x_J^{\text{HR}}\right) \tag{1.16}$$

and the equation of motion for the HR can be written as

$$-m_J^{\text{HR}}\omega^2 + k_J^{\text{HR}}(x_J^{\text{HR}} - A_J^{\text{HR}}\boldsymbol{\phi}_J) = 0 \tag{1.17}$$

If the coupling term C_{np} is neglected for now, then Eqs. (1.16) and (1.17) can be

written in matrix form as

$$\begin{bmatrix} k_J^{\mathrm{HR}} - \omega^2 m_J^{\mathrm{HR}} & -A_J^{\mathrm{HR}}[\phi_J] \\[2ex] -\omega^2 A_J^{\mathrm{HR}}[\phi_J]^{\mathrm{T}} & \dfrac{\Lambda_n}{\rho_0 c^2}(\omega_n^2 - \omega^2) \end{bmatrix} \begin{bmatrix} x_J^{\mathrm{HR}} \\[2ex] p_n \end{bmatrix} = \begin{bmatrix} 0 \\[2ex] \dot{Q}_n \end{bmatrix} \tag{1.18}$$

1.5   Equations of Motion for the Fully Coupled System

The equations for the fully coupled vibro-acoustic system, including the effects of the TMDs and HRs can be formed into a matrix equation using Eqs. (1.7), (1.8), (1.16), and (1.17) as

$$\begin{bmatrix} \begin{bmatrix} \mathbf{A}_{11} & \mathbf{A}_{12} \\ \mathbf{A}_{21} & \mathbf{A}_{22} \end{bmatrix} & \begin{matrix} \mathbf{0} & \mathbf{0} \\ \mathbf{0} & \mathbf{A}_{24} \end{matrix} \\ \begin{matrix} \mathbf{0} & \mathbf{0} \\ \mathbf{0} & \mathbf{B}_{42} \end{matrix} & \begin{bmatrix} \mathbf{B}_{33} & \mathbf{B}_{34} \\ \mathbf{B}_{43} & \mathbf{B}_{44} \end{bmatrix} \end{bmatrix} \begin{bmatrix} \mathbf{x}^{\mathrm{TMD}} \\ \mathbf{w}_p \\ \mathbf{x}^{\mathrm{HR}} \\ \mathbf{p}_n \end{bmatrix} = \begin{bmatrix} \mathbf{0} \\ \mathbf{F}_p \\ \mathbf{0} \\ \dot{\mathbf{Q}}_n \end{bmatrix} \tag{1.19}$$

where $\mathbf{A}_{11}$ is a $(N_{\mathrm{TMD}} \times N_{\mathrm{TMD}})$ matrix that has elements only on the main diagonal of

$$\mathbf{A}_{11} = \begin{bmatrix} k_1^{\mathrm{TMD}} - m_1^{\mathrm{TMD}}\omega^2 & & \\ & \ddots & \\ & & k_J^{\mathrm{TMD}} - m_J^{\mathrm{TMD}}\omega^2 \end{bmatrix} \tag{1.20}$$

$\mathbf{A}_{12}$ is a $(N_{\mathrm{TMD}} \times N_{\mathrm{s}})$ matrix given by

$$\mathbf{A}_{12} = \begin{bmatrix} -k_1^{\mathrm{TMD}}\boldsymbol{\psi}_{11} & \cdots & -k_1^{\mathrm{TMD}}\boldsymbol{\psi}_{1N_s} \\ \vdots & \ddots & \vdots \\ -k_J^{\mathrm{TMD}}\boldsymbol{\psi}_{J1} & \cdots & -k_J^{\mathrm{TMD}}\boldsymbol{\psi}_{JN_s} \end{bmatrix} \tag{1.21}$$

$\mathbf{A}_{21}$ is a $(N_{\text{s}} \times N_{\text{TMD}})$ matrix given by

$$\mathbf{A}_{21} = \begin{bmatrix} -[\boldsymbol{\psi}_{11}]^{\text{T}} k_1^{\text{TMD}} & \cdots & -[\boldsymbol{\psi}_{J1}]^{\text{T}} k_J^{\text{TMD}} \\ \vdots & \ddots & \vdots \\ -[\boldsymbol{\psi}_{1N_s}]^{\text{T}} k_1^{\text{TMD}} & \cdots & -[\boldsymbol{\psi}_{JN_s}]^{\text{T}} k_J^{\text{TMD}} \end{bmatrix} \tag{1.22}$$

$\mathbf{A}_{22}$ is a $(N_{\text{s}} \times N_{\text{s}})$ symmetric matrix given by

$$\mathbf{A}_{22} = \Lambda_p(\omega_p^2 - \omega^2) + [\boldsymbol{\psi}_J]^{\text{T}} k_J^{\text{TMD}} [\boldsymbol{\psi}_J] \tag{1.23}$$

$\mathbf{B}_{33}$ is a $(N_{\text{HR}} \times N_{\text{HR}})$ matrix that has entries only along the diagonal of

$$\mathbf{B}_{33} = \begin{bmatrix} k_1^{\text{HR}} - m_1^{\text{HR}}\omega^2 & & \\ & \ddots & \\ & & k_J^{\text{HR}} - m_J^{\text{HR}}\omega^2 \end{bmatrix} \tag{1.24}$$

$\mathbf{B}_{34}$ is a $(N_{\text{HR}} \times N_{\text{c}})$ matrix given by

$$\mathbf{B}_{34} = \begin{bmatrix} -A_1^{\text{HR}}\boldsymbol{\phi}_{11} & \cdots & -A_1^{\text{HR}}\boldsymbol{\phi}_{1N_c} \\ \vdots & \ddots & \vdots \\ -A_J^{\text{HR}}\boldsymbol{\phi}_{J1} & \cdots & -A_J^{\text{HR}}\boldsymbol{\phi}_{JN_c} \end{bmatrix} \tag{1.25}$$

$\mathbf{B}_{43}$ is a $(N_{\text{c}} \times N_{\text{HR}})$ matrix given by

$$\mathbf{B}_{43} = \begin{bmatrix} -\omega^2 A_1^{\text{HR}}[\boldsymbol{\phi}_{11}]^{\text{T}} & \cdots & -\omega^2 A_J^{\text{HR}}[\boldsymbol{\phi}_{J1}]^{\text{T}} \\ \vdots & \ddots & \vdots \\ -\omega^2 A_1^{\text{HR}}[\boldsymbol{\phi}_{1N_c}]^{\text{T}} & \cdots & -\omega^2 A_J^{\text{HR}}[\boldsymbol{\phi}_{JN_c}]^{\text{T}} \end{bmatrix} \tag{1.26}$$

$\mathbf{B}_{44}$ is a $(N_{\text{c}} \times N_{\text{c}})$ matrix that has entries only along the diagonal of

$$\mathbf{B}_{44} = \frac{\Lambda_n}{\rho_0 c^2} (\omega_n^2 - \omega^2) \tag{1.27}$$

The two remaining elements account for the cross coupling between structure and fluid. $\mathbf{A}_{24}$ is a $(N_\mathrm{s} \times N_\mathrm{c})$ matrix given by

$$\mathbf{A}_{24} = -S\,\mathbf{C}_{np} \tag{1.28}$$

$\mathbf{B}_{42}$ is a $(N_\mathrm{c} \times N_\mathrm{s})$ matrix given by

$$\mathbf{B}_{42} = -\omega^2 S\,[\mathbf{C}_{np}]^\mathrm{T} \tag{1.29}$$

One can see that the matrix in Eq. (1.19) is almost symmetric. The properties of the sub-elements are

$$\mathbf{A}_{21} = \quad [\mathbf{A}_{12}]^\mathrm{T} \tag{1.30}$$

$$\mathbf{B}_{43} = \omega^2 [\mathbf{B}_{34}]^\mathrm{T} \tag{1.31}$$

$$\mathbf{B}_{42} = \omega^2 [\mathbf{A}_{24}]^\mathrm{T} \tag{1.32}$$

Hence if the sub-elements on the fourth row of the matrix in Eq. (1.19) are divided by ω^2 then the matrix will be symmetric.

1.6   Impedance Method

This section describes an algebraic re-arrangement of the matrices described in the previous sections, which results in a reduction in the size of the matrices, which in turn reduces the time taken to calculate the vibro-acoustic response.

Simplification of Eq. (1.19) is possible by re-arrangement of the first and third lines. The mass elements in the TMDs are not driven by external forces and hence the first line equates to zero. Similarly, the Helmholtz resonators are not excited by volume velocity sources, and hence the third line equates to zero. These two lines can be re-arranged and back substituted to reduce the size of the matrix. The first line can be re-arranged to

solve for the displacement of the tuned mass dampers as

$$\mathbf{x}^{\mathrm{TMD}} = -(\mathbf{A}_{11})^{-1}\,\mathbf{A}_{12}\mathbf{w}_p \tag{1.33}$$

which can be substituted into the second line of Eq. (1.19) to give

$$\left[-\mathbf{A}_{21}(\mathbf{A}_{11})^{-1}\,\mathbf{A}_{12} + \mathbf{A}_{22}\right]\mathbf{w}_p + \mathbf{A}_{24}\mathbf{p}_n = \mathbf{F}_p \tag{1.34}$$

The third line in Eq. (1.19) can be re-arranged for the displacement of the Helmholtz resonators as

$$\mathbf{x}^{\mathrm{HR}} = -(\mathbf{B}_{33})^{-1}\,\mathbf{B}_{34}\mathbf{p}_n \tag{1.35}$$

which can be substituted into the fourth line of Eq. (1.19) to give

$$\left[\mathbf{B}_{42}\right]\mathbf{w}_p + \left[-\mathbf{B}_{43}(\mathbf{B}_{33})^{-1}\,\mathbf{B}_{34} + \mathbf{B}_{44}\right]\mathbf{p}_n = \dot{\mathbf{Q}}_n \tag{1.36}$$

Eqs. (1.34) and Eq. (1.36) can be represented in matrix form as

$$\begin{bmatrix} \left[-\mathbf{A}_{21}(\mathbf{A}_{11})^{-1}\,\mathbf{A}_{12} + \mathbf{A}_{22}\right] & \mathbf{A}_{24} \\ \mathbf{B}_{42} & \left[-\mathbf{B}_{43}(\mathbf{B}_{33})^{-1}\,\mathbf{B}_{34} + \mathbf{B}_{44}\right] \end{bmatrix} \begin{bmatrix} \mathbf{w}_p \\ \mathbf{p}_n \end{bmatrix} = \begin{bmatrix} \mathbf{F}_p \\ \dot{\mathbf{Q}}_n \end{bmatrix} \tag{1.37}$$

1.7 Verification

The model described in section 1.5 was realised in Matlab and compared with the model developed in Stage 3A. The acoustic potential energy and the structural kinetic energy were compared for both methods to ensure that they gave the same results.

The Acoustic Potential Energy (APE) is calculated in terms of the modal pressure amplitudes as (see Appendix D.5 in Ref. [2])

$$E_p = \sum_{i=1}^{\infty} \Lambda |p_i|^2 \tag{1.38}$$

$$= \mathbf{p}^{\mathrm{H}}\mathbf{\Lambda}\mathbf{p} \tag{1.39}$$

where Λ is a $(N_a \times N_a)$ diagonal matrix of which the diagonal terms are

$$\Lambda(i,i) = \frac{\Lambda_i}{4\rho_0 c_0^2} \tag{1.40}$$

where Λ_i is the modal volume of the ith cavity mode.

The structural kinetic energy can be calculated in a similar manner. The structural kinetic energy is calculated as [5, p278]

$$E_k = \frac{1}{2}[\dot{q}]^{\mathrm{T}}[\mathbf{M}][\dot{q}] \tag{1.41}$$

where $[\dot{q}]$ is the velocity of an element, and $[\mathbf{M}]$ is the mass of an element. This can be written in terms of the structural modal participation factors as

$$E_k = \frac{\omega^2}{2}[w_p]^{\mathrm{T}}\Lambda_p[w_p] \tag{1.42}$$

The model used for the comparison of the old method (described in Stage 3A [2]) and the new method (described in Section 1.5) is the Boeing cylinder with 30 PVADs attached at 'optimum' locations that were determined by using a genetic algorithm over 18,000 iterations.

The results presented below should be identical to those shown in Ref. [2, Fig. 5.6, p41] and inspection of Figures 1.4 and 1.5 show that indeed the acoustic potential energy and structural kinetic energy calculated using the method described in Stage 3A and the two new methods are identical. The main difference between the three methods is the time to calculate the responses. Table 1.1 lists the time taken to calculate the response using the three methods.

These results show that the time taken using the impedance method described in Section 1.6 is 2.5 times less than the method described in the Stage 3A report.

Comparison of different calculation methods
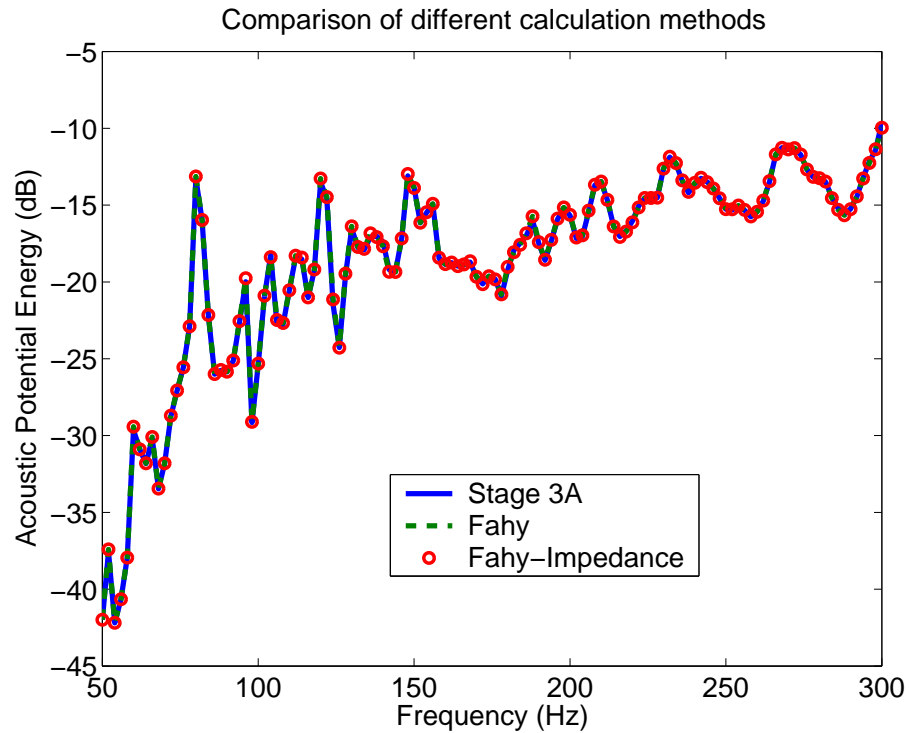
FIG. 1.4: Comparison of the acoustic potential energy inside the cylinder using the method from Stage 3A, Fahy's method described in Section 1.5, and the impedance method described in Section 1.6.

Comparison of different calculation methods
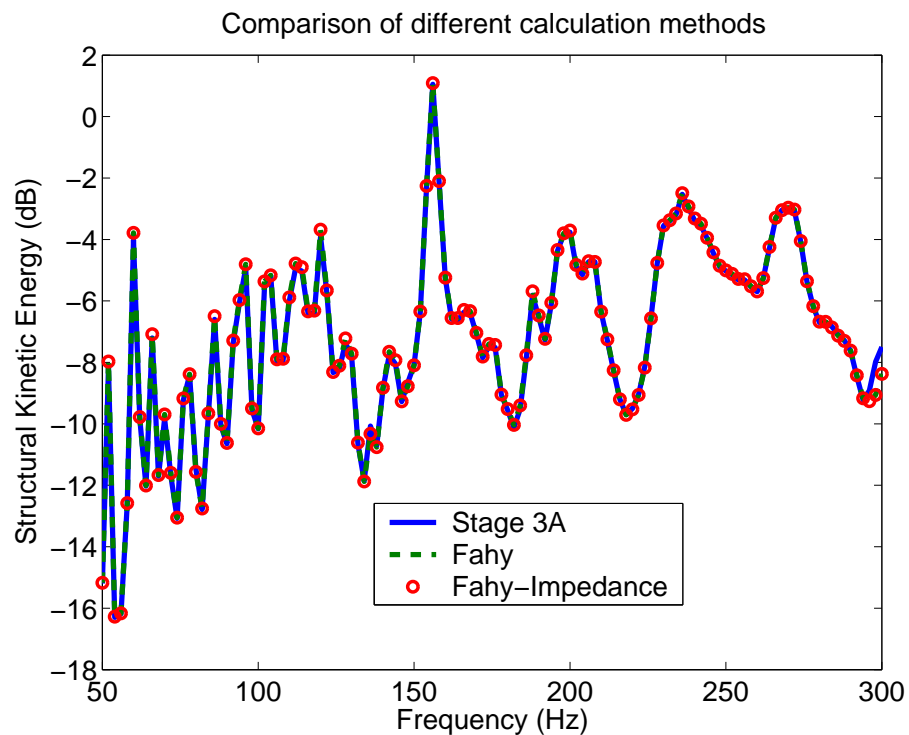
FIG. 1.5: Comparison of the structural kinetic energy inside the cylinder using the method from Stage 3A, Fahy's method described in Section 1.5, and the impedance method described in Section 1.6

Table 1.1: Time taken to calculate the cost function.

Method	Time	Speed Improvement Factor
Stage 3A	349s	1
Fahy	171s	2.0
Fahy-Impedance	137s	2.5

1.8 Rectangular Box

The algorithm described in the previous section was used to investigate the noise reduction into a rectangular cavity through a rectangular plate, with the application of Tuned-Mass-Dampers (TMDs) to the rectangular plate. One of the outcomes from Stage 3A was the hypothesis that for a fixed added mass distributed amongst numerous PVADs, better noise reduction could be achieved that would be less sensitive to the placement of the PVADs, than a few judiciously placed PVADs. The work in this section tests this hypothesis.

Figure 1.6 shows an ANSYS finite element model of a rectangular box with dimensions $0.5 \times 0.3 \times 1.1$ m, and a simply supported rectangular plate attached on one side with dimensions $0.5 \times 0.3 \times 0.001$m.

The load on the plate was a harmonic force of 1N applied at each node, in a direction normal to the plate surface ($F_z = 1$N).

A semi-synchronous genetic algorithm [2] was used to optimise the location, stiffness, and damping of tuned mass dampers attached to the plate. The genetic algorithm used an integer representation for the chromosomes [2, 3]. The total added mass of the tuned mass dampers was set at 10% of the mass of the plate, which was 0.12kg. The mass of each tuned mass damper was divided equally by the total mass budget. Hence for 20 TMDs, each TMD weighed $0.12/20 = 0.006$kg.

The modal analyses of the structural and acoustic spaces was conducted using ANSYS for 100 structural modes and 300 acoustic modes. The first 10 structural and acoustic modes are listed in Table 1.2.
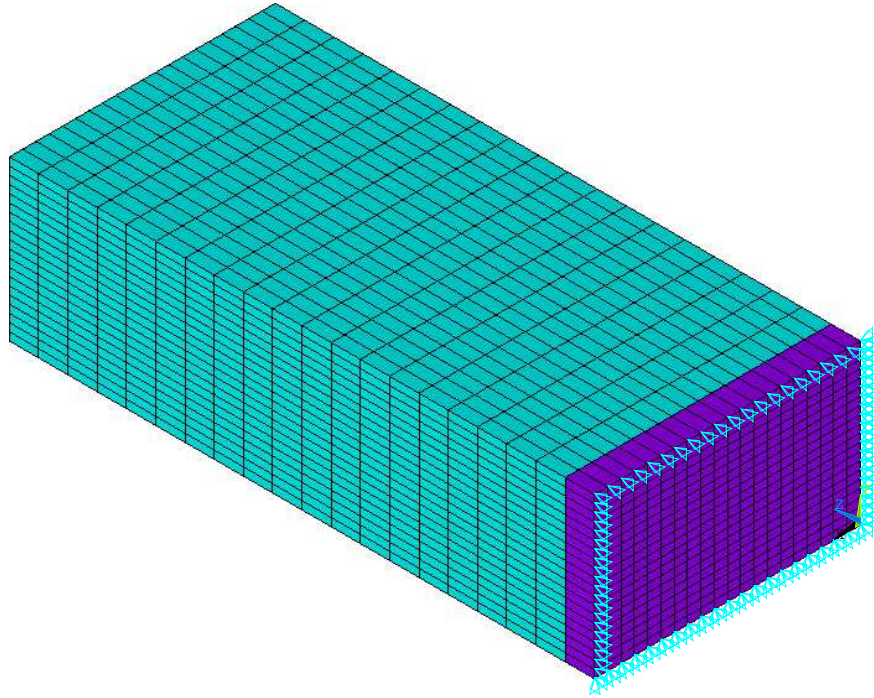
FIG. 1.6: ANSYS finite element model of a rectangular box with rigid walls and a simply supported rectangular plate.

Table 1.2: Structural and acoustic resonance frequencies of the rectangular enclosure with the rectangular plate.

Mode No.	Structural (Hz)	Acoustic (Hz)
1	110	0
2	198	156
3	343	314
4	353	344
5	440	378
6	548	466
7	584	473
8	757	574
9	786	585
10	811	595

1.8.1 Optimisations

Optimisations were conducted for the cases where 1, 5, 10, 20, and 100 TMDs were attached to the rectangular plate. Several optimisations were conducted for each case. The initial conditions for each optimisation is generated randomly and then the genetic algorithm is used to optimise the parameters. Table 1.3 lists the number of times each optimisation was conducted, and the number of cost function evaluations that were involved for each optimisation.

Table 1.3: The number of times each optimisation was conducted, and the number of cost function evaluations for each optimisation.

No. of TMDs	No. of Optimisations	No. of Cost Function Evals
1	10	2,400
5	10	8,000
10	10	18,000
20	10	24,000
100	3	150,000

Table 1.4 lists the range of allowable values for the parameters that were optimised. For each optimisation there were 50 individuals in the population.

Table 1.4: TMD parameter range for the optimisation of the rectangular cavity.

TMD parameter	Min	Max	No. of Values	Comment
TMD position	1	441	441	Nodes on the plate
Mass-spring frequency	11	510	500	[Hz]
Mass-spring damping (η)	0.01	0.25	10	

1.8.2 Results for Optimisation of 1, 5, 10, 20 and 100 TMDs

Figures 1.7 to 1.35 show the results of the optimisation obtained using the genetic algorithm. The results are grouped in sets for 1, 5, 10, 20, and 100 TMDs attached to the structure, with five figures for each set.

Figures 1.7, 1.13, 1.19, 1.25, and 1.31 show the acoustic potential energy versus frequency for the cases where there are no TMDs attached to the plate and the best result achieved at the end of the optimisation with TMDs attached to the plate. The equivalent resonance frequencies of the TMDs are also plotted for the case when no TMDs are attached to the plate. The equivalent resonance frequency of the TMD is calculated as the square root of the optimised stiffness divided by the mass of the TMD. This curve can be used to examine the change in the acoustic potential energy due to application of TMDs.

The typical result for the application of a TMD, which is tuned to a structural resonance frequency, is that the vibration mode is 'split', resulting in the generation of two new resonance frequencies [9, 10].

The results from Active Structural Acoustic Control research indicate that often better noise reduction can be achieved if the TMDs are 'de-tuned' from structural resonance frequencies [11–15]. This result is clearly demonstrated in Figure 1.7, where the equivalent resonance frequency of the TMD is approximately 170Hz, and the acoustic resonance frequency is approximately 160Hz (see Table 1.2). The mode "splitting" phenomena can be seen as there are two new peaks at about 150Hz and 190Hz.

The mode splitting phenomena is also seen in Figure 1.13, where the TMD that has an equivalent resonance frequency at approximately 90Hz has generated two additional damped vibration modes at approximately 70Hz and 110Hz.

The results presented in Figure 1.13 for 5 TMDs attached to the plate show that three of the TMDs are used to reduce the peak in the acoustic potential energy at 160Hz. The effect of one TMD, which generates two additional peaks in the response, is mitigated by the additional two TMDs, which have similar equivalent resonance frequencies. The overall effect is that the response is 'smeared' over a frequency range, rather than generating distinct peaks in the response. This is the first indication of a 'fuzzy' structural response [16–23]. Similar trends can be seen for the cases of 10, 20, and 100 TMDs in Figures 1.19, 1.25, and 1.31, respectively.

As the number of TMDs increases, the number of TMDs that become associated with

a peak in the response also increases. Figures 1.8, 1.14, 1.20, 1.26, and 1.32 show the equivalent resonances for the cases of 1, 5, 10, 20, and 100 TMDs, respectively. Figure 1.32 shows three distinct clusters of TMDs. The clustering can also be seen in the graphs of the results for 5, 10, and 20 TMDs. Note that the analysis frequency range is between 0-400Hz. The results for multiple TMDs (i.e. excluding the case of a single TMD) have at least one TMD that has an equivalent resonance frequency greater than 400Hz. Even though the equivalent resonance frequencies of the TMDs are outside the analysis frequency range, they still affect the response within the analysis frequency range. These results show repeatability between individual optimisations. This is an encouraging sign that the optimisation has converged to a global minimum, as the initial conditions for each optimisation are random, yet the final results are similar.

Figures 1.9, 1.15, 1.21, 1.27, and 1.33 show the locations of the TMDs on the 0.5×0.3m rectangular plate for 1, 5, 10, 20 and 100 TMDs, respectively. The diameter of the circles shown in the figures are proportional to number of TMDs at each node. In general, it can be seen that the locations of the TMDs tend to cluster around the centre of the plate.

Figures 1.10, 1.16, 1.22, 1.28, and 1.34 show the evolution of the optimisations for 1, 5, 10, 20 and 100 TMDs, respectively. Not surprisingly, as the number of TMDs increases, the number of iterations required to reach an optimum solution also increases. In addition, as the number of TMDs increases, the optimal acoustic potential energy becomes lower. This trend is further discussed later in this report.

Figures 1.11, 1.17, 1.23, 1.29, and 1.35 show the acoustic potential energy in the rectangular cavity for all optimisations for 1, 5, 10, 20 and 100 TMDs, respectively (whereas Figures 1.7, 1.13, 1.19, 1.25, and 1.31 just show the best result). These figures show that at the end of each of the optimisations, the acoustic potential energy spectra within the cavity have different shapes in the off-resonance regions; however the total acoustic potential energy has converged to a similar minimum. This means that there are multiple feasible solutions that yield the same total acoustic potential energy.

Figures 1.12, 1.18, 1.24, 1.30, and 1.36 show the damping ratio in the rectangular

cavity for all optimisations for 1, 5, 10, 20 and 100 TMDs, respectively. The case of a single PVAD shown in Figure 1.12 shows that the damping ratio is consistently about 20% for all the optimisations. The results for the other optimisations exhibit the trend that the damping ratio has an even distribution about the allowable range that was specified for the optimisations. However, the results for optimisation with 100 TMDs depart from this trend, where the damping ratios are in general below 10%.
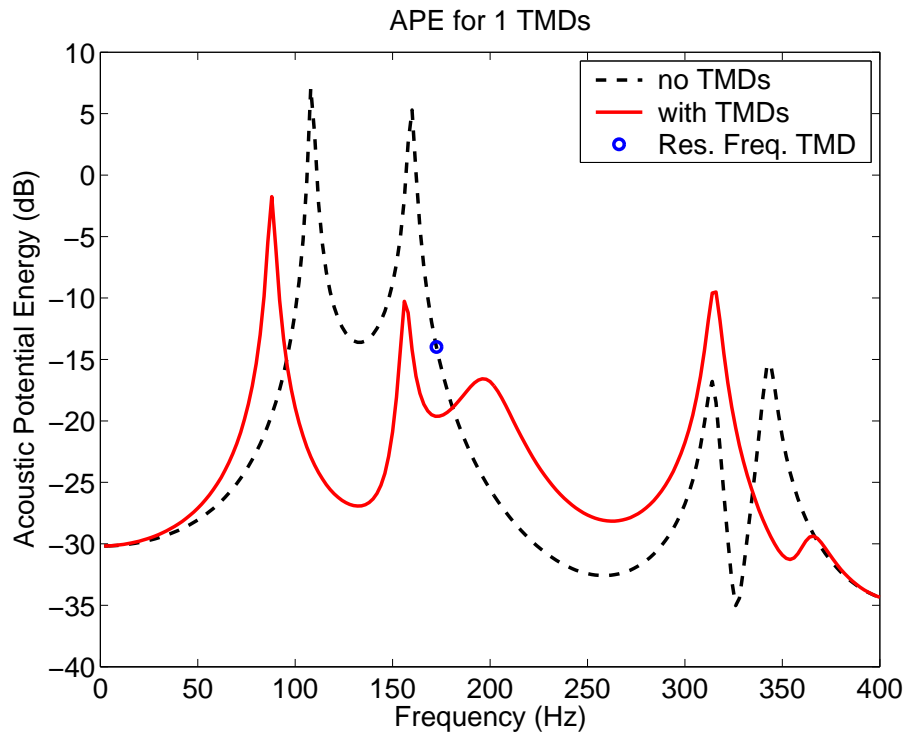
FIG. 1.7: Acoustic potential energy versus frequency for 1 TMD, for the best result.
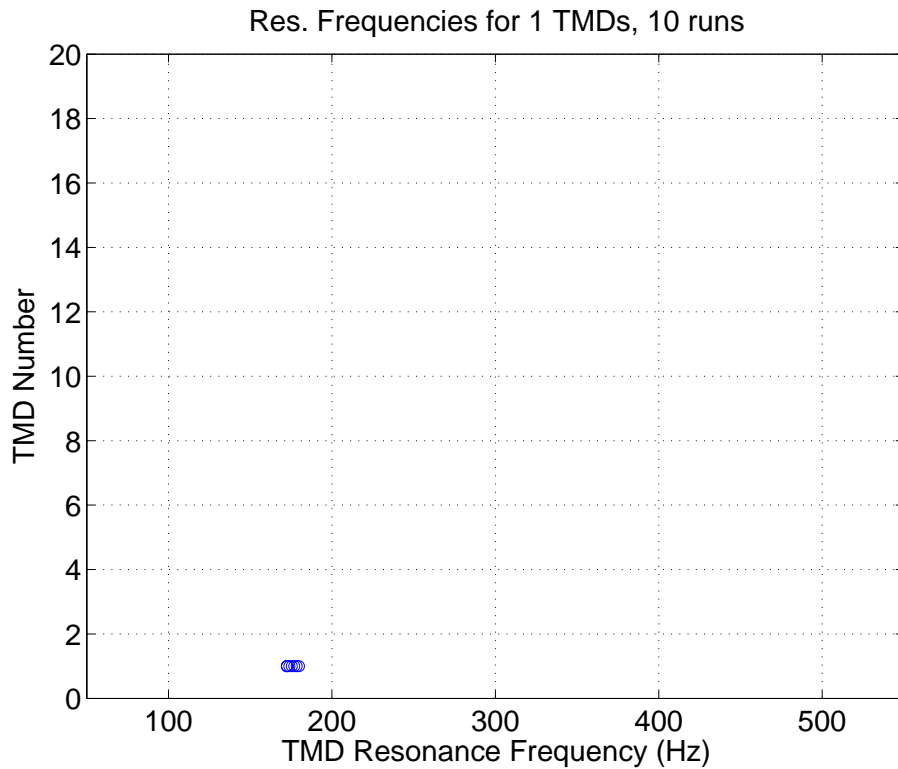
FIG. 1.8: Resonance frequencies for 1 TMD, for all 10 runs.

Node locations for 1 TMD
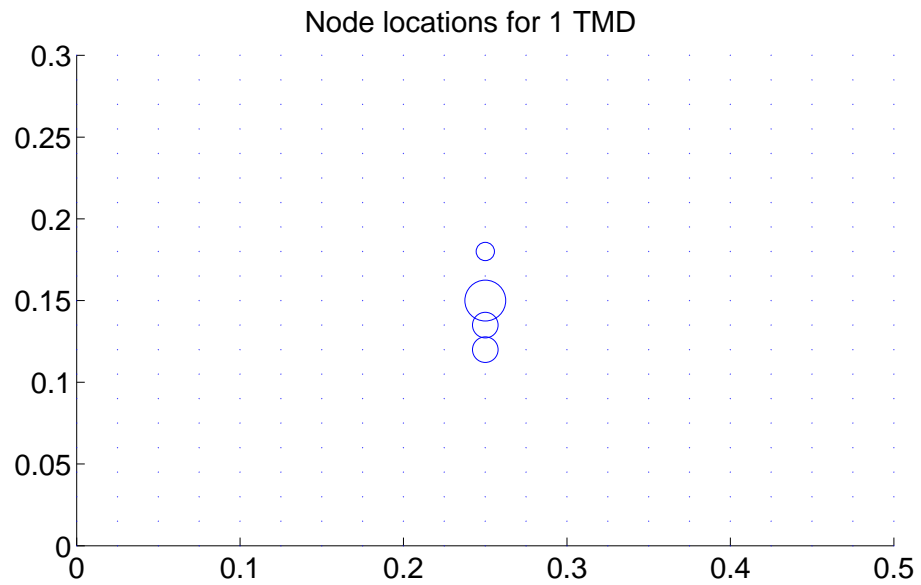
FIG. 1.9: Optimal location of 1 TMD on the plate, for all 10 runs.
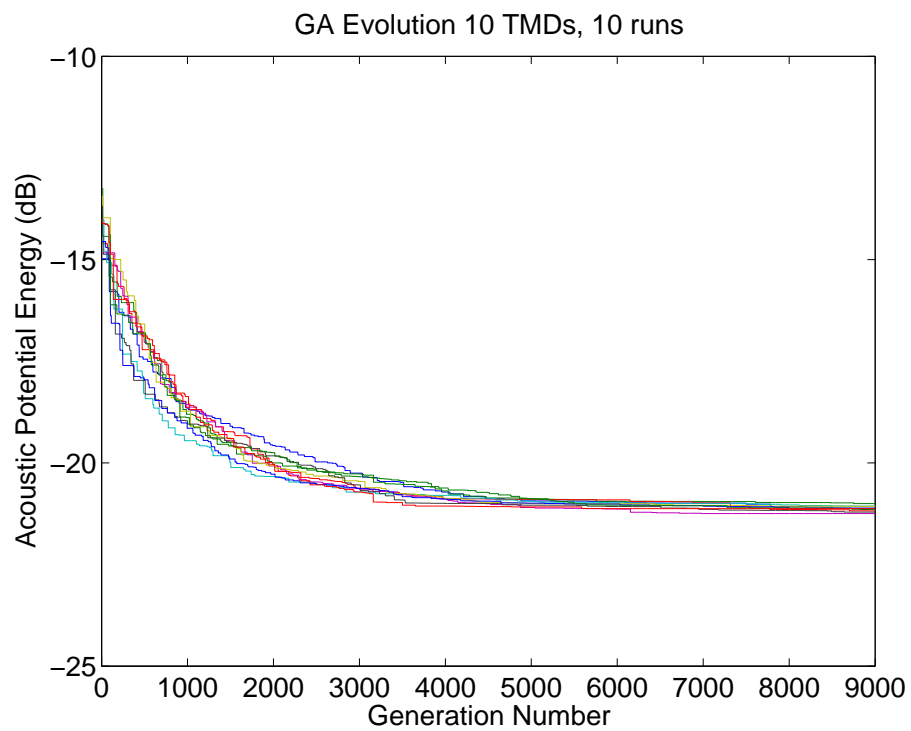
GA Evolution 1 TMDs, 10 runs
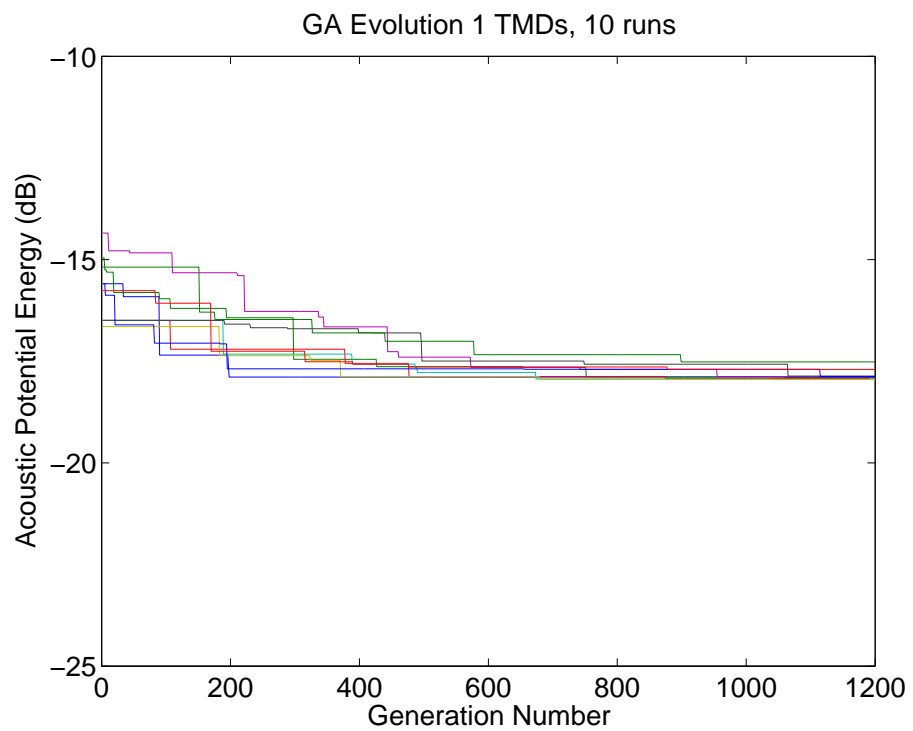
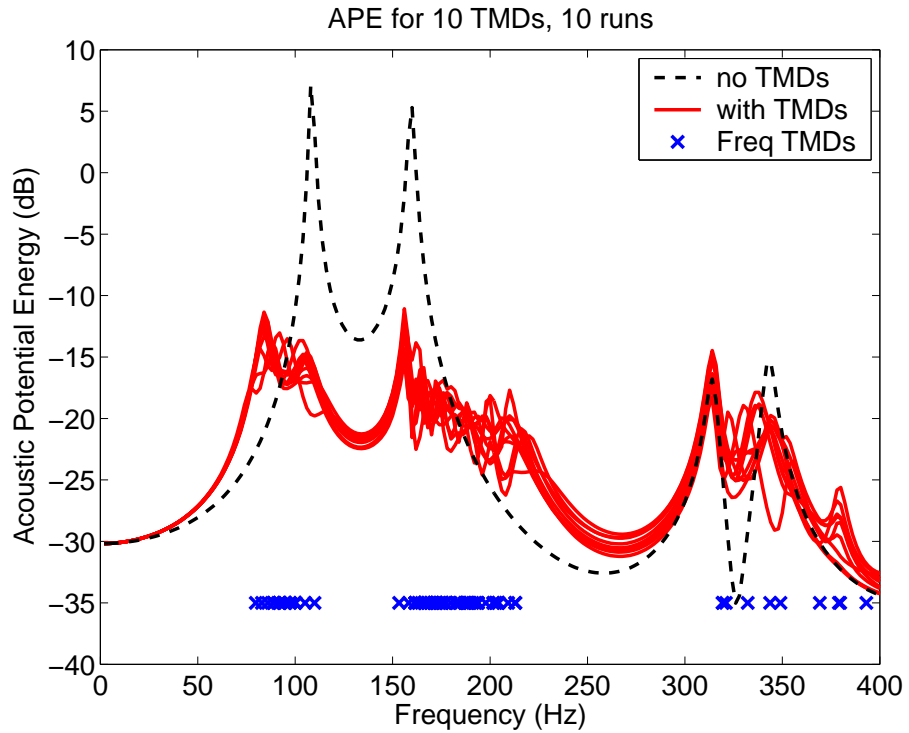FIG. 1.10: Genetic algorithm evolution of 1 TMD, for all 10 runs.
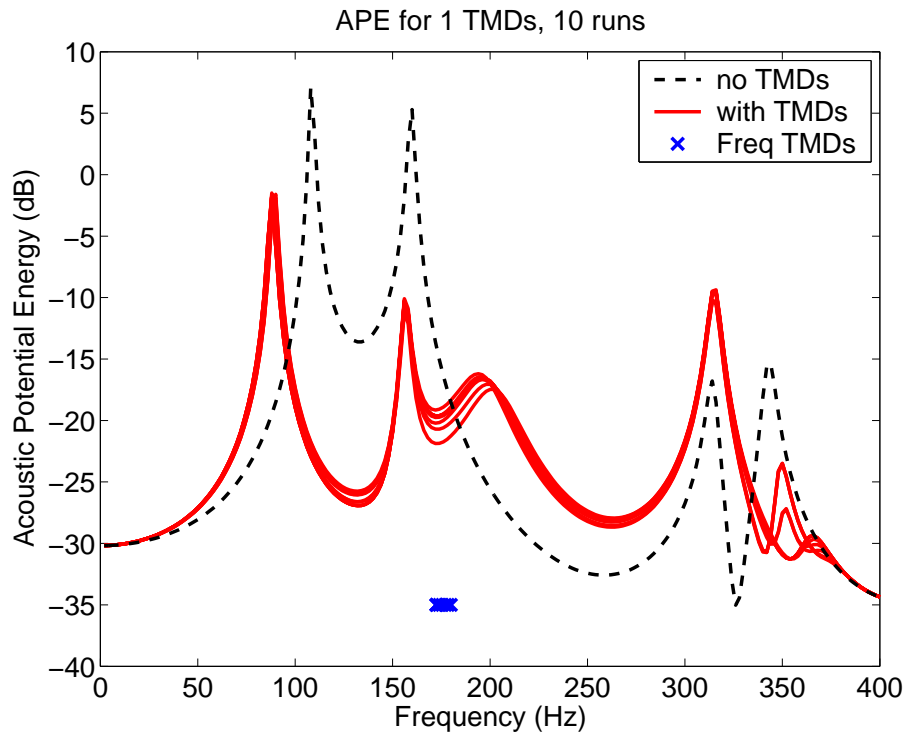
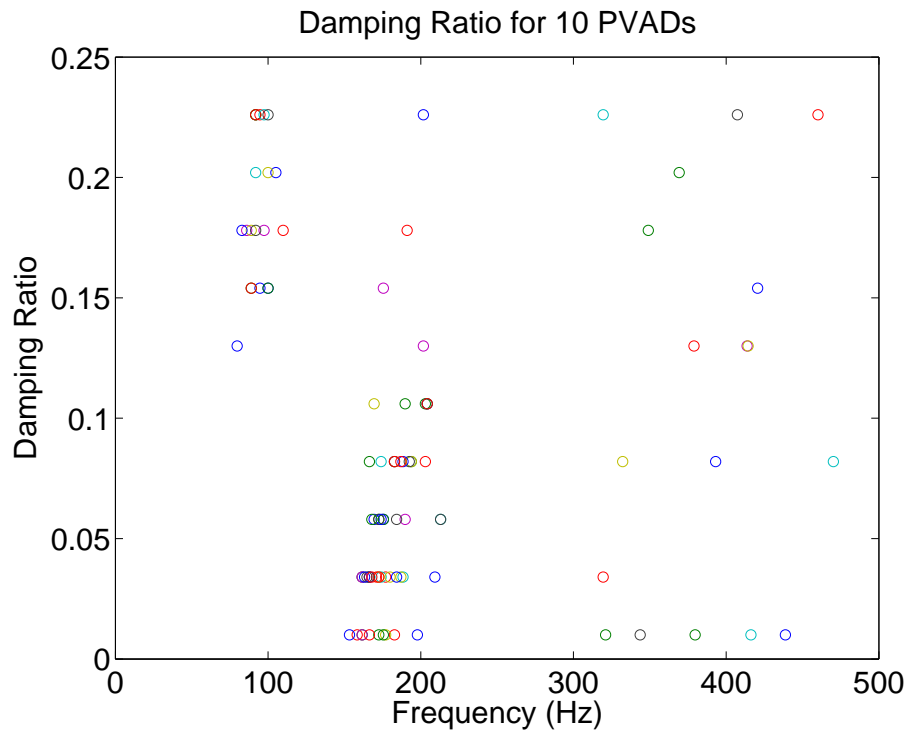FIG. 1.11: Acoustic potential energy versus frequency for 1 TMD, for all 10 runs.
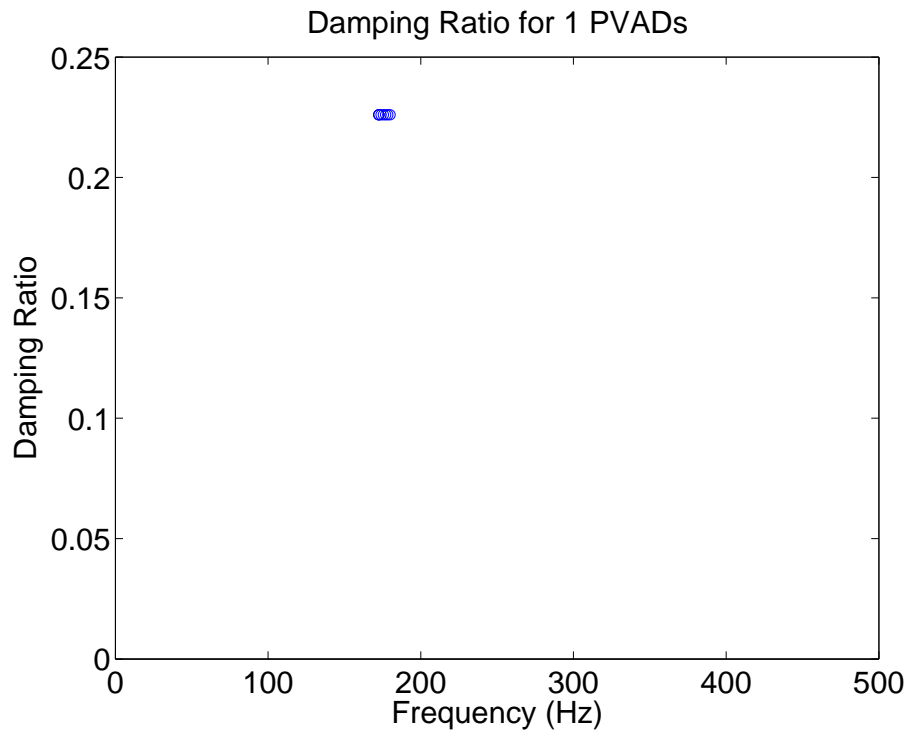
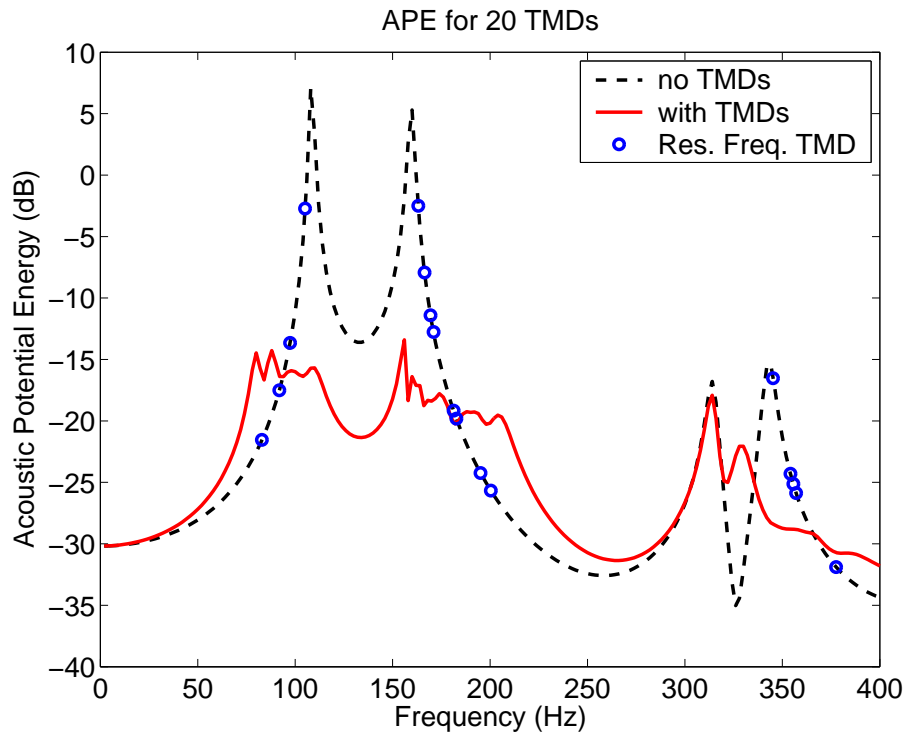FIG. 1.12: Damping ratios of PVADs versus frequency for 1 TMD, for all 10 runs.
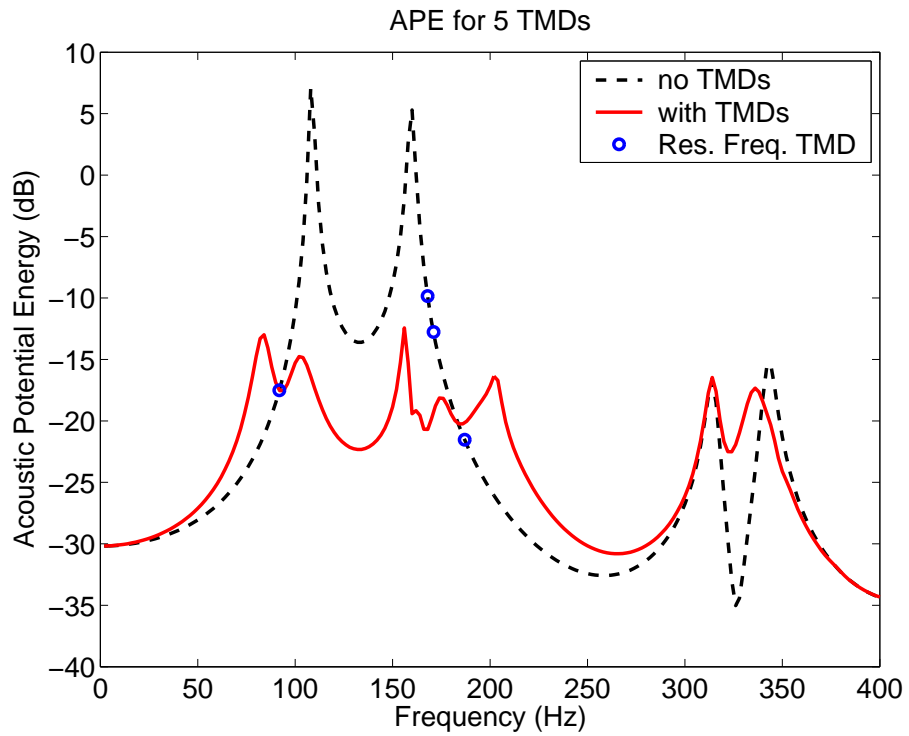
FIG. 1.13: Acoustic potential energy versus frequency for 5 TMDs, for the best result.
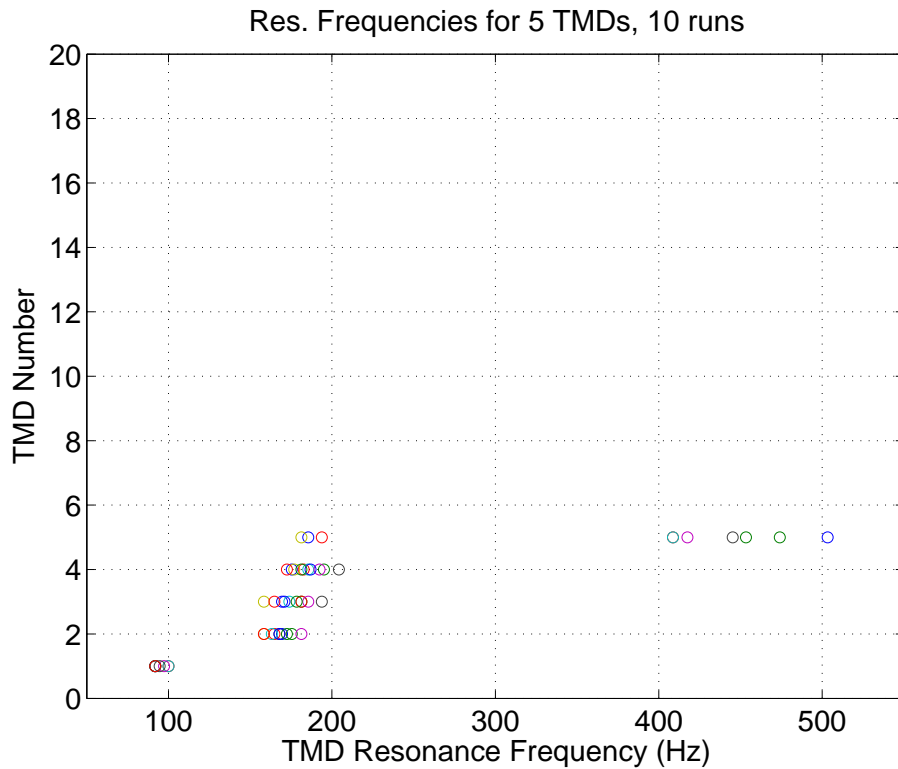
FIG. 1.14: Resonance frequencies for 5 TMDs, for all 10 runs.

Node locations for 5 PVADs
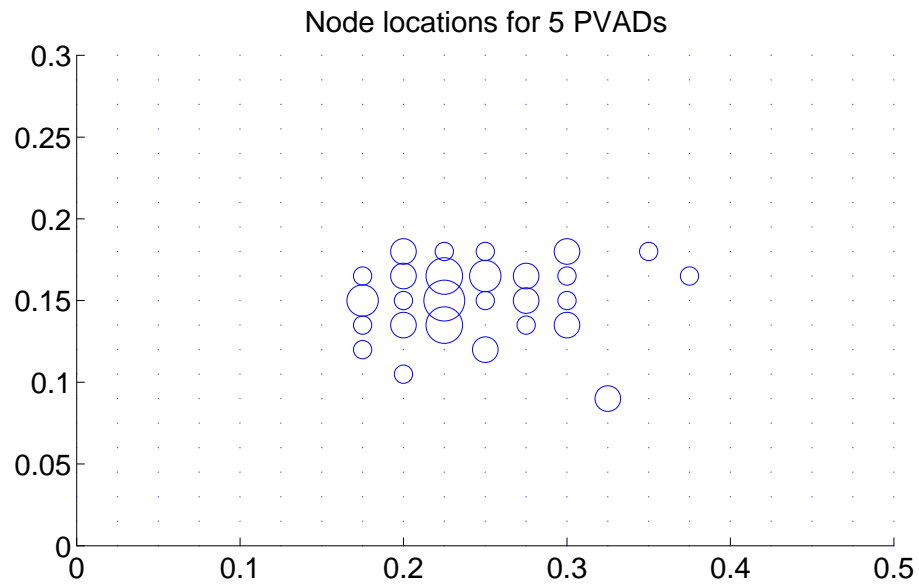
FIG. 1.15: Optimal locations of 5 TMDs on the plate, for all 10 runs.

GA Evolution 5 TMDs, 10 runs
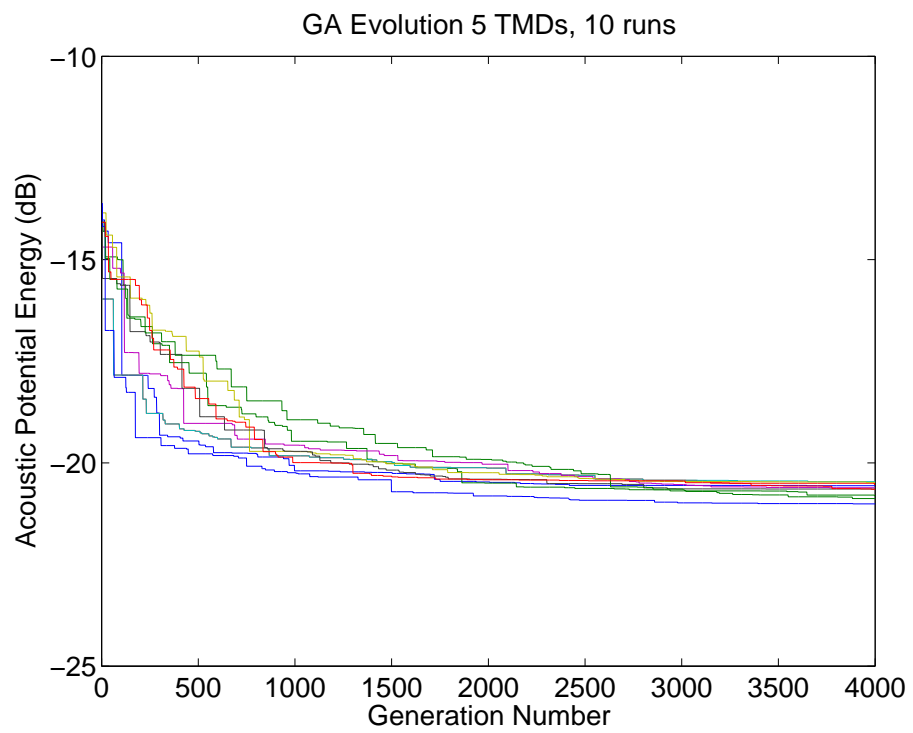
FIG. 1.16: Genetic algorithm evolution of 5 TMDs, for all 10 runs.
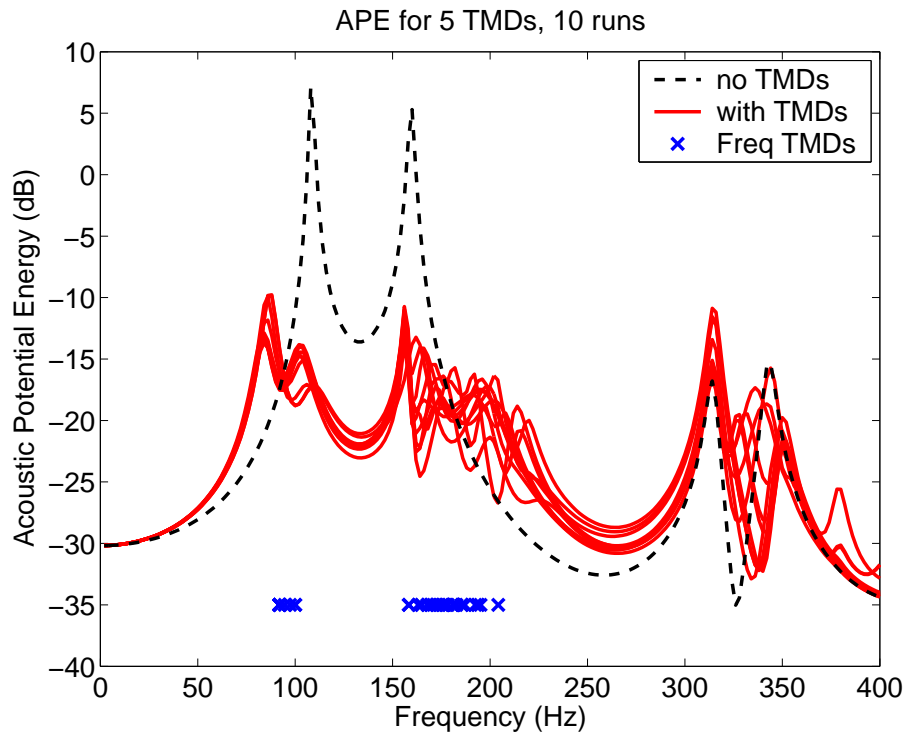
FIG. 1.17: Acoustic potential energy versus frequency for 5 TMDs, for all 10 runs.
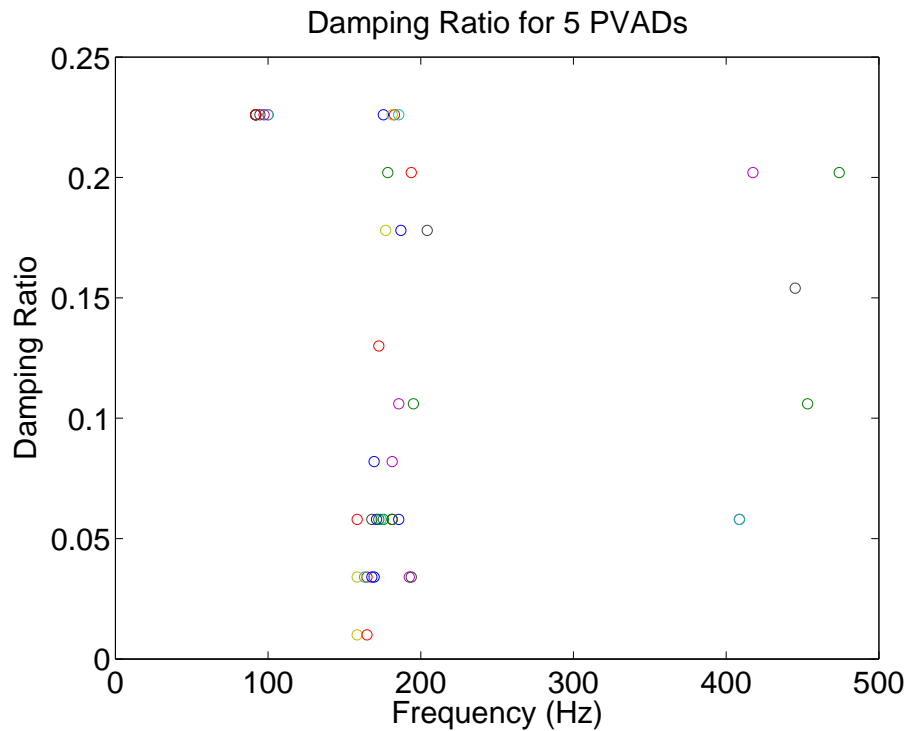
FIG. 1.18: Damping ratios of PVADs versus frequency for 5 TMDs, for all 10 runs.
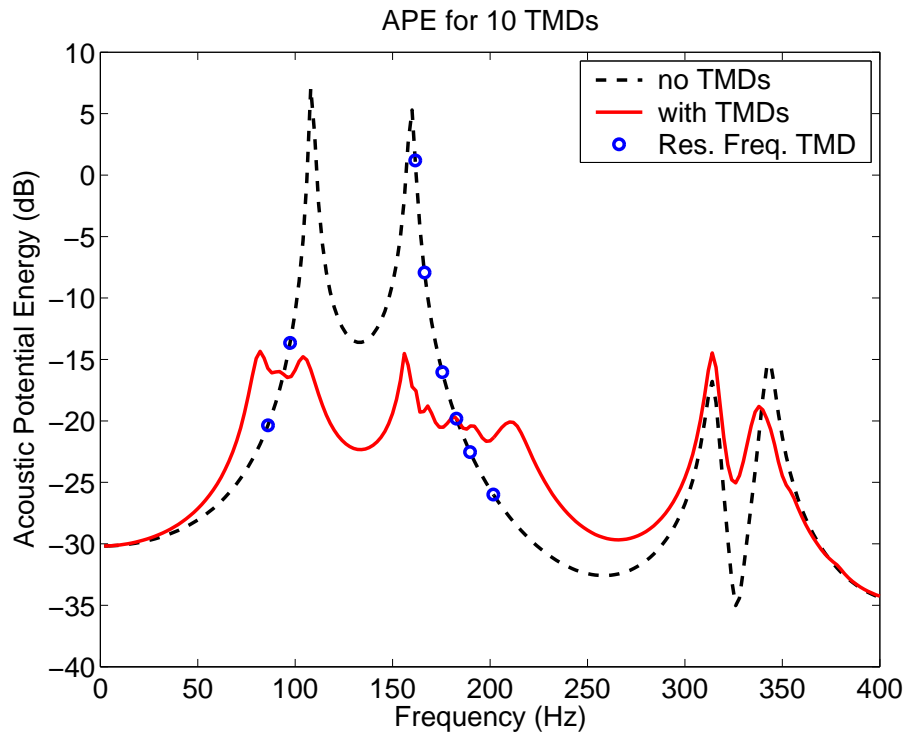
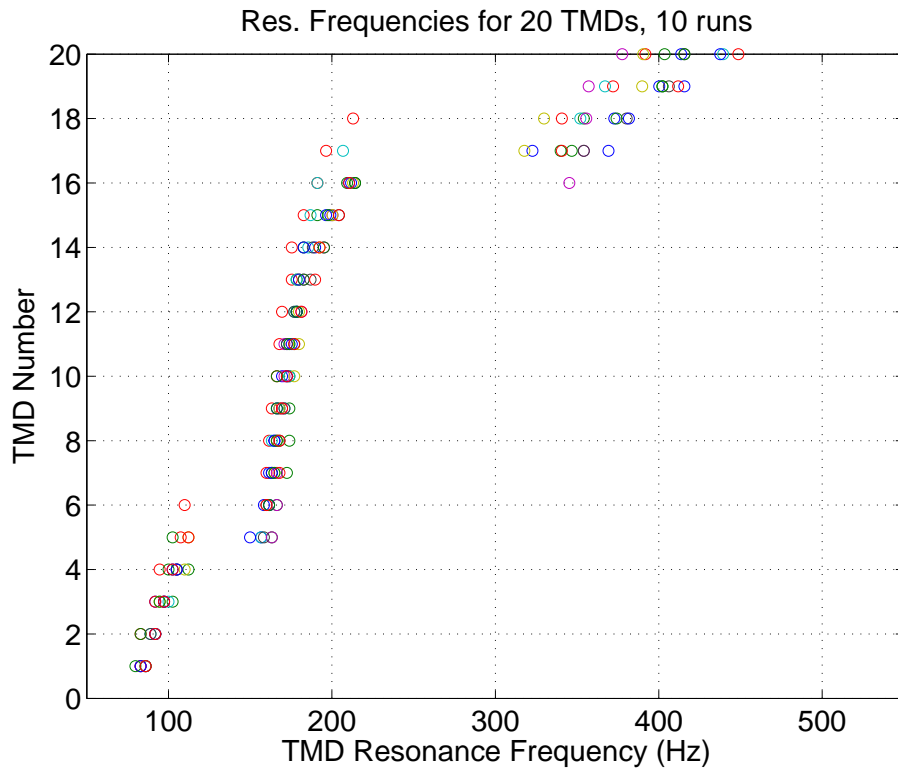FIG. 1.19: Acoustic potential energy versus frequency for 10 TMDs, for the best result.
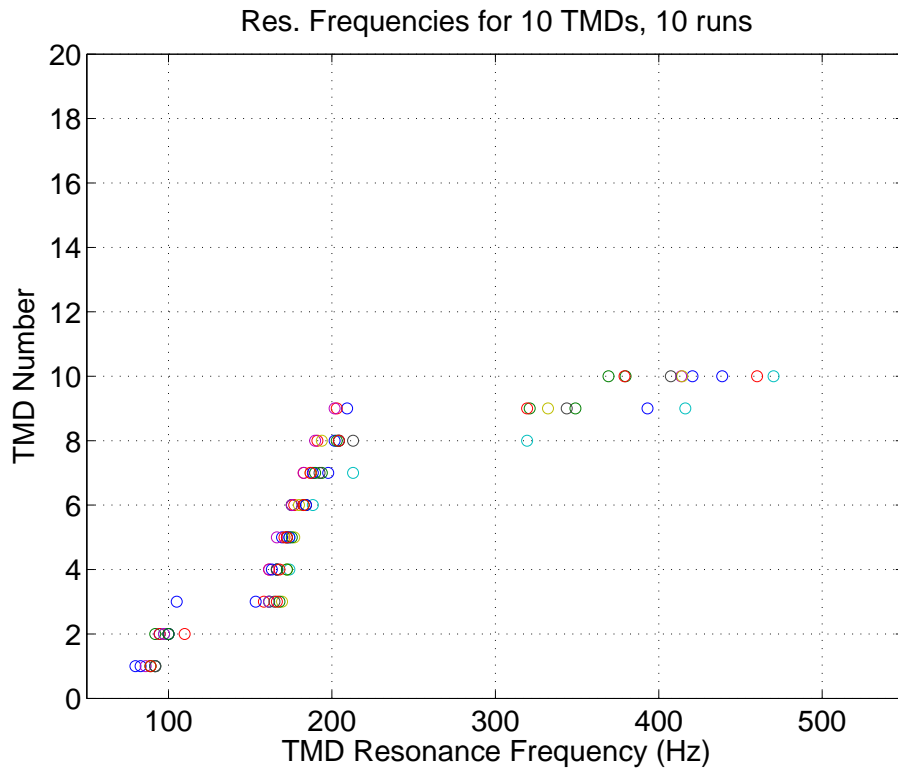
FIG. 1.20: Resonance frequencies for 10 TMDs, for all 10 runs.
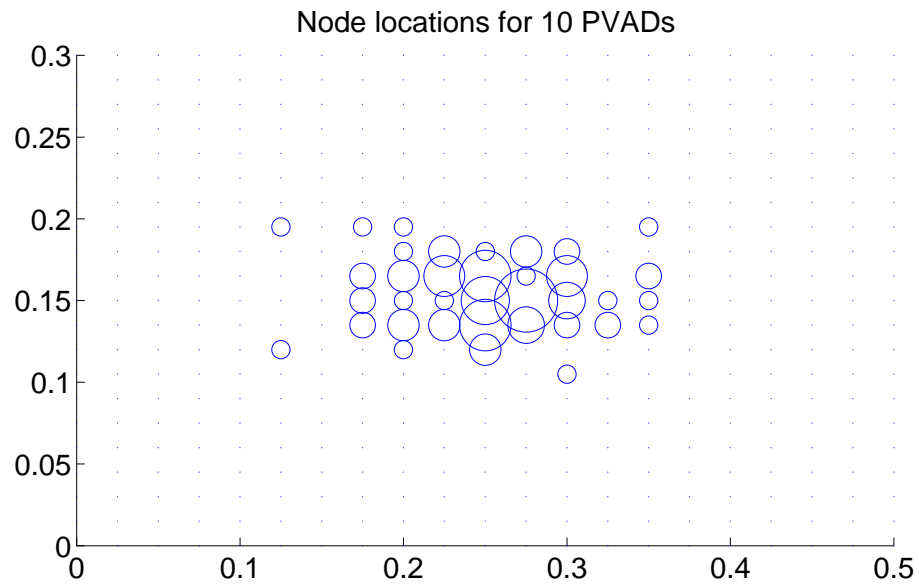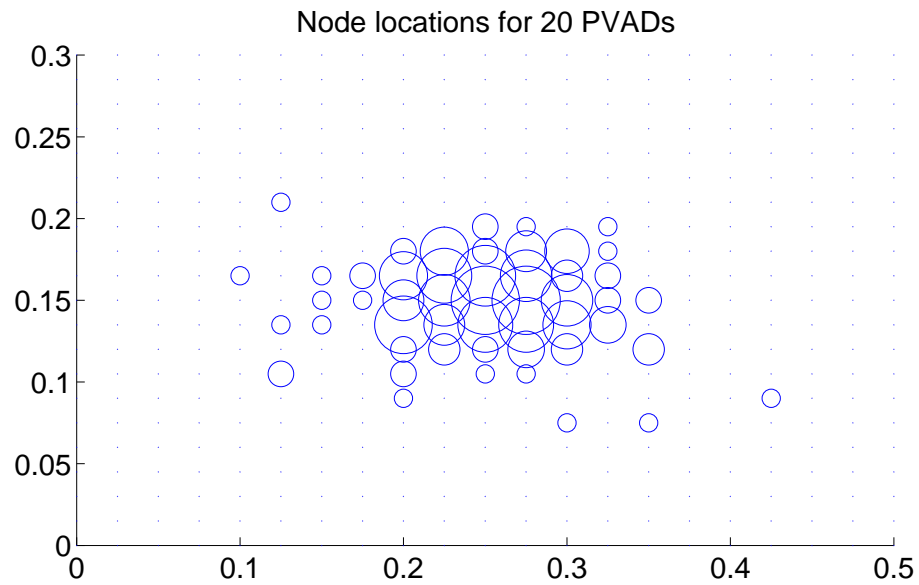
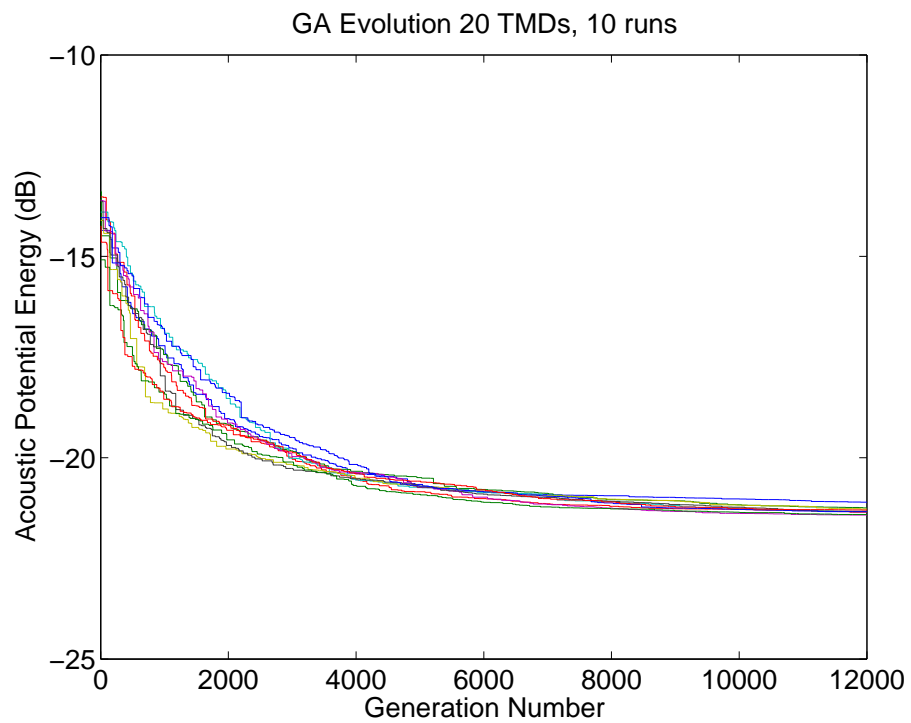FIG. 1.21: Optimal locations of 10 TMDs on the plate, for all 10 runs.

FIG. 1.22: Genetic algorithm evolution of 10 TMDs, for all 10 runs.

FIG. 1.23: Acoustic potential energy versus frequency for 10 TMDs, for all 10 runs.

FIG. 1.24: Damping ratios of PVADs versus frequency for 10 TMDs, for all 10 runs.

FIG. 1.25: Acoustic potential energy versus frequency for 20 TMDs, for the best result.

FIG. 1.26: Resonance frequencies for 20 TMDs, for all 10 runs.

FIG. 1.27: Optimal location of 20 TMDs on the plate, for all 10 runs.

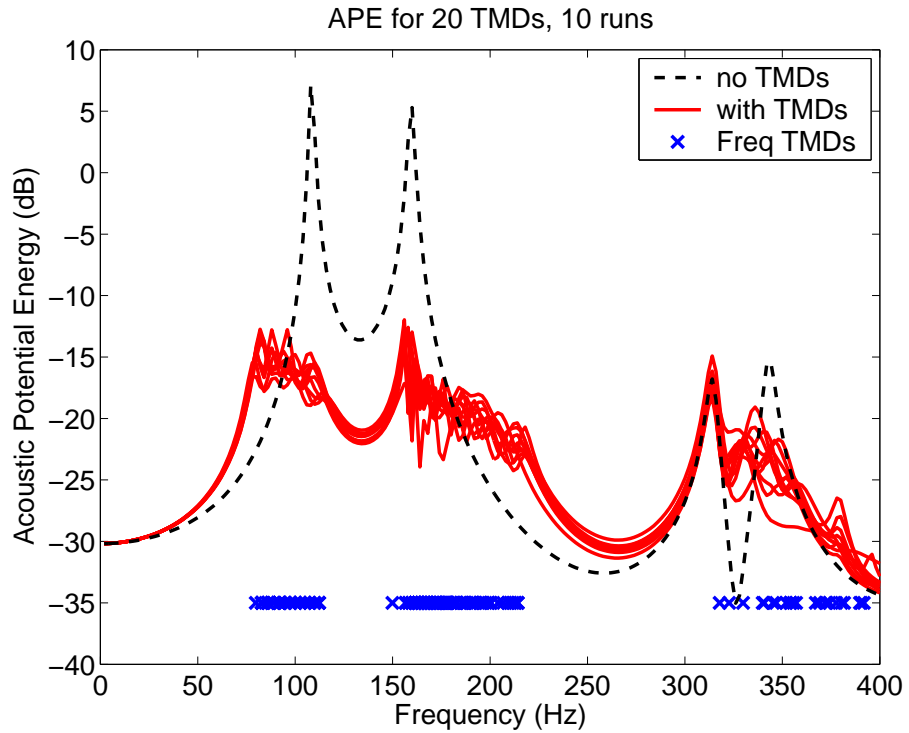FIG. 1.28: Genetic algorithm evolution of 20 TMDs, for all 10 runs.

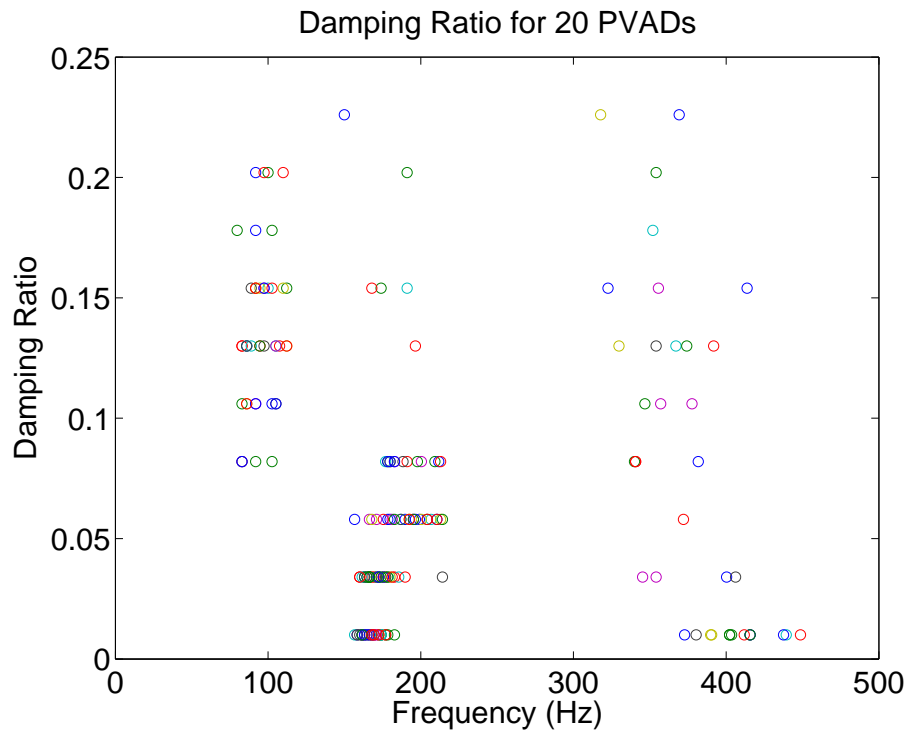FIG. 1.29: Acoustic potential energy versus frequency for 20 TMDs, for all 10 runs.

FIG. 1.30: Damping ratios of PVADs versus frequency for 20 TMDs, for all 10 runs.
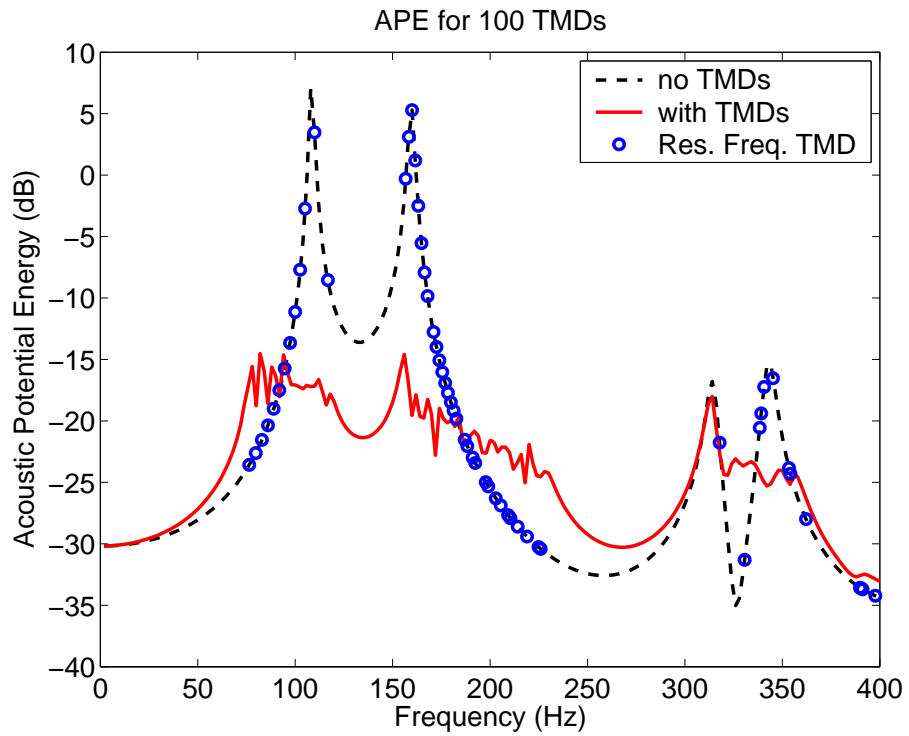
FIG. 1.31: Acoustic potential energy versus frequency for 100 TMDs, for the best result.
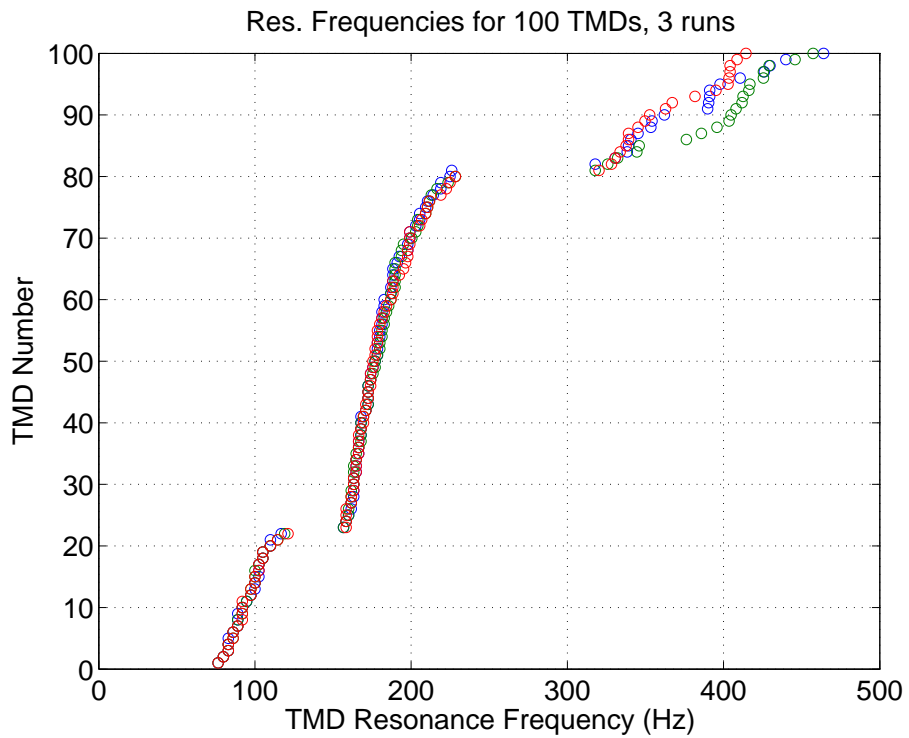

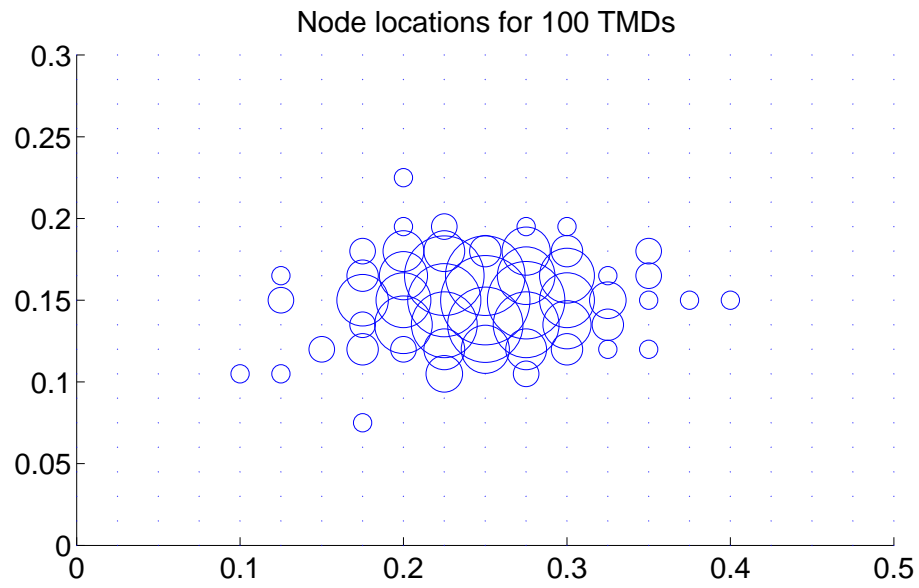FIG. 1.32: Resonance frequencies for 100 TMDs, for all 3 runs.

Node locations for 100 TMDs

FIG. 1.33: Optimal locations of 100 TMDs on the plate, for all 3 runs.
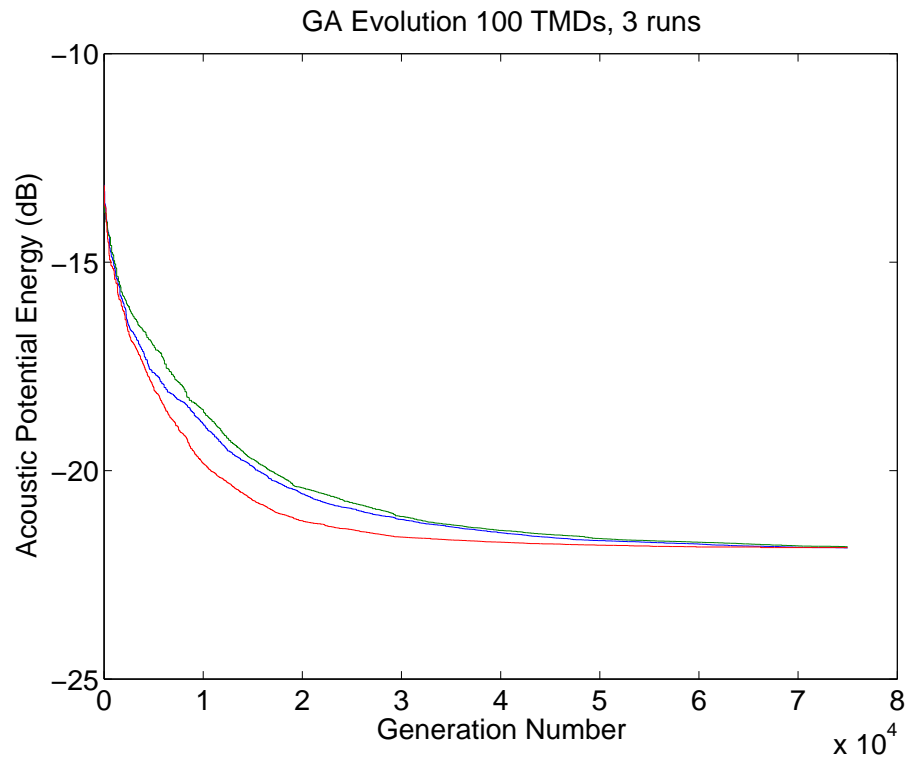
GA Evolution 100 TMDs, 3 runs

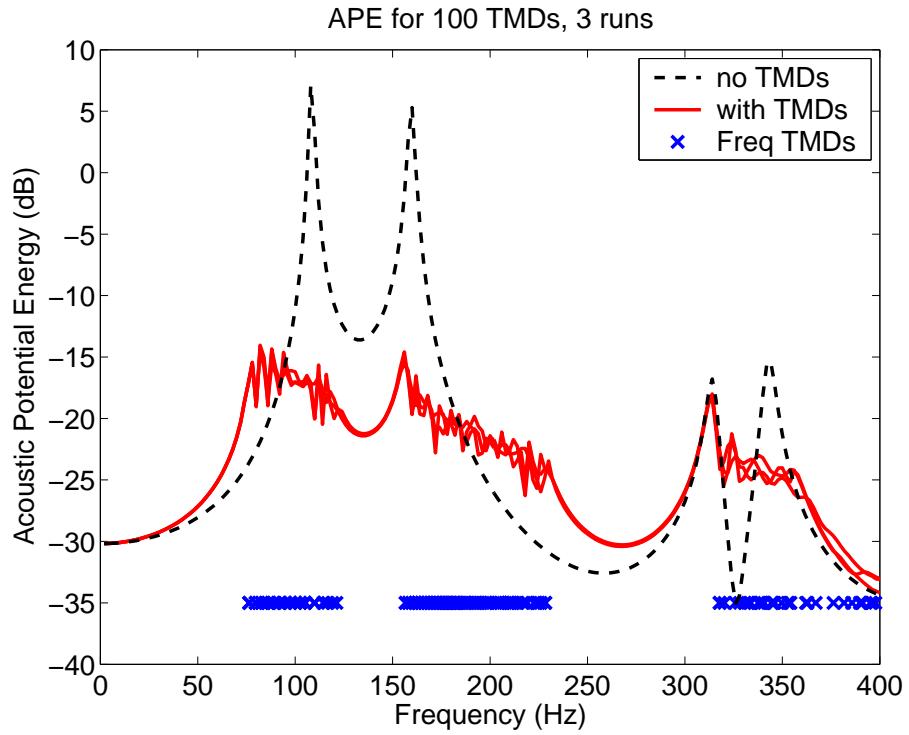FIG. 1.34: Genetic algorithm evolution of 100 TMDs, for all 3 runs.

FIG. 1.35: Acoustic potential energy versus frequency for 100 TMDs, for all 3 runs.
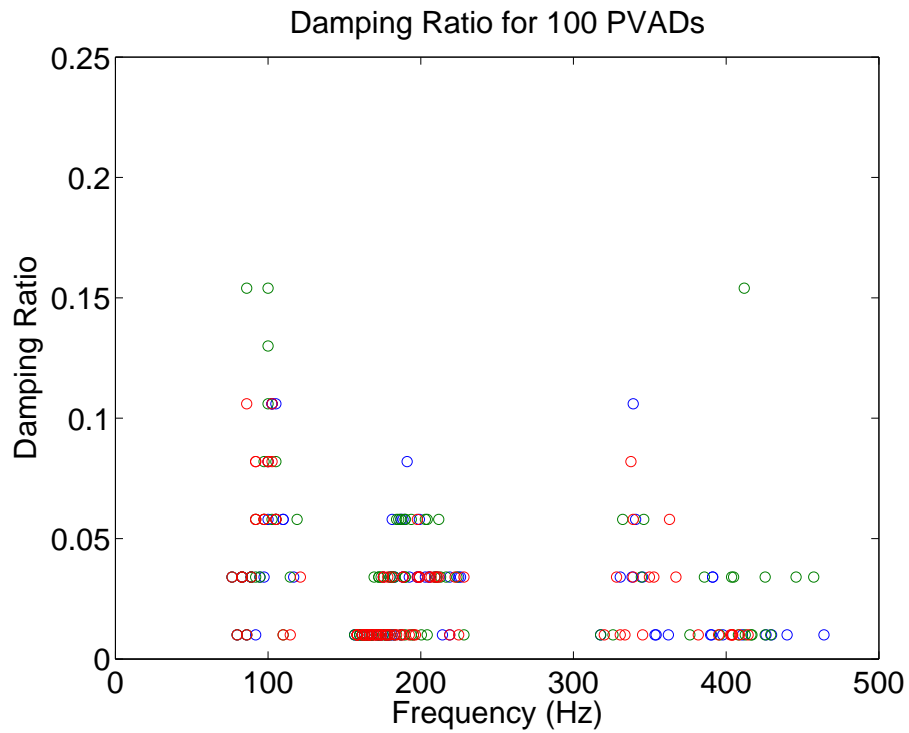

FIG. 1.36: Damping ratios of PVADs versus frequency for 100 TMDs, for all 10 runs.

Figure 1.38 shows the decrease in the total acoustic potential energy with the increasing number of TMDs, with a linear scale for the number of TMDs. Figure 1.39 shows the same results as shown in Figure 1.38, but plotted with a logarithmic scale for the number of TMDs. The results show there is an exponentially decreasing improvement in the noise reduction for increasing the number of TMDs, and plateaus around -22dB. Figure 1.38 also shows that when the thickness of the plate is increased such that it has a mass that is equivalent to the added mass of the TMDs, the total acoustic potential energy within the cavity is greater than when no TMDs are attached to the original plate.

The resonance frequency of a simply supported plate is calculated as [24]

$$ f = \frac{\pi}{2} \sqrt{\frac{Eh^2}{12\rho(1 - \nu^2)} \left[\frac{m^2}{a^2} + \frac{n^2}{b^2} \right]} \text{ (Hz)} \qquad (1.43) $$

where E is the Young's modulus of the plate, h is the thickness, ρ is the density of the plate, ν is the Poisson's ratio, m and n are the modal indices, and a and b are the length and width of the plate. Hence as the thickness of the plate increases, the resonance frequencies increase proportionally. Figure 1.37 shows the resonance frequencies for the normal thickness plate and when the plate thickness was increased to account for the added mass of the TMDs.

The optimum solutions for the 10 and 100 TMDs cases were further analysed by investigating whether changes in the location of the TMDs would cause significant changes in the APE. The locations of each of the TMDs was randomly altered to another nearby location in a circular selection zone. The radius of the selection zone was varied from 0.02m to 0.06m. Figures 1.40 and 1.41 show the variation in the acoustic potential energy with the change in the radius of the selection zone for the 10 and 100 TMDs cases, respectively. The optimal result obtained from the GA optimisations of 10 TMDs is shown in Figure 1.40 as the line at -21.07dB, and the optimum for the 100 TMDs case is shown in Figure 1.41 as the line at -21.85dB (for comparison with Figure 1.39).

The results for 10 TMDs show that changes to the locations of the TMDs cause large
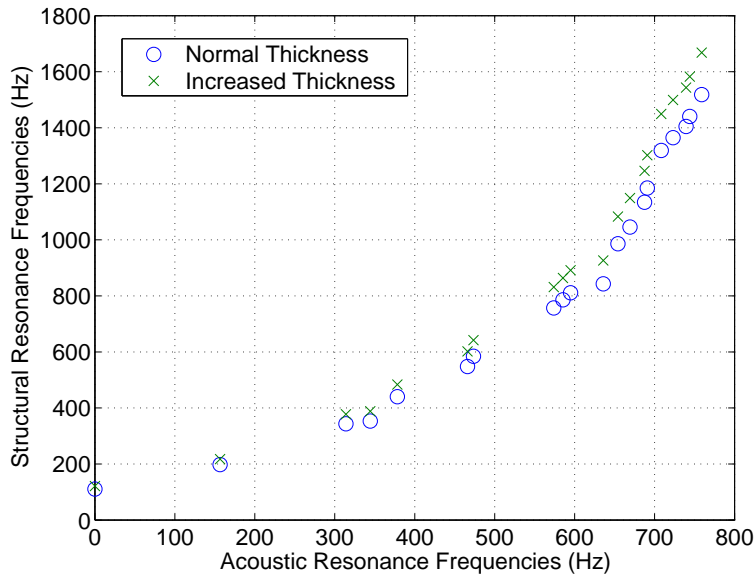
FIG. 1.37: Structural and acoustic resonance frequencies for the case of the standard plate thickness and the increased plate thickness.
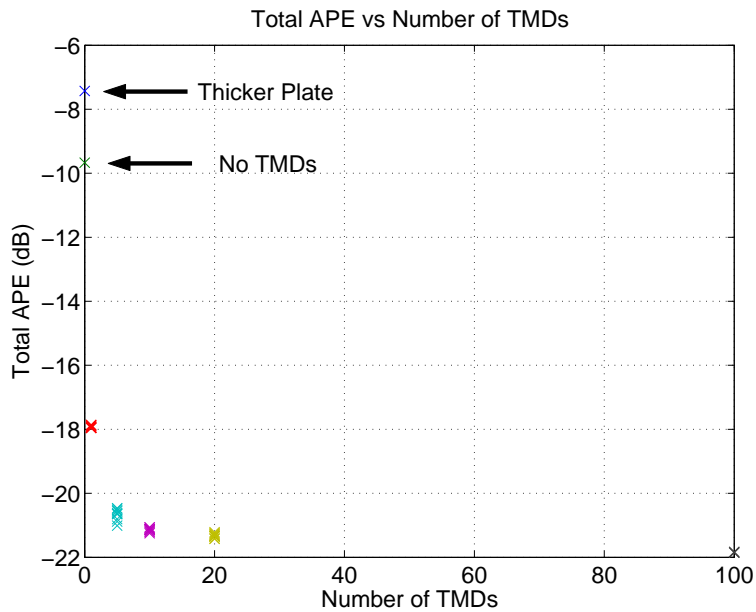

FIG. 1.38: Acoustic potential energy versus the number of TMDs for all runs.

changes to the acoustic potential energy, whereas the results for the 100 TMDs show that the acoustic potential energy is relatively insensitive to the locations of the TMDs.
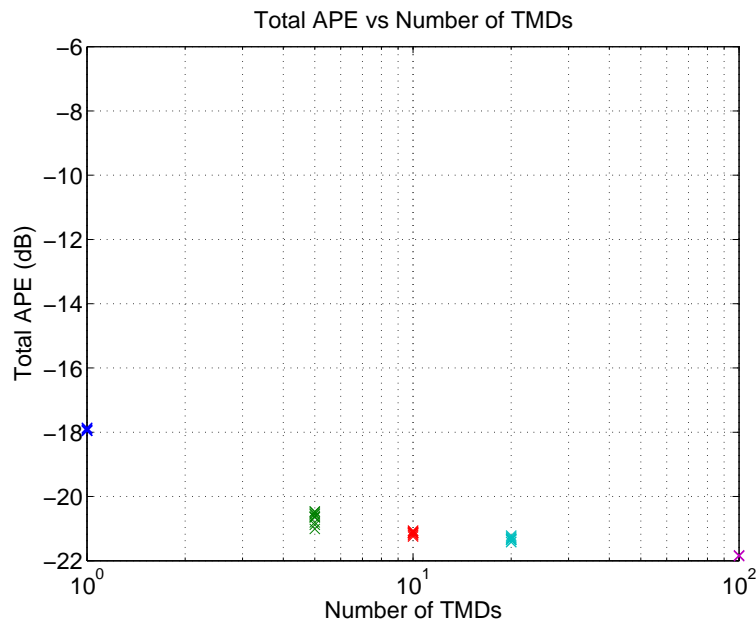
FIG. 1.39: Acoustic potential energy versus the number of TMDs for all runs.

1.8.3 Conclusions

The results show that in general, when there are large numbers of light-weight TMDs, the noise reduction is greater and relatively insensitive to the location of the TMDs, compared to using a few heavy weight TMDs. The optimum distribution of resonance frequencies is a linear distribution centred around the peak responses of the acoustic potential energy.

This design method is applied to the analysis of the Representative Scale Launch Vehicle Faring (RSLVF) in the following sections.

FIG. 1.40: Acoustic potential energy versus the radius for the selection zone, for 10 TMDs.

FIG. 1.41: Acoustic potential energy versus the radius for the selection zone, for 100 TMDs.

1.9   Representative Scale Launch Vehicle Fairing (RSLVF)
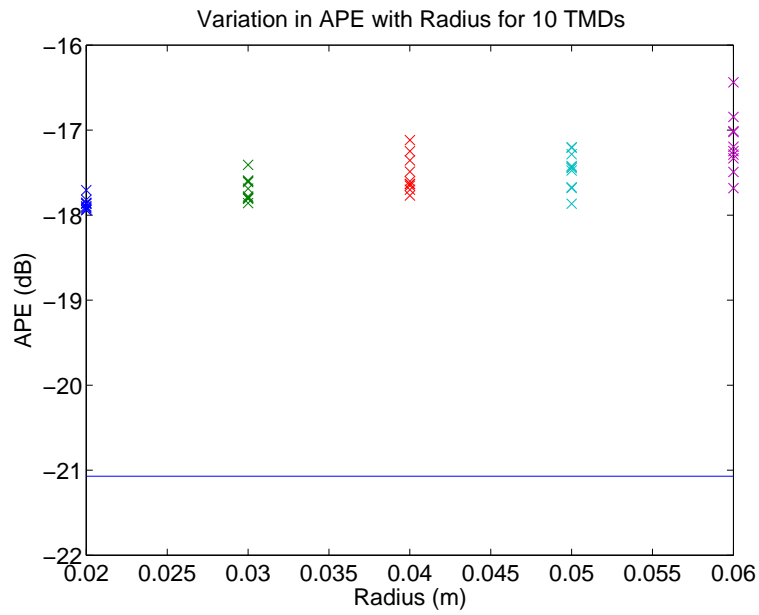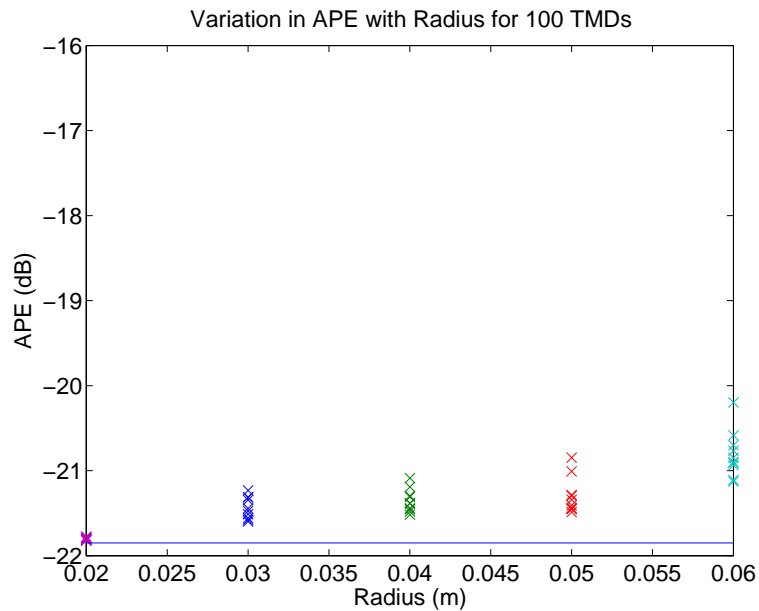
This section describes the optimisation of the design and location of the PVADs attached to the walls of the RSLVF. The optimisation methods employed here are similar to those used previously in Stage 3A, where the optimisation with the Boeing cylinder was investigated, and in Section 1.8 where the optimisation with a rectangular cavity was investigated.

The results from the previous section showed that the greatest noise reduction was achieved by attaching a large number of light weight absorbers to the walls of the fairing, which created a "fuzzy structure" response. It is expected that the same behaviour will occur for the optimisation of the RSLVF.

The following sub-sections describe the acoustic loading conditions that were assumed to act on the fairing, the optimisation method, the results for optimisation of 10, 100, and 500 PVADs attached to the fairing wall, and the effect of separating the HRs and TMDs.

1.9.1   Acoustic Loading on the Fairing

For the work presented here it is assumed that the acoustic loading is a harmonic plane wave that strikes the exterior of the fairing perpendicular to its axis. Future work will focus on more representative loading conditions, but this is not the focus of the work presented here.

In a finite element sense, the surface of the fairing can be discretised into small elements that have nodes at the corners of the area of each element. As the acoustic plane wave reaches the surface of the fairing, the pressure acts on an elemental area. This pressure can be converted into a nodal force, based on the area associated with each node, which can be applied to the modal model. The pressure that acts on the surface of the fairing is a function of the area that faces the incoming plane wave. Hence the nodes that have normals facing the impinging direction have the greatest pressure excitation amplitude, and the nodes that are at 90 degrees to the impinging direction have zero excitation pressure, as the plane wave is travelling tangentially to the surface of the fairing. It is

assumed that there is no diffraction around the fairing, and only half of the fairing is loaded. In reality, diffraction would be expected to occur around the fairing; however it may be assumed that this is of less importance than the waves that directly strike the fairing and thus diffraction will be ignored for the present purpose. Another effect that is ignored is the external re-radiation from the fairing, where the vibration of the structure generated by the incident sound field causes sound to radiate externally away from the structure (not into the cavity), hence removing vibrational energy from the structure and thereby providing a form of damping. This effect can be included at a later stage by adding radiation damping terms to the matrices [5, p466].

In Stage 3A, a cylindrical model was analysed and cosine functions were used to describe the variation of the nodal loads about the axis of the cylinder [2, Eq.(3.40)]. The fairing under investigation here is more complicated than the cylinder model, as the radius varies along the length of the fairing and hence the normal to surface of the fairing is not always perpendicular to the axis of the cylinder. Hence an alternative method, described here, is used to calculate the nodal forces to be applied to the fairing.

Figure 1.42 shows a diagram of the important features of the mathematical model for the pressure loading on the cylinder. The pressure is assumed to vary cosinusoidally around the circumference of the cylinder, due to the area that is normal to the impinging direction.
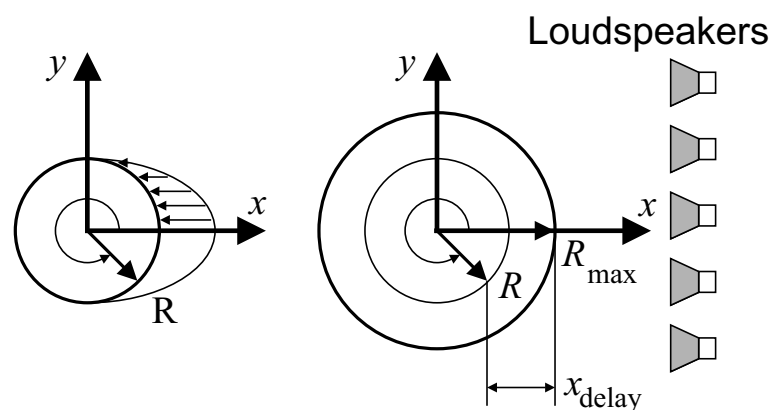

FIG. 1.42: Diagram of the plane wave striking the cylinder.

The results from the finite element analysis include a unit vector in the direction of the

normal to the fairing surface. The incident acoustic pressure wave is assumed to travel along the x-axis towards the origin. Hence one needs to calculate the component of this equivalent force that is projected onto the normal of the fairing surface.

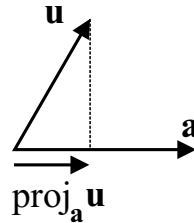Figure 1.43 shows a diagram of a vector $\mathbf{u}$ that is projected onto vector $\mathbf{a}$. The

FIG. 1.43: Diagram of a vector projection of $\mathbf{u}$ on $\mathbf{a}$.

projection of a vector is calculated as [25, p106]

$$\text{proj}_{\mathbf{a}}\mathbf{u} = \frac{\mathbf{u} \bullet \mathbf{a}}{\|\mathbf{a}\|^2} \, \mathbf{a} \tag{1.44}$$

which describes the vector component of $\mathbf{u}$ on $\mathbf{a}$.

We shall assume that a harmonic 200Pa (140dB re 20μPa) acoustic pressure wave strikes the surface of the fairing, and acts over a projected area A_{proj}. The phase of the acoustic pressure wave will differ across the surface of the fairing. We shall assume that at the point where the acoustic pressure wave first strikes the fairing, the pressure wave shall have zero phase. As the wave continues past this point, the phase shall change depending on the distance travelled and the frequency of the harmonic pressure wave. Hence the nodal force that acts on the fairing is a function of:

- The magnitude of the incident pressure (P_0)

- The projected nodal area (A_{proj})

- The phase shift due to the acoustic path length

The projected area is calculated by scaling the nodal area using Eq.(1.44), where $\mathbf{u}$ is a vector in the direction of the incident pressure wave ($\mathbf{u} = [1, 0, 0]$), and $\mathbf{a}$ is the unit vector normal to the fairing surface obtained from the finite element analysis.

The distance travelled by a plane wave between the surface closest to the noise source and a point on the circumference on the fairing is

$$x_{\text{delay}} = R_{\text{max}} - R \cos \theta \tag{1.45}$$

where R_{max} is the radius where the incident pressure wave first strikes the fairing and θ is the angle from the x-axis to the node at radius R and has the range $-\pi/2 < \theta < +\pi/2$. The phase delay is calculated as

$$\text{phase delay} = \frac{2\pi}{\lambda} x_{\text{delay}} \tag{1.46}$$

where $\lambda = c/f$ is the wavelength of sound, c is the speed of sound, and f is the frequency in Hertz.

Hence the nodal force is calculated as

$$F_{\text{node}} = P_0 A_{\text{node}} \left\| \frac{\mathbf{u} \bullet \mathbf{a}}{\|\mathbf{a}\|^2} \mathbf{a} \right\| \left[\cos\left(\frac{2\pi x_{\text{delay}}}{\lambda} \right) + j \sin\left(\frac{2\pi x_{\text{delay}}}{\lambda} \right) \right] \tag{1.47}$$

Figure 1.44 shows a slice through the fairing at $z = 2$m of the magnitude of the nodal forces calculated using Eq. (1.47). Note that this figure does not show the effect of the phase delay.

Figure 1.45 shows all the nodal forces that are applied to the fairing, once again omitting the effect of the phase delay.

Figure 1.46 shows the real and imaginary parts of all the nodal forces that are applied to the fairing for the analysis frequency range. Each curve shows the nodal force for all frequencies. The curves are circular about the origin with a constant radius, indicating that the magnitude of the force is constant and the phase changes with frequency.
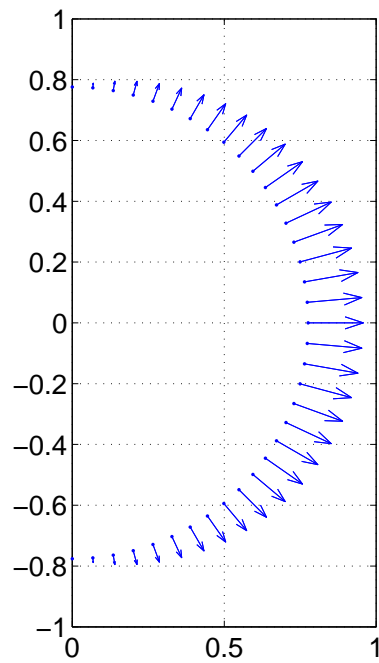
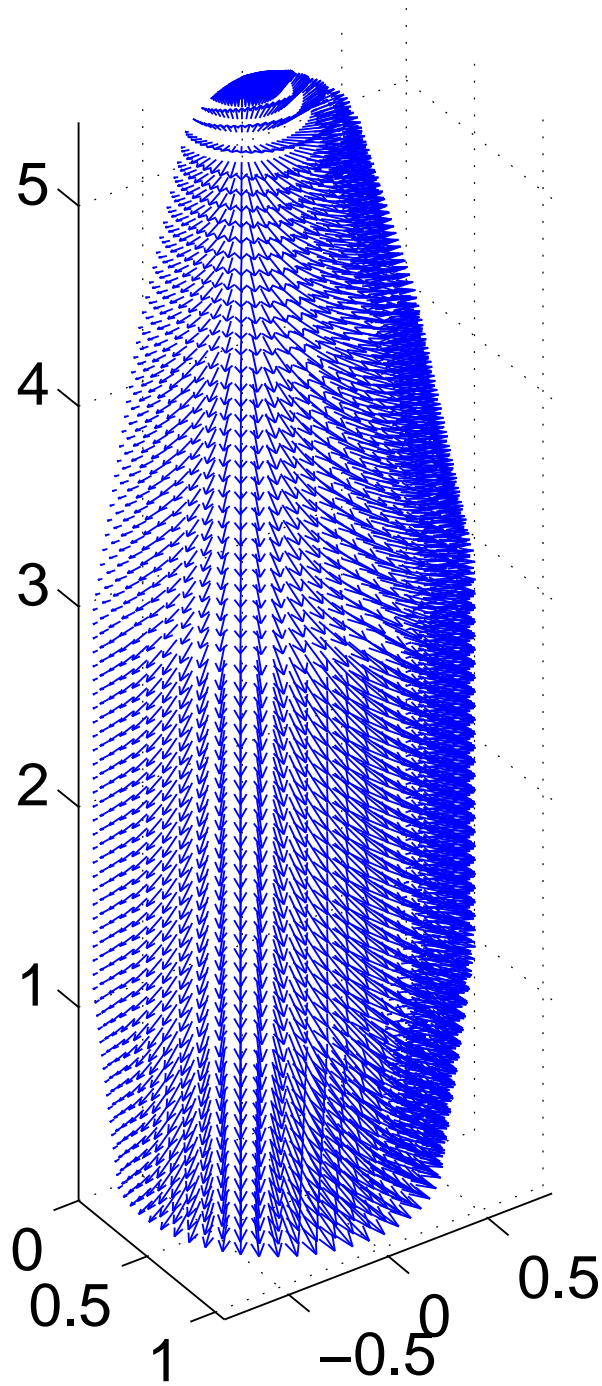FIG. 1.44: Loading on the fairing at z=2m.
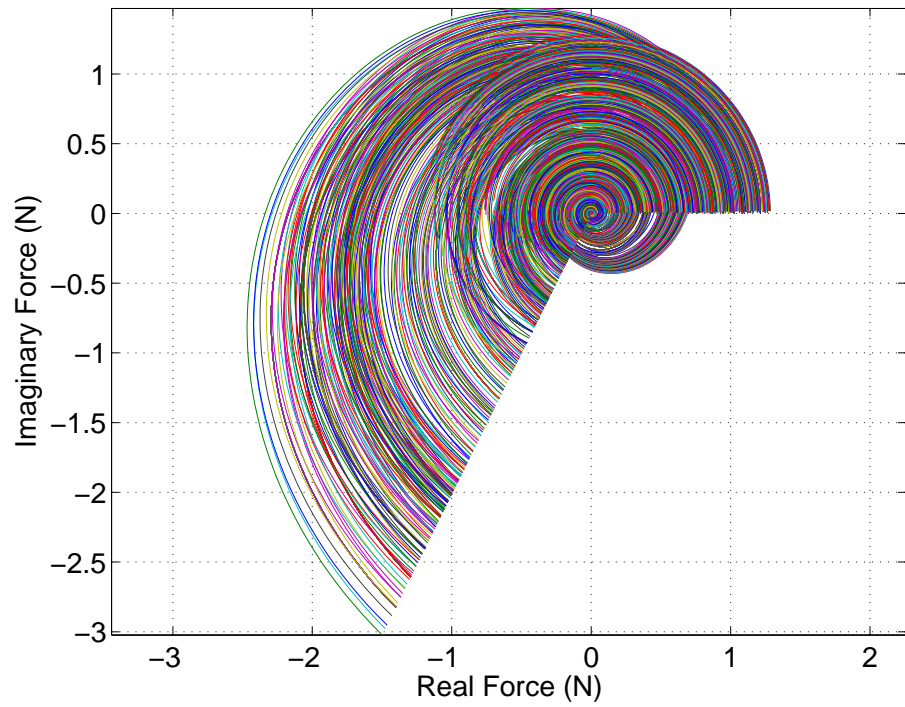
FIG. 1.45: Loads on the fairing.

FIG. 1.46: Real and imaginary parts of all nodal forces applied to the fairing.

1.9.2   Modal Analysis

A modal analysis was conducted on the finite element model of the RSLVF to calculate the in-vacuo structural and acoustic resonance frequencies. The frequency range of interest is from 0Hz to 300Hz and the modal analysis was conducted to include resonance frequencies at least one octave (doubling of frequency) greater than the frequency range of interest; hence resonance frequencies from 0Hz to over 600Hz were calculated. Table 1.5 lists the first ten structural and acoustic resonance frequencies, and Figure 1.47 shows all the structural and acoustic resonance frequencies that were included in the analyses described in this report. Some of the structural resonance frequencies are repeated as they are associated with the circumferential mode shapes of the fairing that have "odd" and "even" mode shapes, which is typical for cylindrical structures [6]. Figure 1.48 shows the distribution of the structural and acoustic resonance frequencies grouped into 10Hz bins.

Table 1.5: Structural and acoustic resonance frequencies of the RSLVF.

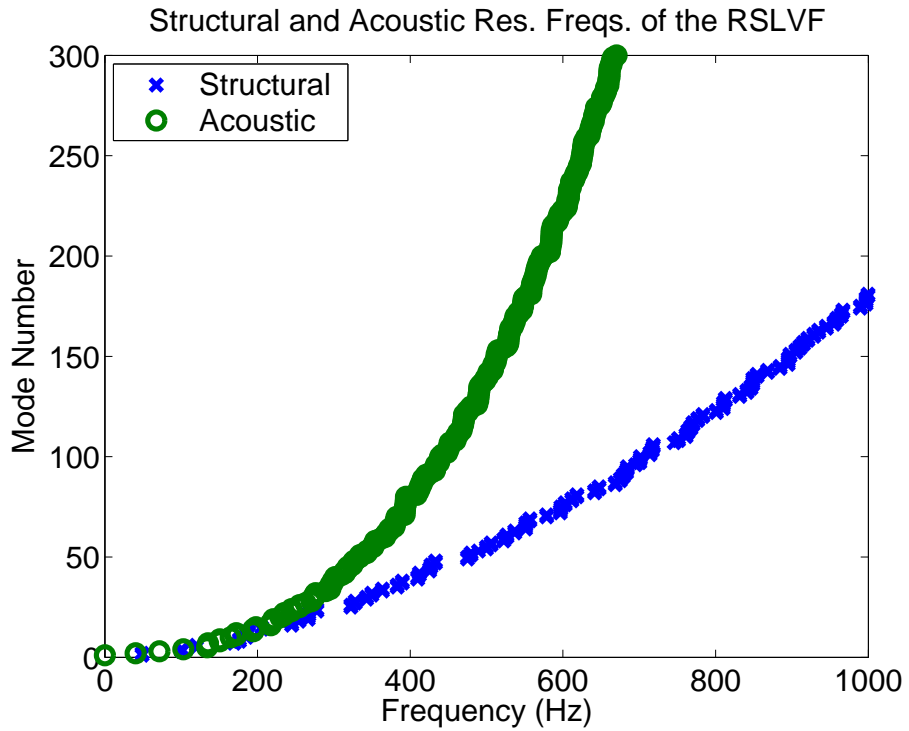| Mode No.	Structural (Hz)	Acoustic (Hz)
1	49	0
2	49	40
3	101	71
4	101	103
5	120	134
6	120	135
7	170	135
8	176	151
9	176	151
10	185	165

FIG. 1.47: Structural and acoustic resonance frequenices of the RSLVF.
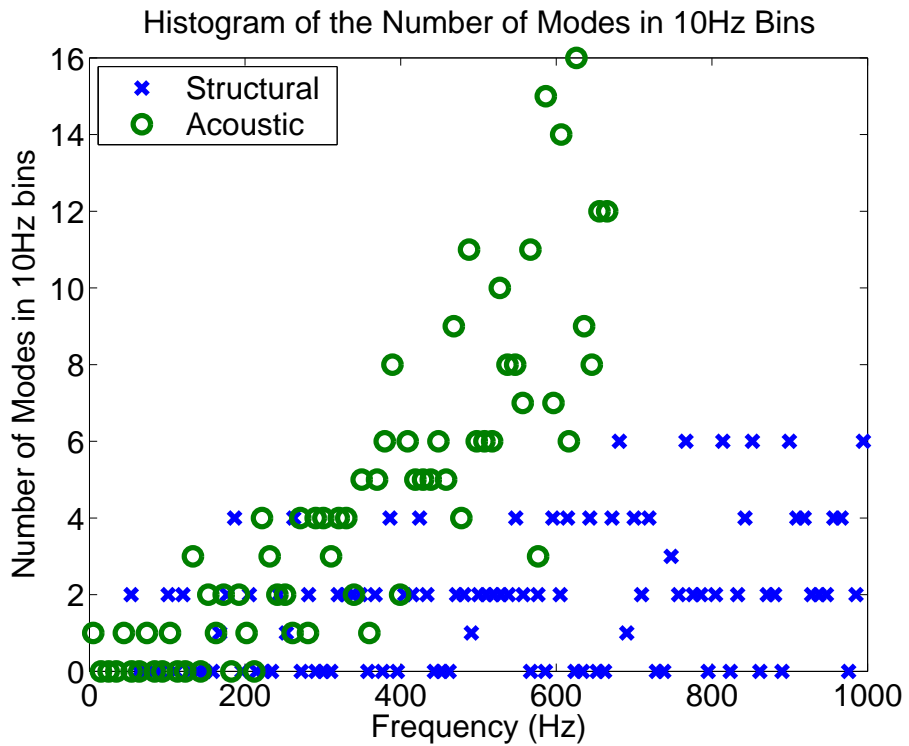
FIG. 1.48: Distribution of structural and acoustic resonance frequenices of the RSLVF grouped into 10Hz bins.

1.9.3 Optimisation Method

Optimisations were conducted on the RSLVF for the location and parameters of the tuned mass dampers and Helmholtz resonators. The optimisations were conducted for 10, 100, and 500 PVADs. The parameters were allowed to vary as listed in Table 1.6.

Table 1.6: PVAD parameter range for the optimisation of the RSLVF.

PVAD parameter	Min	Max	No. Values	Comment
PVAD position	1	5184	5184	Circumferential nodes
Mass-spring frequency	11	510	500	[Hz]
Mass-spring damping (η)	0.01	0.25	10	
Acoustic resonator frequency	11	510	500	[Hz]
Acoustic resonator damping (η)	0.01	0.25	10	

It was assumed that the PVADs could be placed on the perimeter of the fairing, except at the top of the nose cone, and on the base of the fairing. Figure 1.49 shows the 5184 possible locations where the PVADs can be placed.

The following sections show the results of the optimisations for 10, 100, and 500 PVADs.
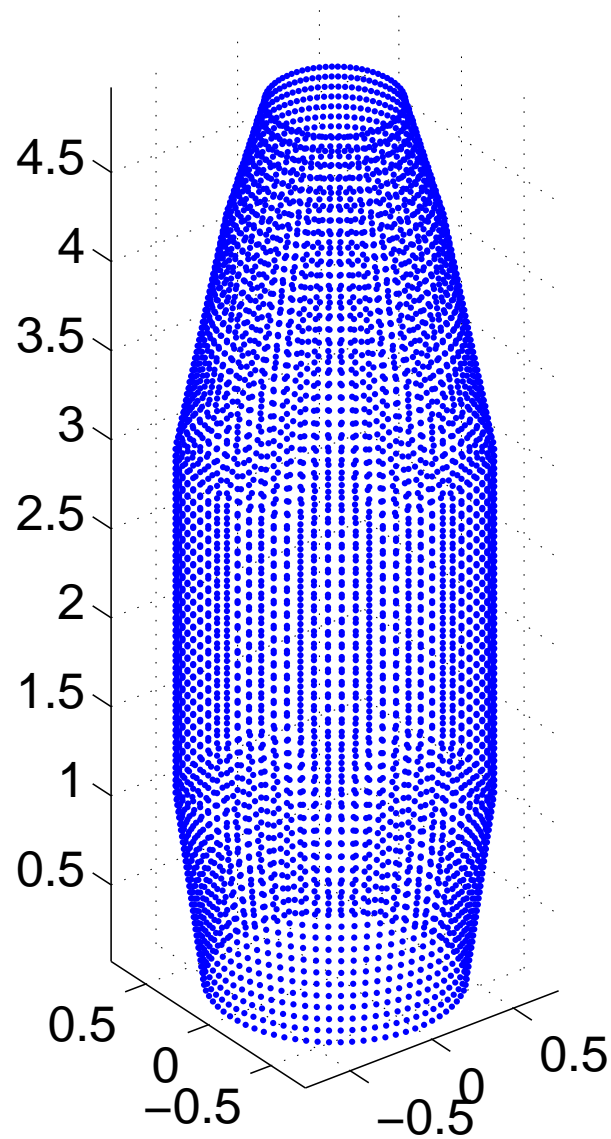
FIG. 1.49: The 5184 possible node locations for the PVADs on the circumference of the fairing.

1.9.4   10 PVADs

FIG. 1.50: Acoustic potential energy versus frequency for 10 PVADs.

FIG. 1.51: Resonance frequencies for 10 PVADs.

FIG. 1.52: Location of 10 PVADs on the fairing.

FIG. 1.53: Genetic algorithm evolution of 10 PVADs.
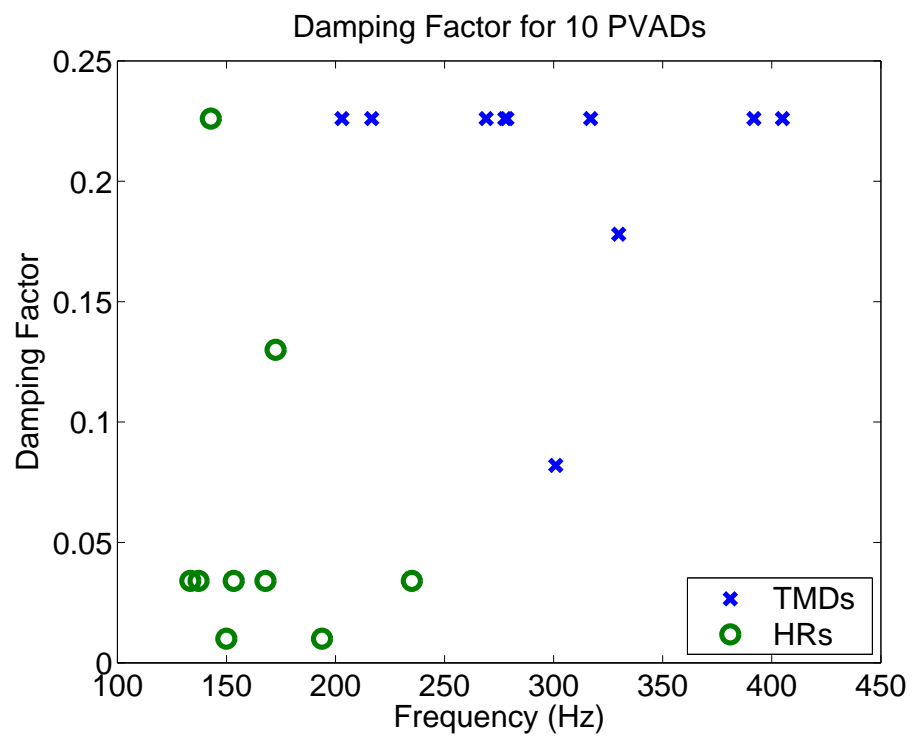
FIG. 1.54: Damping factor versus frequency for 10 PVADs.

1.9.5   100 PVADs

FIG. 1.55: Acoustic potential energy versus frequency for 100 PVADs.

FIG. 1.56: Resonance frequencies for 100 PVADs.

FIG. 1.57: Location of 100 PVADs on the fairing.

FIG. 1.58: Genetic algorithm evolution of 100 PVADs.
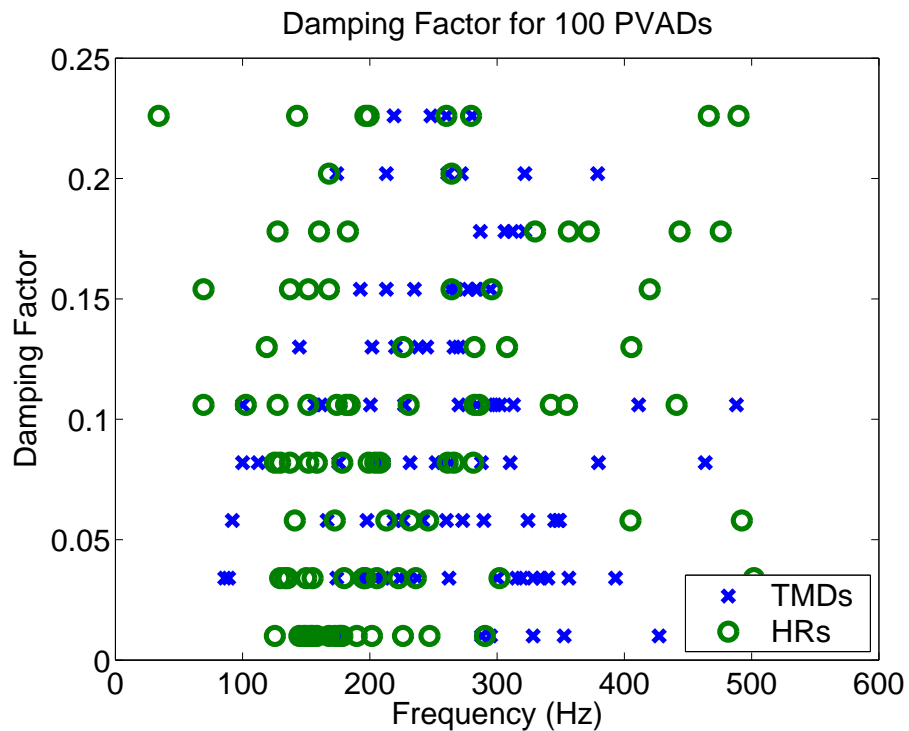
FIG. 1.59: Damping factor versus frequency for 100 PVADs.

Examination of Figure 1.58 shows there is a small dip in the value of the cost function at about 14,000 generations. At this point in the evolution, the genetic algorithm optimisation method was halted and a local gradient descent optimisation method was used. It was suggested in Stage 3A that local gradient descent search algorithms may be of benefit in speeding up the optimisation process. The method employed here involved using a local search for the optimum parameters for a single TMD and HR, whilst all other parameters were kept constant. Hence for this case where 100 PVADs were optimised, the optimisation of each PVAD was farmed out to a computer in the Condor pool of computers. Once the optimisation had completed, the optimum parameters for each PVAD was assembled into the chromosome and the genetic algorithm search method was continued. It can be seen that there was negligible difference in the reduction of the cost function. Hence this method was not beneficial to the optimisation process.
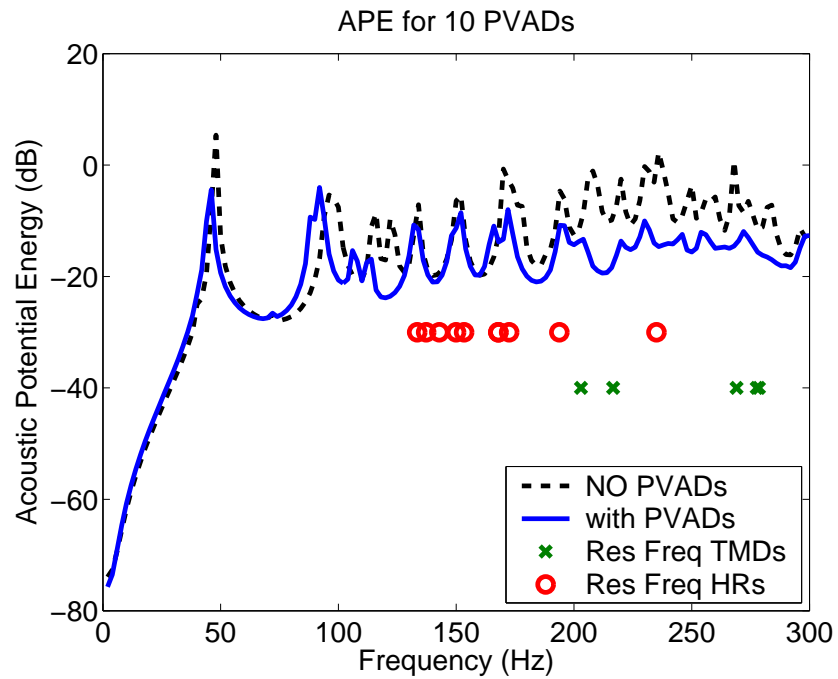
1.9.6 500 PVADs
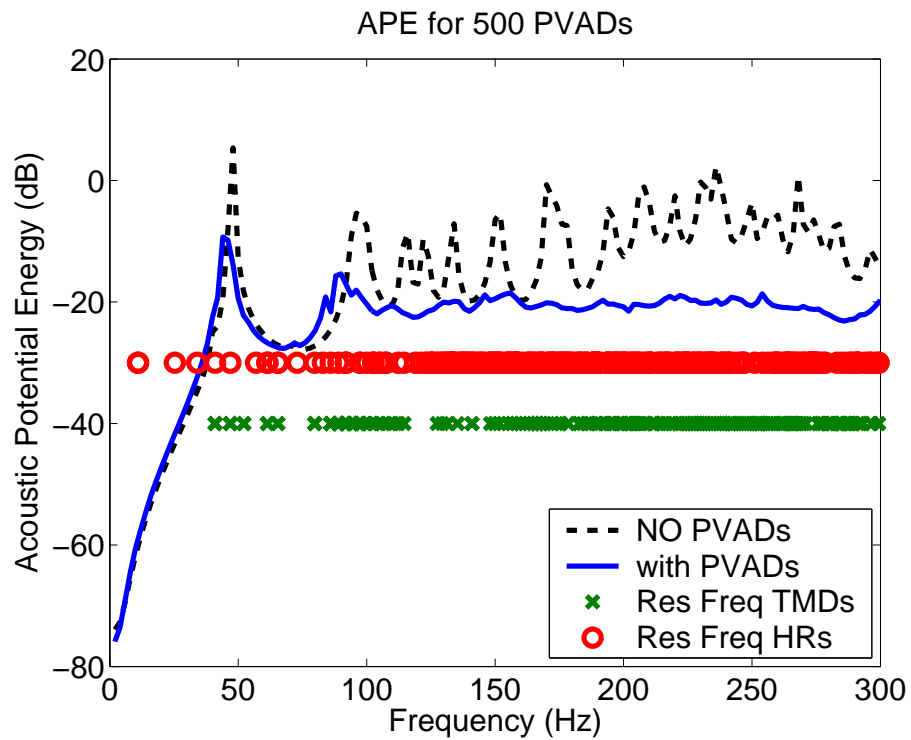
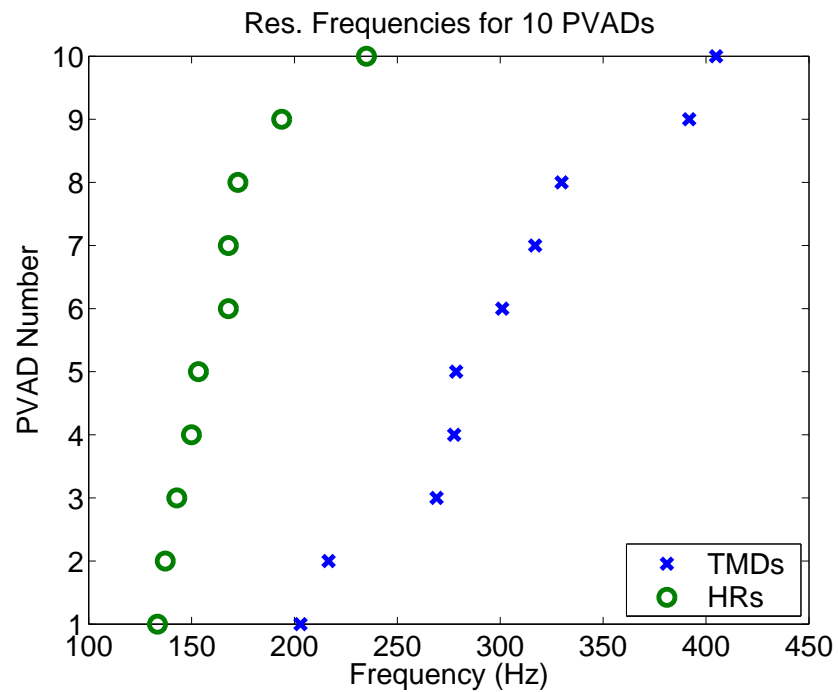FIG. 1.60: Acoustic potential energy versus frequency for 500 PVADs.
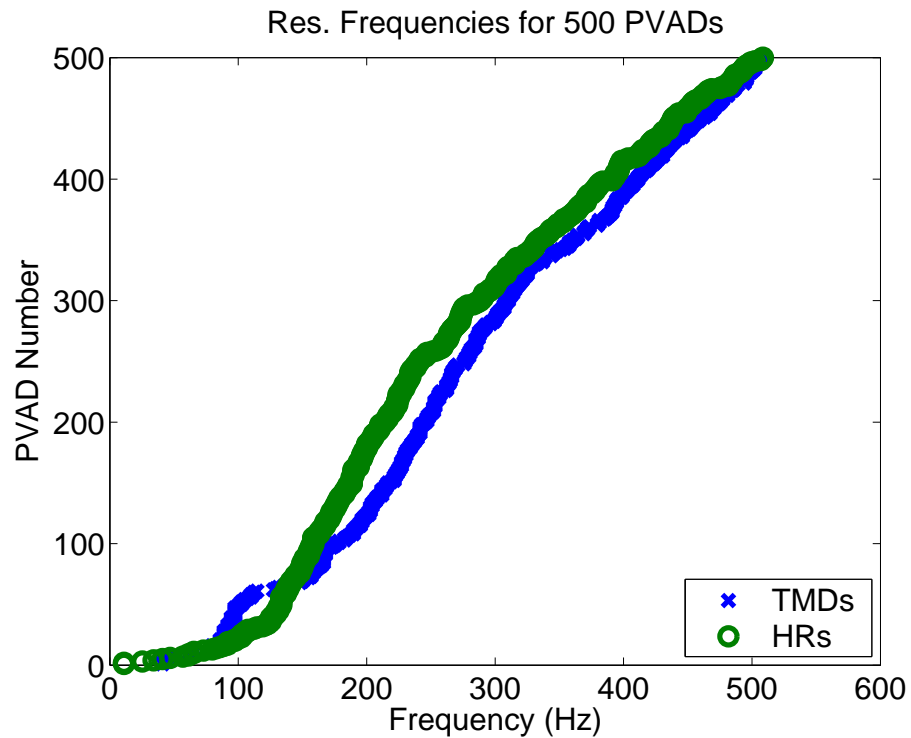
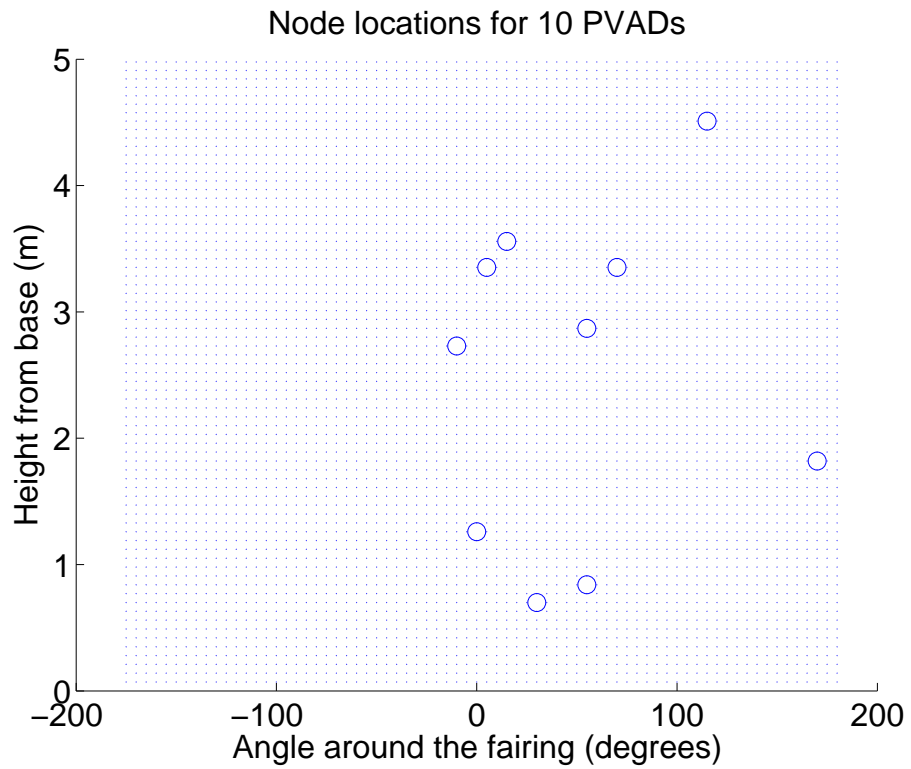FIG. 1.61: Resonance frequencies for 500 PVADs.
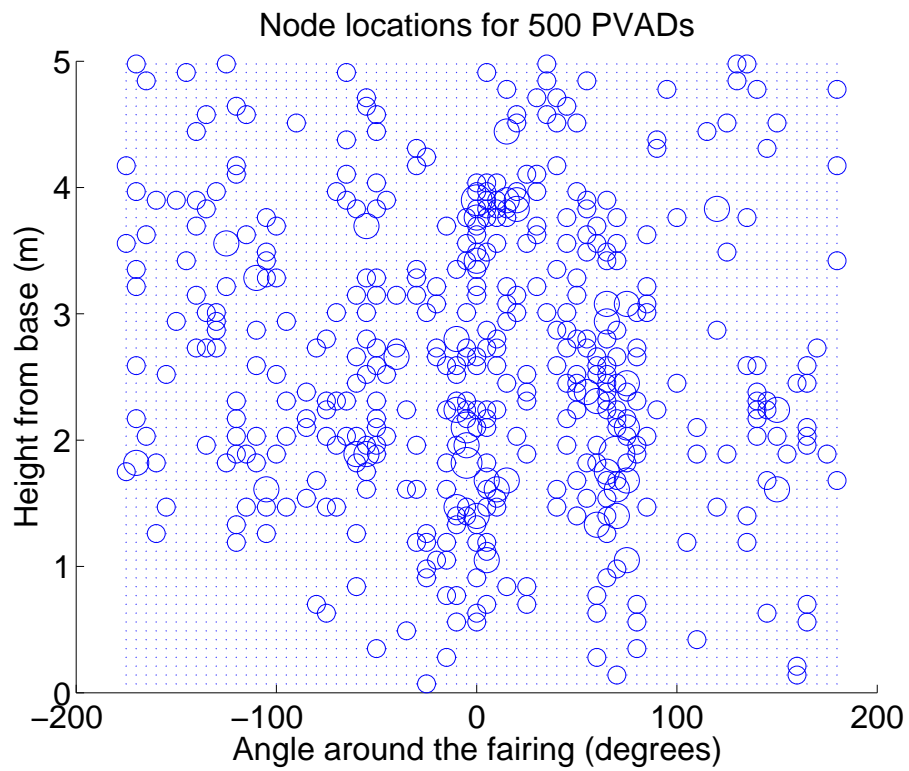
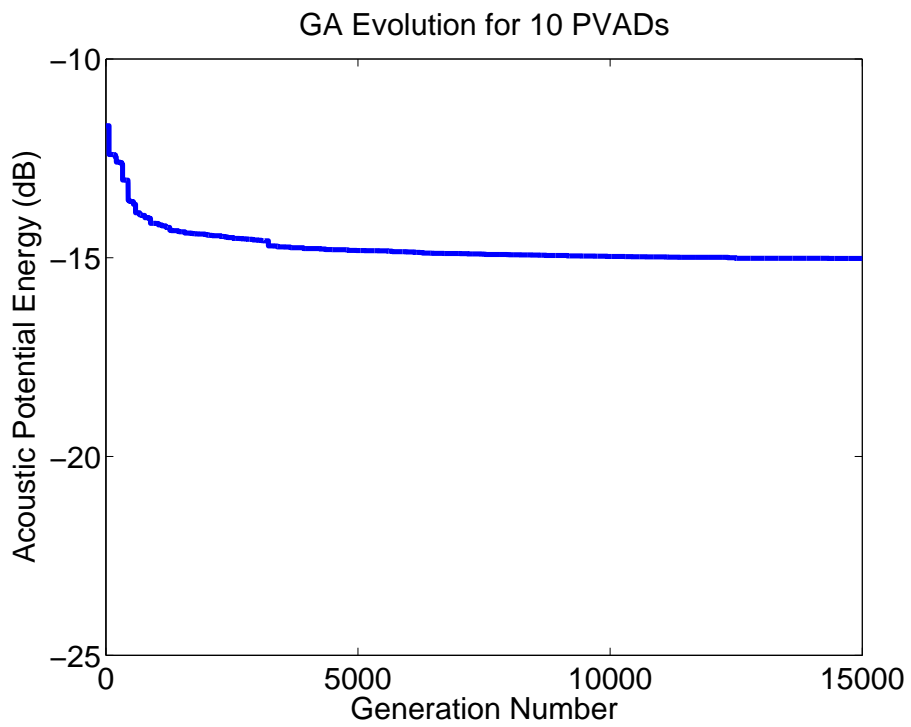FIG. 1.62: Location of 500 PVADs on the fairing.

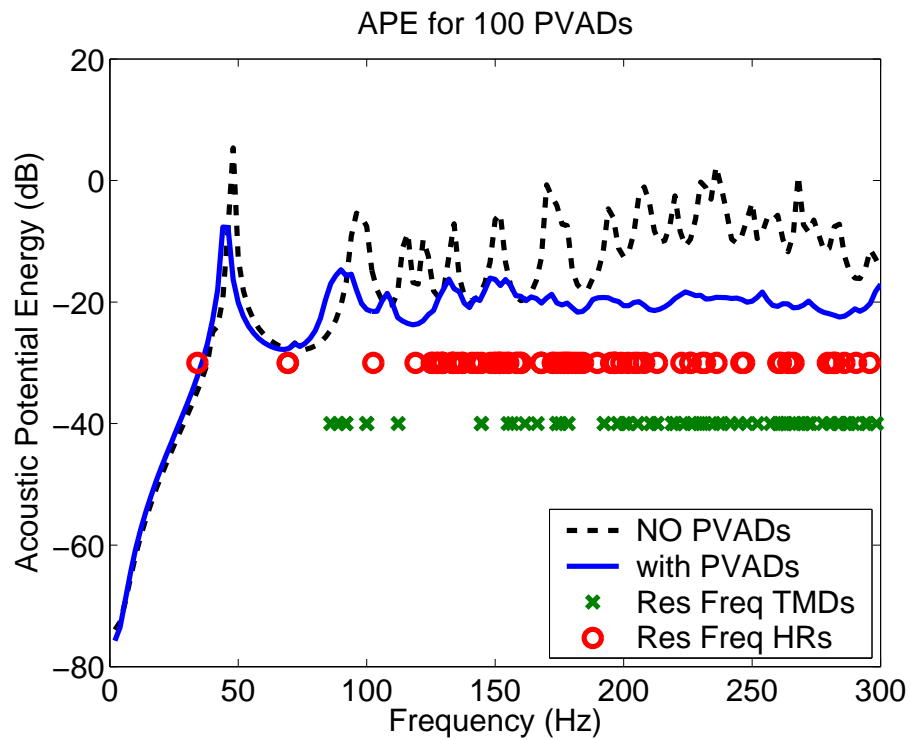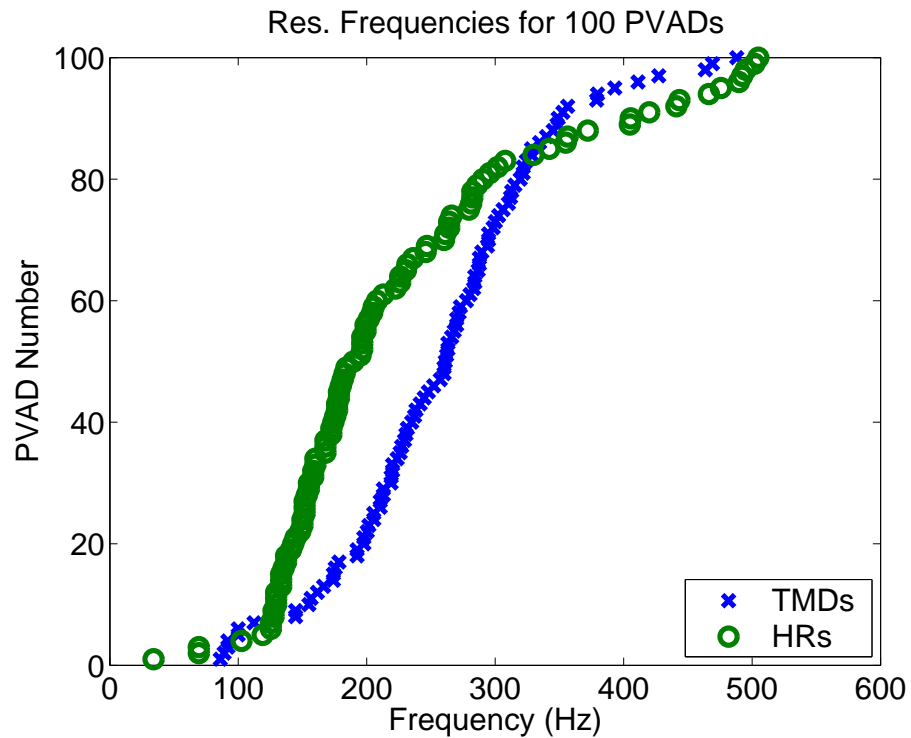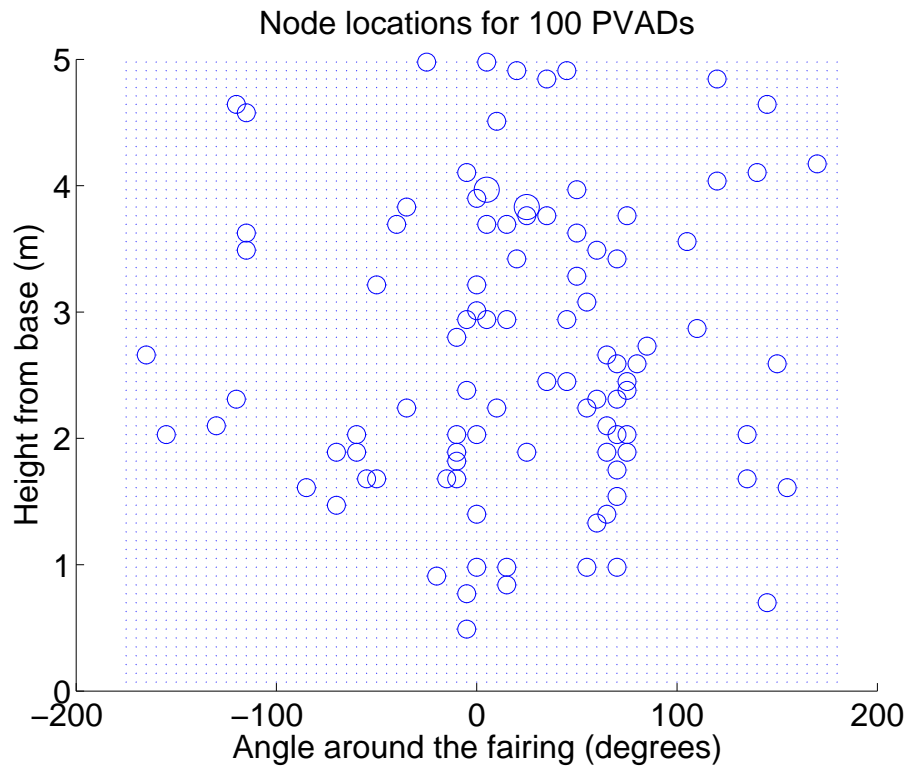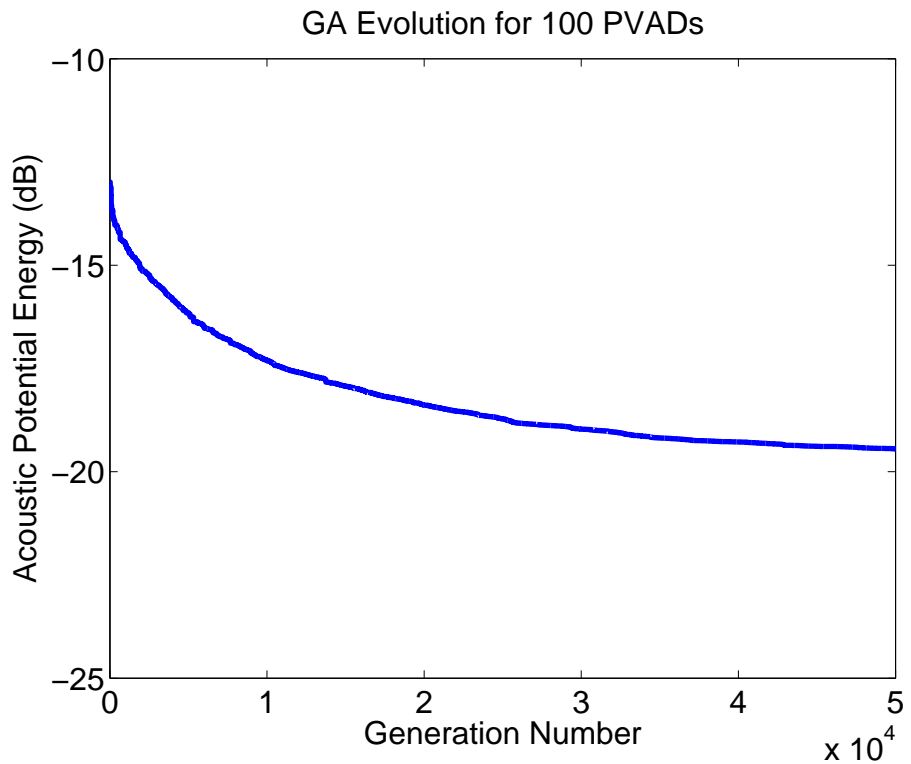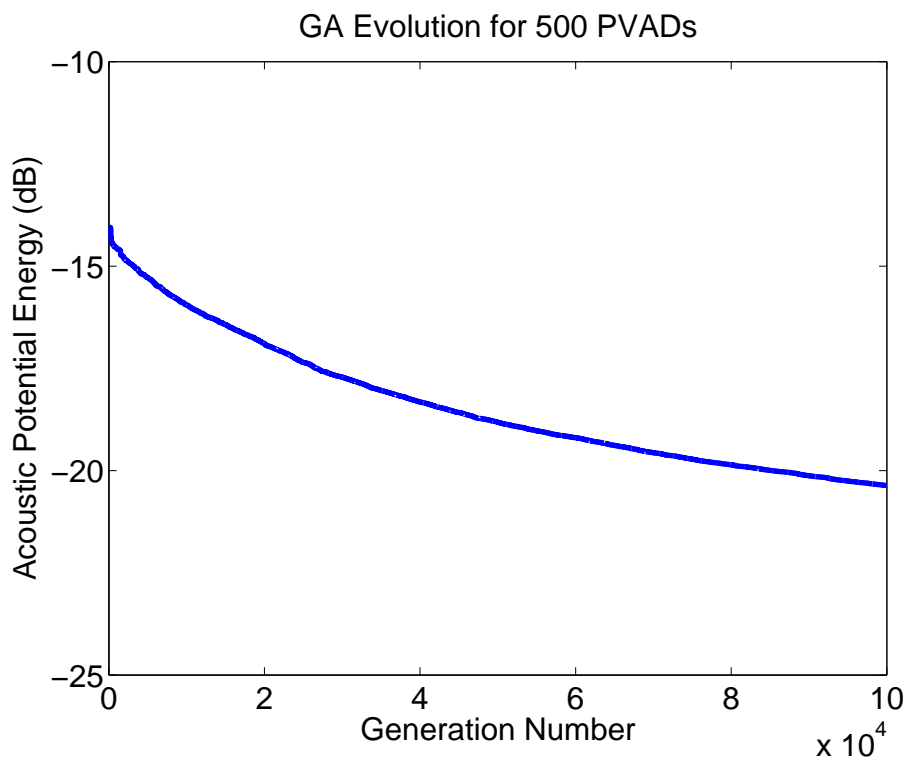FIG. 1.63: Genetic algorithm evolution of 500 PVADs.
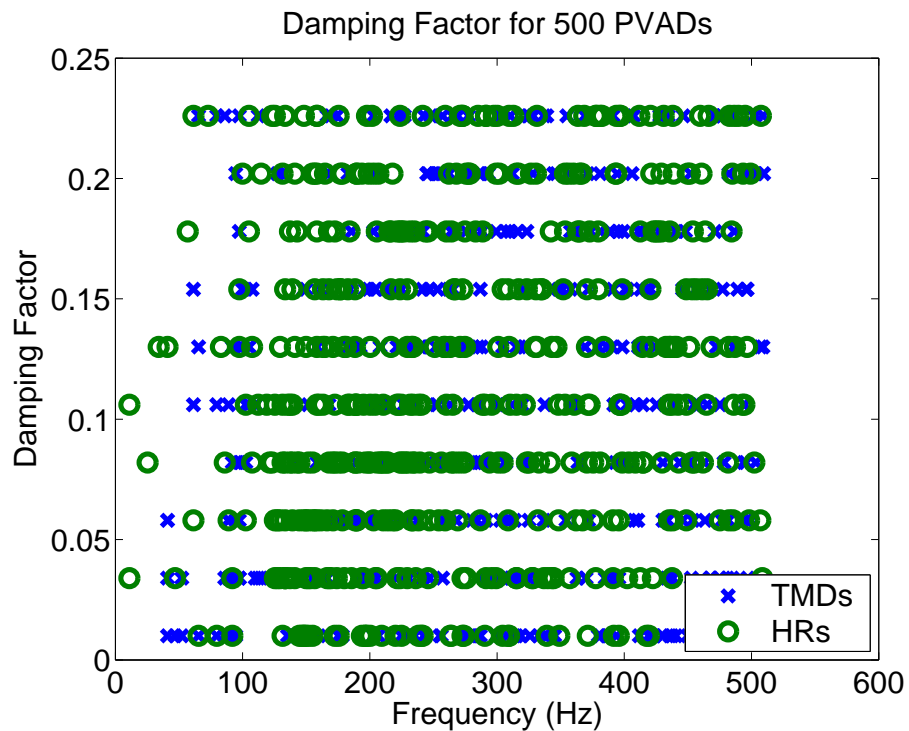
FIG. 1.64: Damping factor versus frequency for 500 PVADs.

Figures 1.50, 1.55, and 1.60 show the APE within the cavity versus frequency for 10, 100, and 500 PVADs, respectively. The results show the trend as the number of PVADs increases, the results for the APE change from mode "splitting" to "fuzzy" structural behaviour.

Figures 1.51, 1.56, and 1.61 show the distribution of the resonance frequencies for the HRs and the TMDs for 10, 100, and 500 PVADs, respectively. The results show a linear distribution of resonance frequencies for both the HRs and the TMDs.

Figures 1.53, 1.58, and 1.63 show the evolution of the genetic algorithm for 10, 100, and 500 PVADs, respectively. The results show that as the number of PVADs increases, the noise reduction improves. This will be further discussed in Section 1.10.

Figure 1.63 shows the evolution of the GA for 500 PVADs attached to the RSLVF. The optimisation involved calculating the cost function approximately 200,000 times (twice the number of generations). On a Pentium 4, 3GHz machine the calculation of a single cost function takes approximately 3 minutes. The computers in the Condor pool have processor speeds in the range of 1.8GHz to 2.4GHz. Hence if this optimisation were to be

done on a 3GHz machine, it would have taken at least 417 days. Using the Condor pool it took less than 2 weeks.

1.9.7 Separating the Helmholtz Resonators and Tuned Mass Dampers

Up to now, it has been assumed that the locations of the HR and TMD reside at the same node. An optimisation was conducted to investigate the benefit of separating the locations of the HRs and the TMDs. The optimisation considered the case where there were 100 HRs and 100 TMDs. Table 1.7 lists the parameter range for the optimisation, which is almost identical to the ranges described in Table 1.6, except that there is an additional parameter for the node location of the HRs, which has the same limits for the location as the TMDs.

Table 1.7: PVAD parameter range for the optimisation of the separated HRs and TMDs.

PVAD parameter	Min	Max	No. Values	Comment
HR position	1	5184	5184	Circumferential nodes
TMD position	1	5184	5184	Circumferential nodes
Mass-spring frequency	11	510	500	[Hz]
Mass-spring damping (η)	0.01	0.25	10	
Acoustic resonator frequency	11	510	500	[Hz]
Acoustic resonator damping (η)	0.01	0.25	10	

Figure 1.65 shows the APE within the fairing versus frequency. The HRs and TMDs form clusters around the peaks in the APE curves, tending to "smear" the energy into the absorbers.

Figure 1.66 shows that the resonance frequencies of the HRs and TMDs have a linear distribtion across the frequency range of interest.

Figure 1.67 shows the locations of the HRs and TMDs on the fairings as the red and blue circles, respectively.

Figure 1.68 shows that the APE within the cavity at the end of the optimisation of the separated HRs and TMDs is approximately -20dB, which is 0.5dB better than that was achieved when the HRs and TMDs were at the same locations, as shown in Figure 1.58.
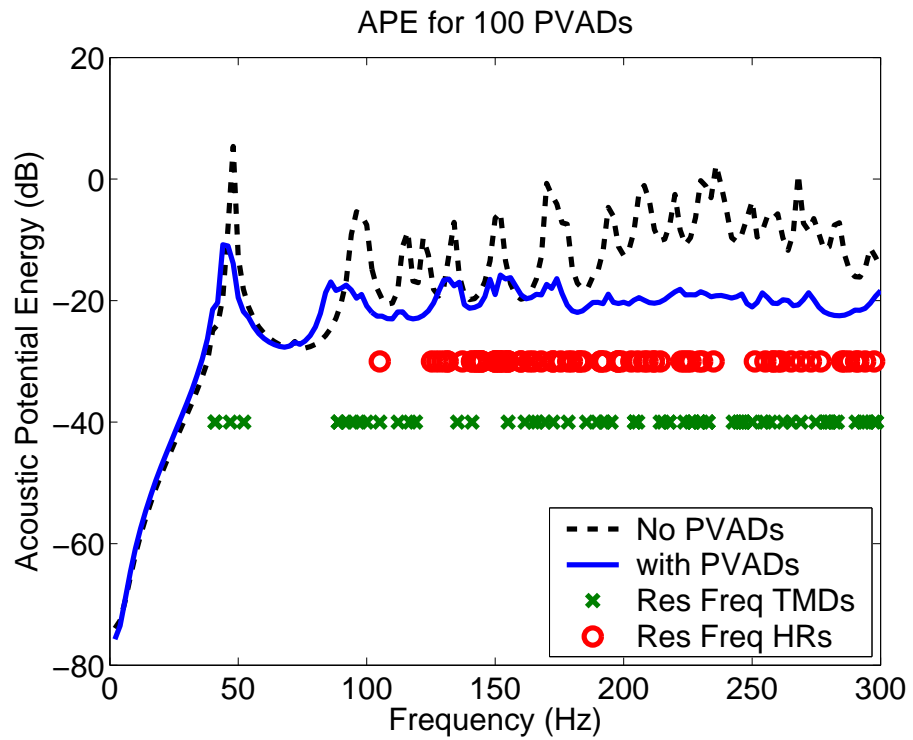
FIG. 1.65: Acoustic potential energy versus frequency for 100 PVADs with separated HRs and TMDs.
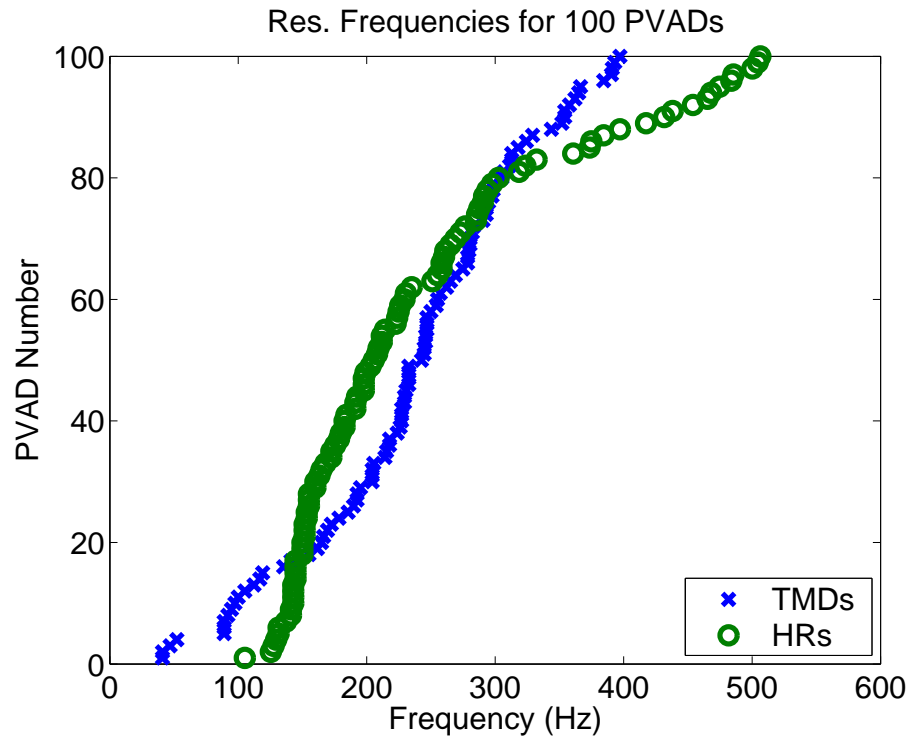
FIG. 1.66: Resonance frequencies for 100 PVADs with separated HRs and TMDs.
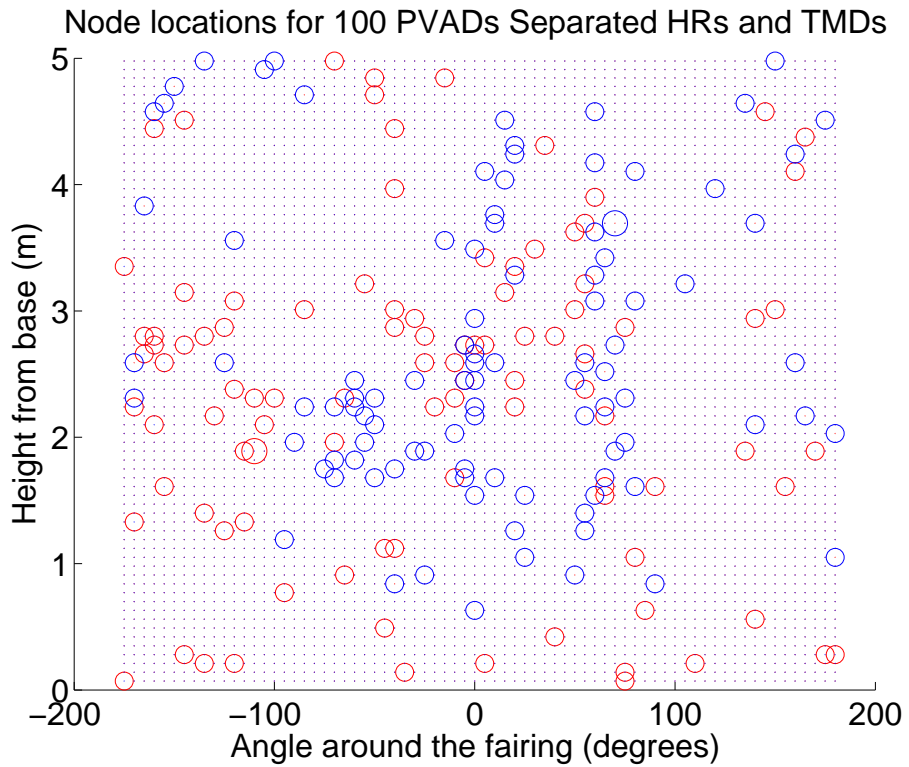
FIG. 1.67: Location of 100 PVADs on the fairing with separated HRs and TMDs. The blue circles are for the TMDs and the red circles are for the HRs.
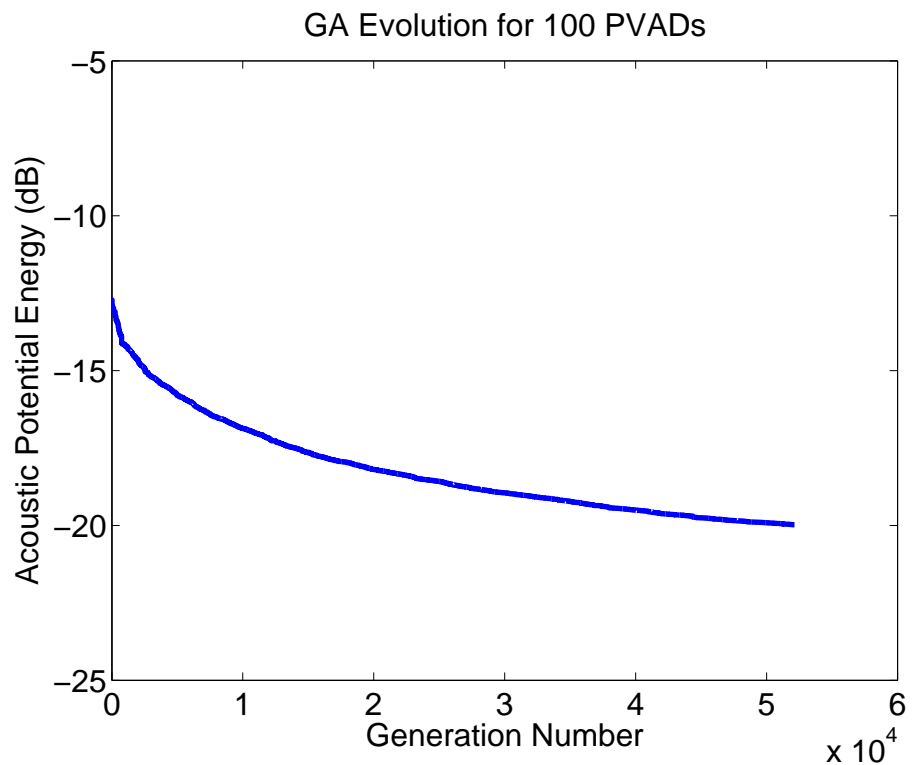
FIG. 1.68: Genetic algorithm evolution of 100 PVADs with separated HRs and TMDs.
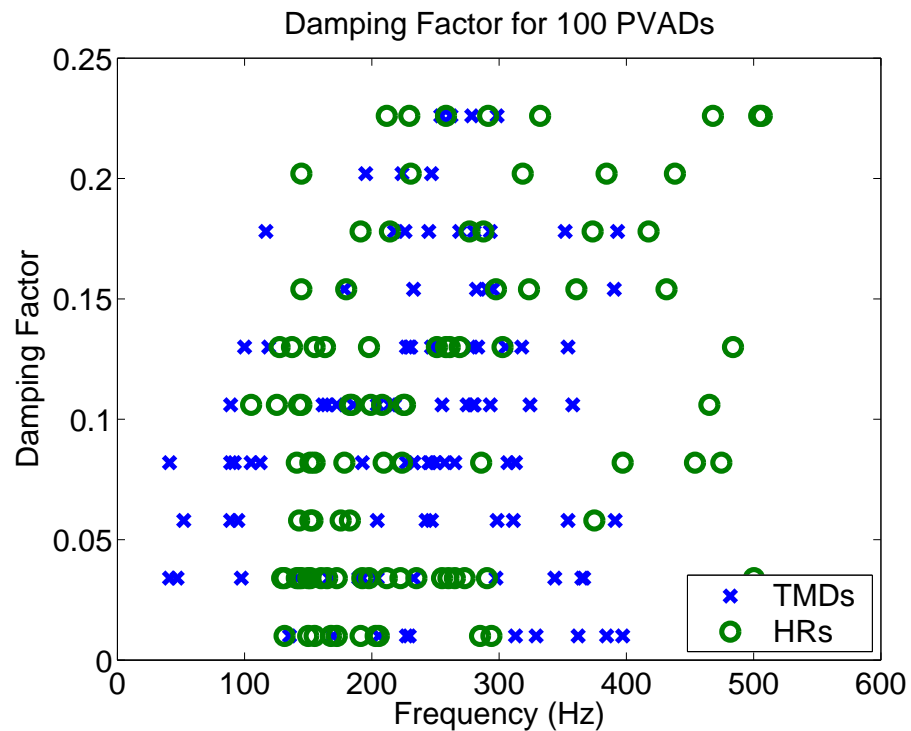
FIG. 1.69: Damping factor versus frequency for 100 PVADs with separated HRs and TMDs.

These results show that there is no benefit to be gained in separating the HRs and the TMDs. This result for the RSLVF is consistent with the results for the optimisation of the separated HRs and TMDs attached to the Boeing cylinder, where the noise reduction was improved by a negligible 0.5dB [2, p60].

1.10   Conclusions

The trends described in Section 1.9, concerning the optimisation of PVADs attached to the walls of the RSLVF, are similar to the trends shown in Section 1.8 for the optimisation of TMDs attached to the rectangular plate:

- Figures 1.50, 1.55, and 1.60 show the trend as the number of PVADs increases, the results for the APE change from mode "splitting" to "fuzzy" structural behaviour.

- Figures 1.51, 1.56, and 1.61 show the linear distribution of resonance frequencies for both the TMDs and the HRs.

- Figures 1.53, 1.58, and 1.63 show that as the number of PVADs increases, the noise reduction improves.

Figure 1.70 shows the decrease in the total acoustic potential energy with the increasing number of PVADs, with a linear scale for the number of PVADs. Figure 1.71 shows the same results as shown in Figure 1.70, but plotted with a logarithmic scale for the number of PVADs. The results show there is an exponentially decreasing improvement in the noise reduction for increasing the number of PVADs. These results show that the greatest noise reduction is obtained for a large number of lightweight dampers.

Total APE vs Number of PVADs

FIG. 1.70: Acoustic potential energy versus the number of PVADs.
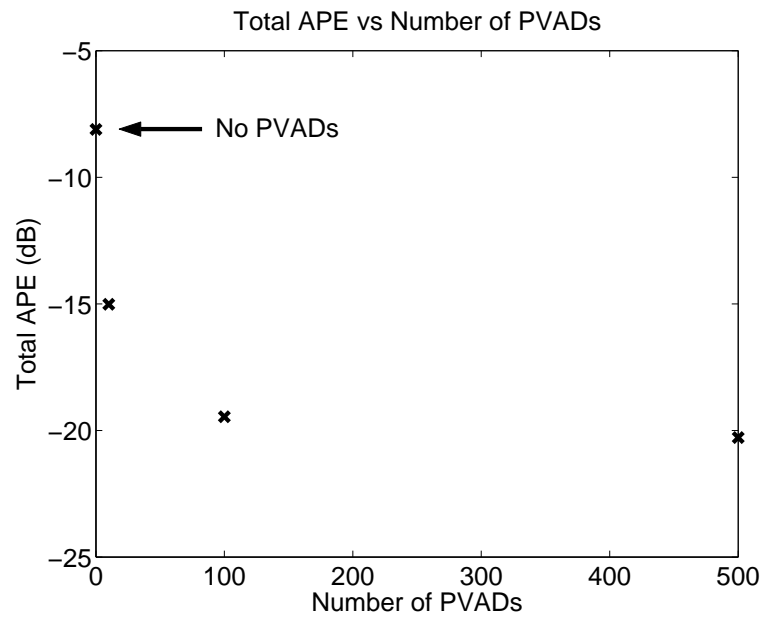
Total APE vs Number of PVADs
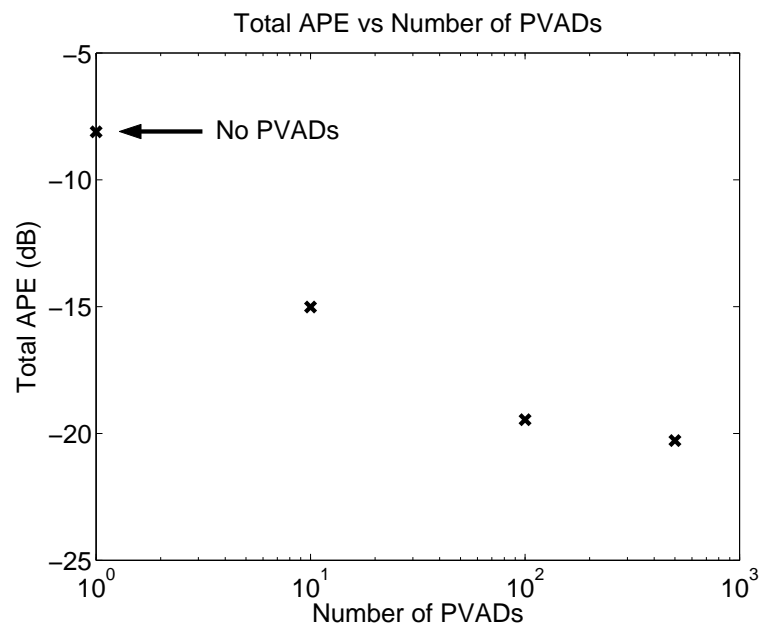
FIG. 1.71: Acoustic potential energy versus the number of PVADs.

Chapter 2

Task 2: Optimal design of multiple degree of freedom vibro-acoustic dampers

This task was labelled "Stage 4 Task 2" in the original proposal in which the work statement was as follows:

The design of a multi-degree-of-freedom vibro-acoustic absorber with rocking modes and a twisting mode in addition to the normal translational modes will be investigated. Key design issues shall be identified and design techniques developed.

2.1   Introduction

The Tuned Vibration Dampers that were considered in the previous analyses in this report and in the previous three stages of the project, all had a single degree of freedom. One concept that was suggested to improve the reduction in vibration levels of the structure, and hence improve the noise reduction was to design a tuned vibration damper that has both translational and rotational degrees of freedom. It was thought that the incorporation of both these degrees of freedom into the one PVAD would provide a compact and effective passive noise control device. This chapter contains the analysis of such a device

that has both translational and rotational degrees of freedom.

Section 2.2 contains the derivation of equations of motion of thin-shelled structure that is excited with both translational forces and rotational moments. Section 2.3 contains the derivation of a tuned vibration damper that has both translational and rotational degrees of freedom in the one device. This device has a cantilever structure, where point masses are attached to the end of flexible arms. The equations of motion for the cantilever TMDs are incorporated into the equations of motion for the structure. Section 2.4 contains the derivation of the coupled vibro-acoustic equations, which includes the effects of the HRs and the cantilever TMDs.

Section 2.5 describes the range of parameters that were considered in the optimisation of the PVADs attached to the walls of the RSLVF. The analyses considered the attachment of 10 and 20 PVADs to the fairing wall. It was considered that more than twenty PVADs could not be physically built within the limits of the analyses considered here. The results of these optimisations are presented in this section.

The mathematical framework developed in Stage 2 was not amenable to extension to multiple degree of freedom dampers. Hence, part of the Stage 3A work included reformulating the modal coupling method to incorporate the Helmholtz resonators and Tuned Mass Dampers that could be extended to multiple degree of freedom systems. This was done by adapting the framework presented in Refs [6, 7]. Hence part of the work that was due only to start in Stage 4 has already been completed. The following section extends the work described in Stage 3A to incorporate a vibration isolator that has twisting modes and is capable of transmitting moments into the base structure.

2.2 Equations of Motion for Moment Loading on Shells

Most vibrational analyses ignore the contribution due to rotational degrees of freedom as it is frequently considered to be less important than the contribution from translational degrees of freedom. However, research has shown that the contribution of rotational degrees of freedom on shell structures often plays a significant part in vibrational power

transmission and cannot be ignored [6].

The multiple degree of freedom vibration dampers, which will be described in Section 2.3, transmit both forces and moments on the structure and hence the equations of motion of the structure must include these loads. This section contains the derivation of the equations of motion of thin shelled structures due to excitation from both translational forces and rotational moments. The theory is developed using Refs [6, 26].

The theoretical development of the application of multiple degree of freedom PVADs to the structure is very similar to existing theoretical models of vibration isolated platforms attached to flexible structures. It is useful to start the development of this framework with a numerical model of the flexible structure, similar to the existing theoretical models, and then in the final stages of the development, the modal results from the finite element analysis can be substituted for the theoretical modal results.

Multiple PVADs are attached to the fairing and each PVAD applies a force to it that can be described in a cylindrical coordinate system as

$$
\mathbf{Q}_J = \begin{bmatrix} F_{xJ} & F_{\theta J} & F_{rJ} & M_{xJ} & M_{\theta J} & M_{rJ} \end{bmatrix}^{\mathrm{T}} \tag{2.1}
$$

where $J = 1, \cdots, L_1$, and there are L_1 PVADs attached to the fairing. Forces are transmitted into the structure along the axis of the fairing (F_{xJ}), tangential to the surface ($F_{\theta J}$), and radially (F_{rJ}). Moments transmitted into the structure and are described using the right-hand-rule about the axis of the fairing (M_{xJ}), tangential to the surface of the fairing ($M_{\theta J}$), and a drilling moment normal to the fairing (M_{rJ}).

The force and moment components in $\mathbf{Q}_J$ are assumed to be concentrated point actions at the joint between the fairing at PVAD location $\boldsymbol{\sigma}_J$ on the thin shell, so that Dirac Delta functions (δ) and their partial derivatives can be used to describe the external force distribution on the fairing.

The motion of the fairing could be described by the Donnell-Mushtari thin-shell theory [27] which uses eighth order differential equations. These equations can be simplified if the radius R of the shell is significantly large compared to the shell thickness h. In this

case the vibration of the fairing is primarily radial, with the axial x and tangential θ displacements being small enough to allow the corresponding inertia terms in the axial and tangential directions in the equation of motion of the fairing to be neglected. Forces acting in the axial x and tangential θ directions excite vibration in these directions which in turn couple with the radial vibration to produce vibration in the radial w direction but at a much smaller amplitude. The radial vibration amplitude produced in this way is considered small compared to the radial vibration produced directly by moments and radial forces.

Note that the axial and tangential forces produced on the inside surface of the fairing produce moments about the mid-surface of the shell which result in direct excitation of radial motion. This is taken into account in the following analysis.

The response of the fairing can be described as [26]

$$\ddot{\eta}_k + 2\zeta_k \omega_k \dot{\eta}_k + \omega_k^2 \eta_k = F_k \tag{2.2}$$

where η_k is the kth modal participation factor, ζ_k is the viscous damping of the shell at the kth mode, ω_k is the resonance frequency of the kth mode and F_k is the kth modal force which is applied to the shell for the kth mode and is defined as

$$F_k = \frac{1}{\rho h N_k} \int_0^{2\pi} \int_0^{\frac{L}{R}} \left\{ \begin{array}{l} q_s U_{sk} + q_\theta U_{\theta k} + q_w U_{wk} \\[2mm] + \dfrac{U_{sk}}{2R} \dfrac{\partial\left(-T_n\right)}{\partial \theta} - \dfrac{U_{\theta k}}{2R} \dfrac{\partial\left(-T_n\right)}{\partial s} + \dfrac{U_{\theta k}}{R} T_s \\[4mm] + \dfrac{U_{wk}}{R^2} \left[\dfrac{\partial\left(-T_\theta R\right)}{\partial s} + \dfrac{\partial\left(T_s R\right)}{\partial \theta} \right] \end{array} \right\} R^2 ds d\theta \tag{2.3}$$

where q_i and T_i represent the forces and moments applied along each of the three axes, defined as

$$q_{iJ} = \frac{F_{iJ}}{R^2} \delta(s - s_J) \delta(\theta - \theta_J) e^{j\omega t} \tag{2.4}$$

$$T_{iJ} \;=\; \frac{M_{iJ}}{R^2}\delta(s - s_J)\delta(\theta - \theta_J)\,e^{j\omega t} \tag{2.5}$$

F_i and M_i are the forces and moments applied to the shell at location $\boldsymbol{\sigma}_J$ in the directions $i = s, \theta, w$, U_{ik} is the modal response in the ith direction, δ is the Dirac delta function and

$$N_k = \int_0^{2\pi}\int_0^{\frac{L}{R}}\left\{U_{1k}^2 + U_{2k}^2 + U_{3k}^2\right\}R^2 ds d\theta \tag{2.6}$$

Equation (2.3) is not the same as printed in Soedel [26]. It was found by the author that terms were missing which account for the moment loading to the shell. This has been corrected in Eq. (2.3) provided in this report. A detailed description of the correction is given in Ref [6].

The terms on the left hand side of the integral in Eq. (2.3) equate to the inverse of modal mass of the fairing. The integral terms account for the translational force and rotational moment loads on the fairing.

We shall assume that the in-plane displacement of the fairing is not significant and does not contribute to the overall vibration response of the fairing [6, 7]. Only the out-of-plane vibration shall be considered in this analysis. Theoretically, there is a small degree of coupling from the in-plane vibration to the out-of-plane vibration; however the magnitude is small and can be ignored [6]. Hence the following relationships can be used to describe the displacement of the fairing

$$U_{sk} \;=\; 0 \tag{2.7}$$

$$U_{\theta k} \;=\; 0 \tag{2.8}$$

$$U_{wk} \;=\; [\boldsymbol{\Psi}]\mathbf{w}_p \tag{2.9}$$

The mode shapes $[\boldsymbol{\Psi}]$ of the structure are calculated using the ANSYS finite element analysis software, and $\mathbf{w}_p$ is the vector of modal participation factors.

The force and moment loads on the fairing are assumed to be point loads, which can

be described with Dirac delta functions. Making use of the relationships

$$\int_\alpha F(\alpha)\frac{\partial}{\partial \alpha}\left[\delta(\alpha - \alpha^*)\right] d\alpha = -\frac{\partial F(\alpha^*)}{\partial \alpha} \tag{2.10}$$

the integral in Eq. (2.3) can be evaluated as

$$F_k = \frac{1}{\Lambda_p}\left[[\psi_J]^{\mathrm{T}}F_J - \frac{\partial[\psi_J]^{\mathrm{T}}}{\partial y}M_{Jx} + \frac{\partial[\psi_J]^{\mathrm{T}}}{\partial x}M_{Jy}\right] \tag{2.11}$$

The rotations of the fairing about $\boldsymbol{\sigma}_J$ are given by [26, 27]

$$\theta_s = \frac{v}{R} - \frac{1}{R}\frac{\partial w}{\partial \theta} \tag{2.12}$$

$$\theta_\theta = -\frac{1}{R}\frac{\partial w}{\partial s} \tag{2.13}$$

$$\theta_w = \frac{1}{2R^2}\left\{R\frac{\partial v}{\partial s} - R\frac{\partial u}{\partial \theta}\right\} \tag{2.14}$$

The partial differential of the mode shapes $[\psi]$ are the mode shapes in the rotational directions. The ANSYS software calculates these rotational mode shapes, which can be extracted for use with the modal coupling software implemented in Matlab. Eq. (2.11) can be written as

$$F_k = \frac{1}{\Lambda_p}\left[[\psi_J]^{\mathrm{T}}F_J - [\psi_{J\theta x}]^{\mathrm{T}}M_{Jx} + [\psi_{J\theta y}]^{\mathrm{T}}M_{Jy}\right] \tag{2.15}$$

where $[\psi_{J\theta x}]$ and $[\psi_{J\theta y}]$ are the rotational mode shapes about the θ_x and θ_y axes, respectively. These rotational mode shapes are calculated in ANSYS and are extracted and converted into units that are consistent with the translational mode shapes. Appendix B.2 describes the calculation of the rotational mode shapes in ANSYS and Appendix B.3 describes a verification procedure to confirm that the mode shapes were extracted correctly.

The rotational mode shapes from ANSYS are described using the global Cartesian coordinate system. The theoretical development in this section assumes that the rota-

tional mode shapes are in an orthogonal coordinate system that has an axis normal to the surface of the structure. Appendix B.4 describes the transformation of the ANSYS mode shapes from the Cartesian coordinate system to a pseudo-cylindrical coordinate system that is aligned with the normal to the surface of the structure.

2.3 Equations of Motion for Cantilevered Tuned Vibration Damper

One concept for a tuned vibration damper that can transmit both translational forces and rotational moments is a device that consists of point masses that are cantilevered from a central shaft [28–30]. The resonance frequencies of the damper are adjusted by changing the lengths of the cantilever arms. This section contains the equations of motion of a dual cantilever vibration damper and the integration of these equations into the equations of motion of the structure developed in Section 2.2.

Figure 2.1 shows a mathematical model of the two mass cantilevered tuned vibration damper.
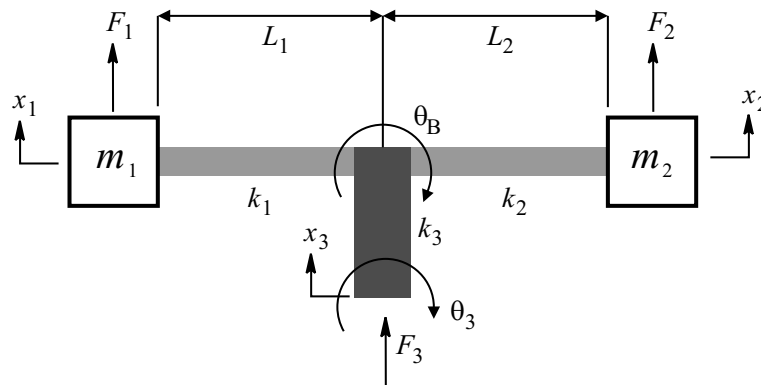
FIG. 2.1: Mathematical model of the two mass cantilevered tuned vibration dampers.

It is assumed that:

- Point masses are located on the ends of the cantilever arms.

- The rotation of the masses is negligible so the rotational inertia of the masses is ignored.

- The masses of the arms are negligible compared to the point masses and hence can be ignored from the point of view of the system dynamics.

- The central column has very high axial stiffness compared to the bending stiffness of the arms, so that the axial stiffness of the column can be assumed infinite.

- The central column has bending flexibility.

The tuned vibration damper has two masses m_1 and m_2 on the ends of cantilever arms that have lengths L_1 and L_2, respectively. The transverse stiffnesses of these arms, k_1 and k_2, are given by

$$k_1 \quad = \frac{3E_1I_1}{L_1^3} \quad \text{(N/m)} \tag{2.16}$$

$$k_2 \quad = \frac{3E_2I_2}{L_2^3} \quad \text{(N/m)} \tag{2.17}$$

where E and I are the Young's modulus and moment of inertia, respectively. The rotational stiffness of the upright central column is given by

$$k_3 = \frac{E_3I_3}{L_3} \quad \text{(Nm/radians)} \tag{2.18}$$

The following pages describe the derivation of the equations of motion of the damper. The equations of motion for mass 1 are given by

$$m_1\ddot{x}_1 = F_1 - k_1[x_1 - (x_3 + L_1\theta_B)] \tag{2.19}$$

$$x_1(k_1 - \omega^2 m_1) + x_2(0) + x_3(-k_1) + \theta_B(-k_1L_1) = F_1 \tag{2.20}$$

The equations of motion for mass 2 are given by

$$m_2\ddot{x}_2 = F_2 - k_2[x_2 - (x_3 - L_2\theta_B)] \tag{2.21}$$

$$x_1(0) + x_2(k_2 - \omega^2 m_2) + x_3(-k_2) + \theta_B(k_2L_2) = F_2 \tag{2.22}$$

The sum of forces at the junction between the cantilever arms and the central column is given by

$$0 = F_3 + k_1[x_1 - (x_3 + L_1\theta_B)] + k_2[x_2 - (x_3 - L_2\theta_B)] \tag{2.23}$$

$$x_1(-k_1) + x_2(-k_2) + x_3(k_1 + k_2) + \theta_B(k_1L_1 - k_2L_2) = F_3 \tag{2.24}$$

The sum of moments at the junction between the cantilever arms and the central column is given by

$$0 = L_1k_1[x_1 - (x_3 + L_1\theta_B)] - L_2k_2[x_2 - (x_3 - L_2\theta_B)] + k_3(\theta_B - \theta_3) \tag{2.25}$$

$$x_1(L_1k_1) + x_2(-L_2k_2) + x_3(-L_1k_1 + L_2k_2)$$

$$+\theta_B(-L_1k_1L_1 - L_2k_2L_2 + k_3) + \theta_3(-k_3) = 0 \tag{2.26}$$

The sum of the moments at the base of the isolator is given by

$$-(m_1 + m_2)L_3^2\omega^2\theta_3 = -k_3(\theta_B - \theta_3) + M_3 \tag{2.27}$$

$$\theta_B(k_3) + \theta_3(-k_3 - (m_1 + m_2)L_3^2\omega^2) = M_3 \tag{2.28}$$

Eqs (2.20), (2.22), (2.24), (2.26), and (2.28) can be combined into matrix form as

$$
\begin{bmatrix}
k_1 - \omega^2 m_1 & 0 & -k_1 \\
0 & k_2 - \omega^2 m_2 & -k_2 \\
-k_1 & -k_2 & k_1 + k_2 \\
L_1 k_1 & -L_2 k_2 & \begin{Bmatrix} -L_1 k_1 \\ +L_2 k_2 \end{Bmatrix} \\
0 & 0 & 0
\end{bmatrix} \cdots
$$

$$
\cdots \begin{bmatrix}
-k_1 L_1 & 0 \\
k_2 L_2 & 0 \\
k_1 L_1 - k_2 L_2 & 0 \\
\begin{Bmatrix} -L_1 k_1 L_1 \\ -L_2 k_2 L_2 \\ +k_3 \end{Bmatrix} & -k_3 \\
k_3 & \begin{Bmatrix} -k_3 \\ -(m_1 + m_2)L_3^2 \omega^2 \end{Bmatrix}
\end{bmatrix}
\begin{bmatrix} x_1 \\ x_2 \\ x_3 \\ \theta_B \\ \theta_3 \end{bmatrix}
=
\begin{bmatrix} F_1 \\ F_2 \\ F_3 \\ 0 \\ M_3 \end{bmatrix}
\tag{2.29}
$$

It can be shown that this matrix equation can be reduced to eliminate the terms for x_3, θ_3, and θ_B so that the matrix equation reduces to

$$
\begin{bmatrix}
\mathbf{A}_{11} & \mathbf{A}_{12} & \mathbf{A}_{13} \\
\mathbf{A}_{21} & \mathbf{A}_{22} & \mathbf{A}_{23} \\
\mathbf{A}_{31} & \mathbf{A}_{32} & \mathbf{A}_{33}
\end{bmatrix}
\begin{bmatrix} x_1 \\ x_2 \\ w_p \end{bmatrix}
=
\begin{bmatrix}
F_1 \\
F_2 \\
\begin{Bmatrix} \sum_J [\psi_J]^{\mathrm{T}} F_J \\ -[\psi_{J\theta x}]^{\mathrm{T}} M_{Jx} \\ +[\psi_{J\theta y}]^{\mathrm{T}} M_{Jy} \end{Bmatrix}
\end{bmatrix}
\tag{2.30}
$$

Appendix B.5 describes the algebraic derivation and the terms $\mathbf{A}_{11}$ to $\mathbf{A}_{33}$.

2.4 Equations of Motion for the Fully Coupled System

This section describes the integration of the vibration response of the structure, which includes the effects of the cantilever vibration dampers, with the acoustic response of the cavity, which includes the effects of the HRs, to result in equations that describe the coupled vibro-acoustic system.

Section 2.3 described the equations of motion for the cantilevered vibration damper. The design proposed here involves using two of these devices orientated at 90 degrees to each other. Hence the equations of motion for the structural system will contain two sets of the $\mathbf{A}$ matrices described in Eq. (2.30). The matrices for the structural equations will be

$$
\begin{bmatrix}
\begin{bmatrix} \mathbf{A}_{11}^A & \mathbf{A}_{12}^A \\ \mathbf{A}_{21}^A & \mathbf{A}_{22}^A \end{bmatrix} & \begin{bmatrix} \mathbf{0} & \mathbf{0} \\ \mathbf{0} & \mathbf{0} \end{bmatrix} & \begin{matrix} \mathbf{A}_{13}^A \\ \mathbf{A}_{23}^A \end{matrix} \\
\begin{bmatrix} \mathbf{0} & \mathbf{0} \\ \mathbf{0} & \mathbf{0} \end{bmatrix} & \begin{bmatrix} \mathbf{A}_{11}^B & \mathbf{A}_{12}^B \\ \mathbf{A}_{21}^B & \mathbf{A}_{22}^B \end{bmatrix} & \begin{matrix} \mathbf{A}_{13}^B \\ \mathbf{A}_{23}^B \end{matrix} \\
\begin{matrix} \mathbf{A}_{31}^A & \mathbf{A}_{32}^A \end{matrix} & \begin{matrix} \mathbf{A}_{31}^B & \mathbf{A}_{32}^B \end{matrix} & \mathbf{A}_{33}^A + \mathbf{A}_{33}^B
\end{bmatrix}
\begin{bmatrix} x_1^A \\ x_2^A \\ x_1^B \\ x_2^B \\ w_p \end{bmatrix}
=
\begin{bmatrix} F_1^A \\ F_2^A \\ F_1^B \\ F_2^B \\ \left\{ \begin{matrix} \sum_J [\psi_J]^{\mathrm{T}} F_J \\ -[\psi_{J\theta x}]^{\mathrm{T}} M_{Jx} \\ +[\psi_{J\theta y}]^{\mathrm{T}} M_{Jy} \end{matrix} \right\} \end{bmatrix}
\tag{2.31}
$$

It can be seen that the format of this matrix equation is similar to the $\mathbf{A}$ matrices in Eq. (1.19). Hence it is possible to incorporate this matrix equation into the fully-coupled vibro-acoustic theory developed in Section 1.5 where

$$
\mathbf{A'}_{11} =
\begin{bmatrix}
\begin{bmatrix} \mathbf{A}_{11}^A & \mathbf{A}_{12}^A \\ \mathbf{A}_{21}^A & \mathbf{A}_{22}^A \end{bmatrix} & \begin{bmatrix} \mathbf{0} & \mathbf{0} \\ \mathbf{0} & \mathbf{0} \end{bmatrix} \\
\begin{bmatrix} \mathbf{0} & \mathbf{0} \\ \mathbf{0} & \mathbf{0} \end{bmatrix} & \begin{bmatrix} \mathbf{A}_{11}^B & \mathbf{A}_{12}^B \\ \mathbf{A}_{21}^B & \mathbf{A}_{22}^B \end{bmatrix}
\end{bmatrix}
\tag{2.32}
$$

$$\mathbf{A'}_{12} = \begin{bmatrix} \mathbf{A}_{13}^A \\ \mathbf{A}_{23}^A \\ \mathbf{A}_{13}^B \\ \mathbf{A}_{23}^B \end{bmatrix} \tag{2.33}$$

$$\mathbf{A'}_{21} = \begin{bmatrix} \mathbf{A}_{31}^A & \mathbf{A}_{32}^A & \mathbf{A}_{31}^B & \mathbf{A}_{32}^B \end{bmatrix} \tag{2.34}$$

$$\mathbf{A'}_{22} = \begin{bmatrix} \mathbf{A}_{33}^A + \mathbf{A}_{33}^B \end{bmatrix} \tag{2.35}$$

2.5 Optimisation Method

Optimisations were conducted on the RSLVF fairing for the location and parameters of the cantilevered tuned mass dampers and Helmholtz resonators. The optimisations were conducted for 10 and 20 PVADs attached to the fairing.

There is an identical mass on the end of each of the four arms on each PVAD, which together make up the total mass of the PVAD. The added mass to the fairing was set at 10% of the total mass of the fairing. The mass of the fairing is about 67kg. Hence the allowable added mass is about 6.7kg. If this is evenly divided into 20 PVADs, then each PVAD will weigh 335 grams, and the mass on the end of each of the four cantilever arms will be 84 grams. This is probably near the practical limits of a real cantilevered vibration damper. Hence the optimisation of 20 PVADs is the maximum number of dampers that was investigated.

The parameters were allowed to vary as listed in Table 2.1.

In order to reduce the number of parameters to be optimised, the geometry of some of the components of the TMDs was assumed, as listed in Table 2.2.

Using the parameters described in Tables 2.1 and 2.2, the range of resonance frequencies for the TMDs is between approximately 40Hz and 1400Hz.

Table 2.1: PVAD parameter range for the optimisation of the RSLVF with cantilevered vibration dampers.

PVAD parameter	Min	Max	No. Values	Comment
PVAD position	1	5184	5184	Circumferential nodes
Cantilever arm lengths	0.01	0.1	500	[m]
Mass-spring damping (η)	0.01	0.25	10	
Acoustic resonator frequency	11	510	500	[Hz]
Acoustic resonator damping (η)	0.01	0.25	10	

Table 2.2: Assumed parameters for the cantilevered vibration dampers.

Parameter	Value	Units	Comment
Young's modulus of arm	70.9	GPa	Aluminium
Moment of inertia of arm	52.08e-12	m^4	5mm diameter rod
Young's modulus of upright column	130	GPa	Stiff light-weight material
Moment of inertia of upright column	32.55e-9	m^4	25mm diameter rod

2.5.1 10 PVADs
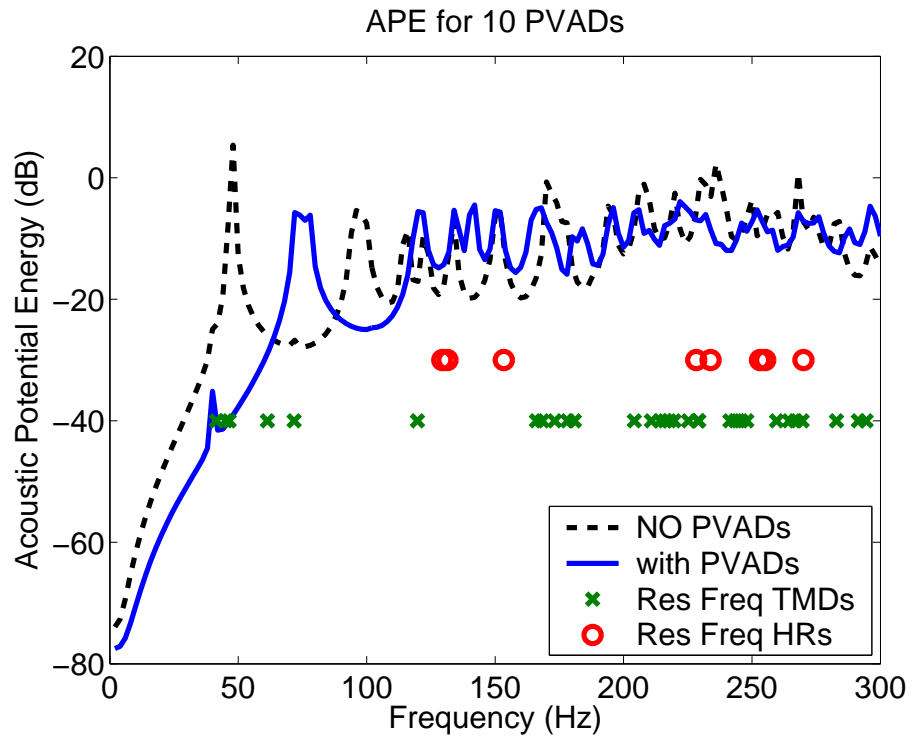
FIG. 2.2: Acoustic potential energy versus frequency for 10 PVADs.

FIG. 2.3: Resonance frequencies for 10 PVADs.
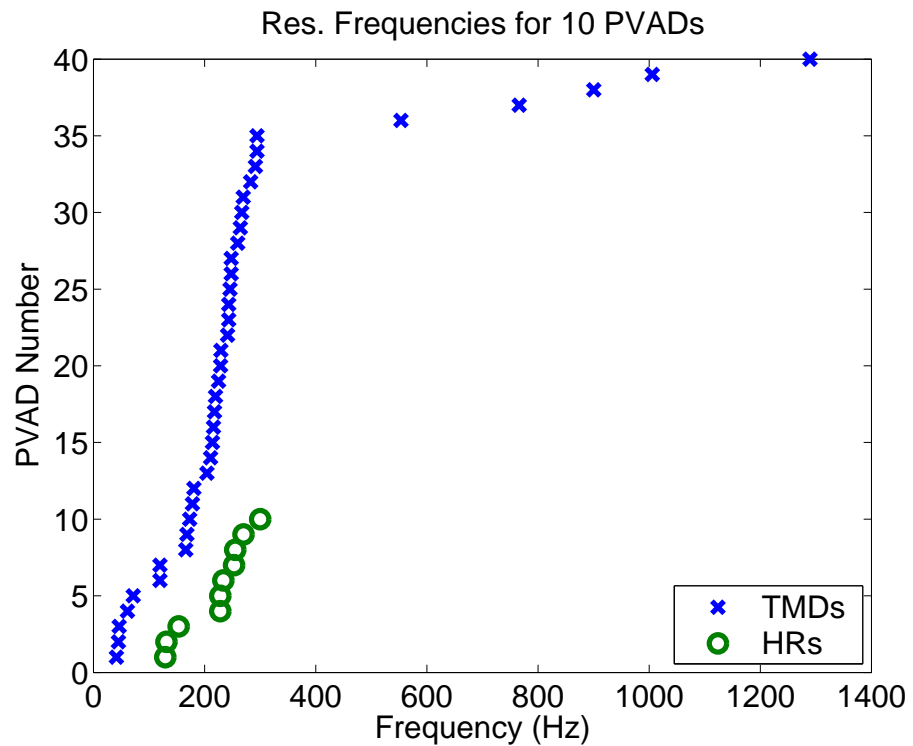
Node locations for 10 PVADs

FIG. 2.4: Location of 10 PVADs on the fairing.

Node locations for 10 cantilever PVADs
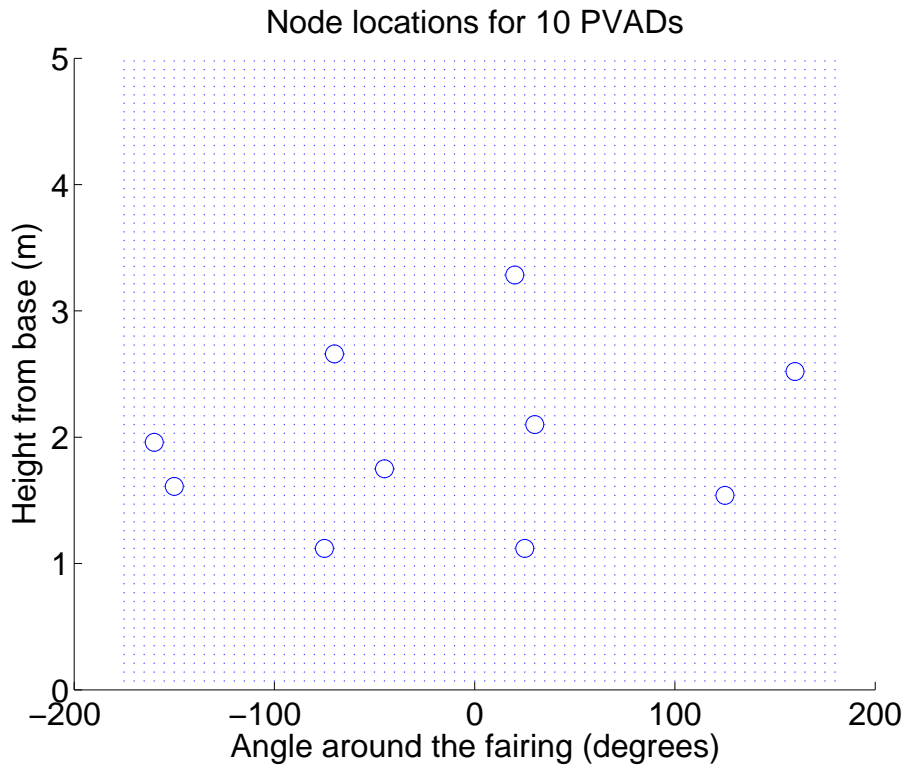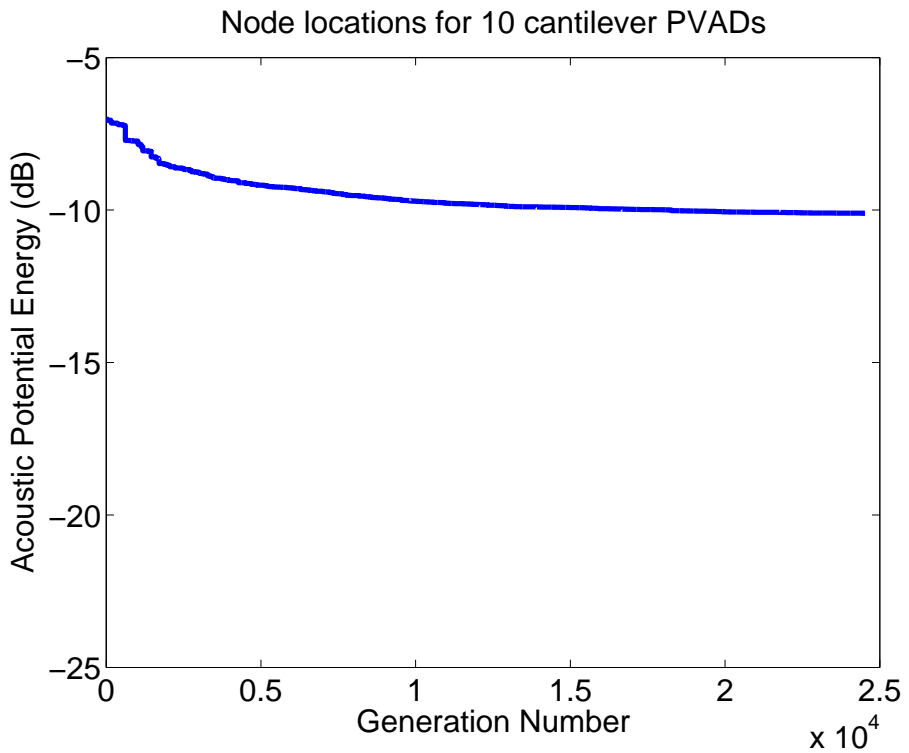
FIG. 2.5: Genetic algorithm evolution of 10 PVADs.
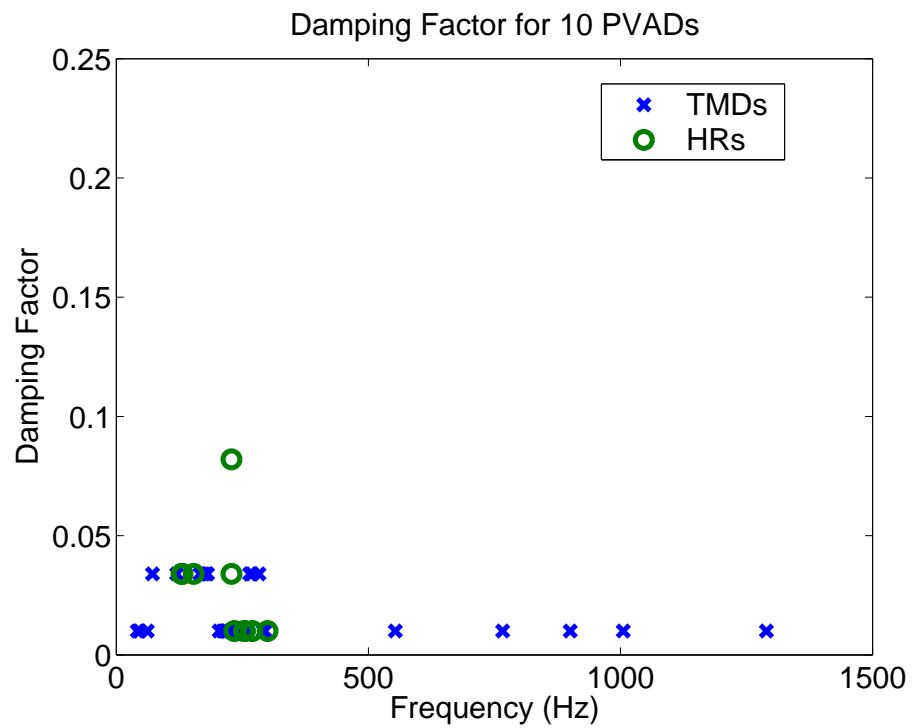
FIG. 2.6: Damping factor versus frequency for 10 PVADs.

2.5.2 20 PVADs
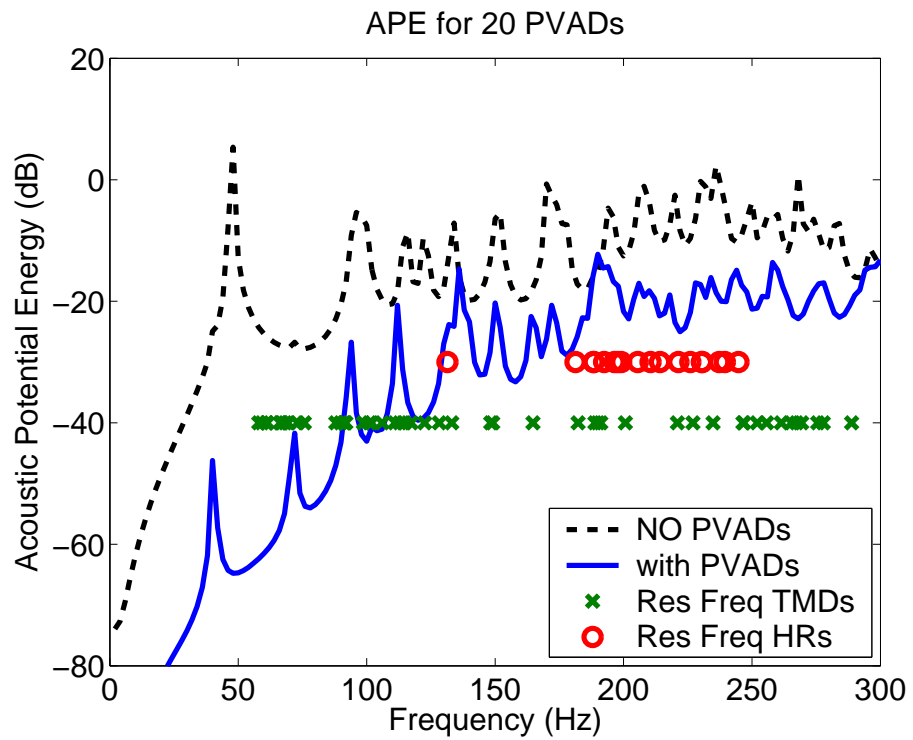
FIG. 2.7: Acoustic potential energy versus frequency for 20 PVADs.
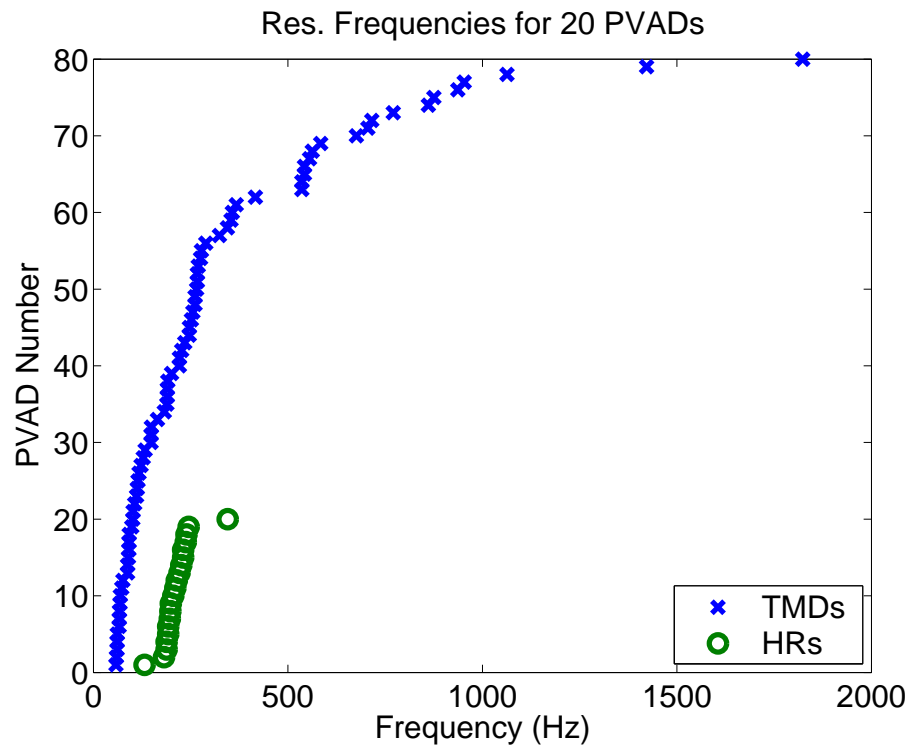
FIG. 2.8: Resonance frequencies for 20 PVADs.
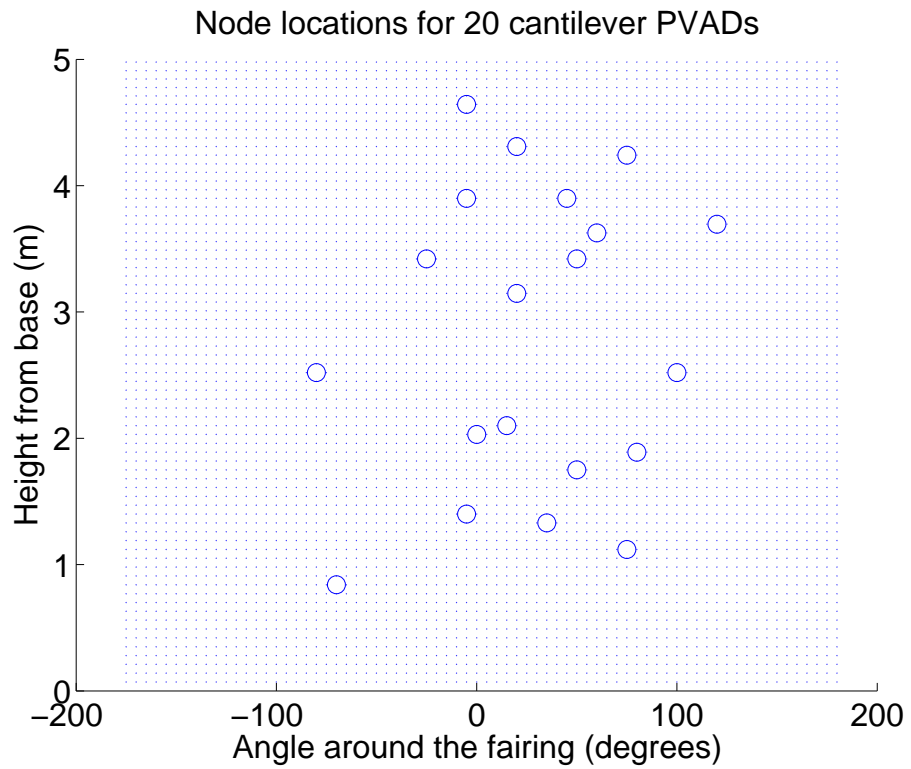
FIG. 2.9: Location of 20 PVADs on the fairing.
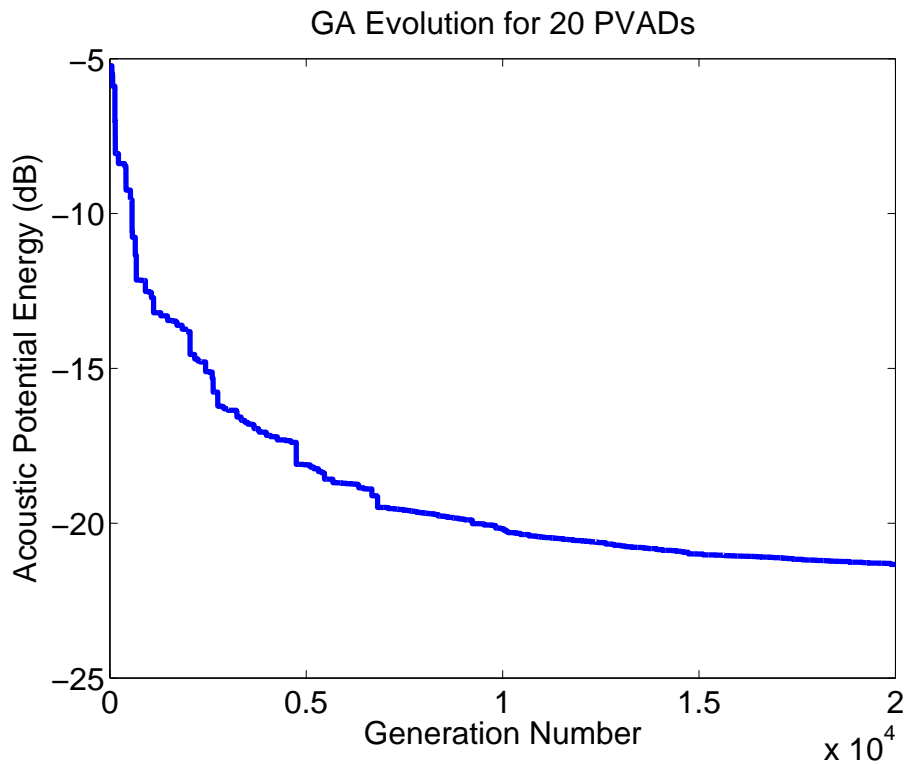
FIG. 2.10: Genetic algorithm evolution of 20 PVADs.
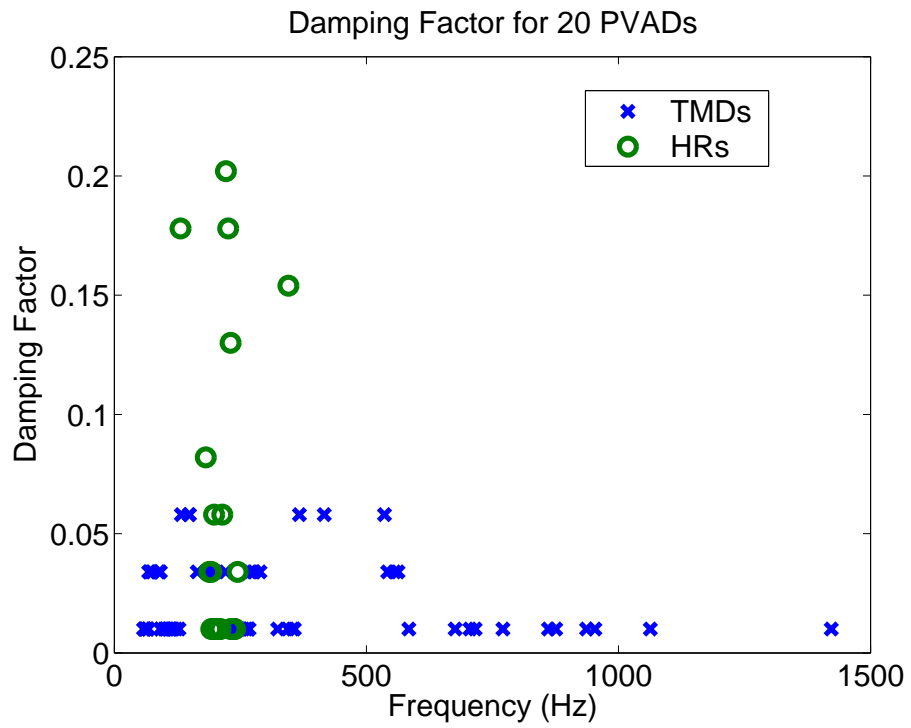
FIG. 2.11: Damping factor versus frequency for 20 PVADs.

2.5.3   Comparison with 500 Single DOF PVADs

Figure 2.12 shows the APE within the cavity for no PVADs, 500 single degree of freedom PVADs, and 20 cantilever PVADs attached to the walls of the fairing. The results show that the use of the 20 cantilever PVADs, which are capable of transmitting rotational moments to the fairing, affects the APE in the low frequency region, whereas the 500 single degree of freedom PVADs has a smoothing effect in the frequency region from 100-300Hz.
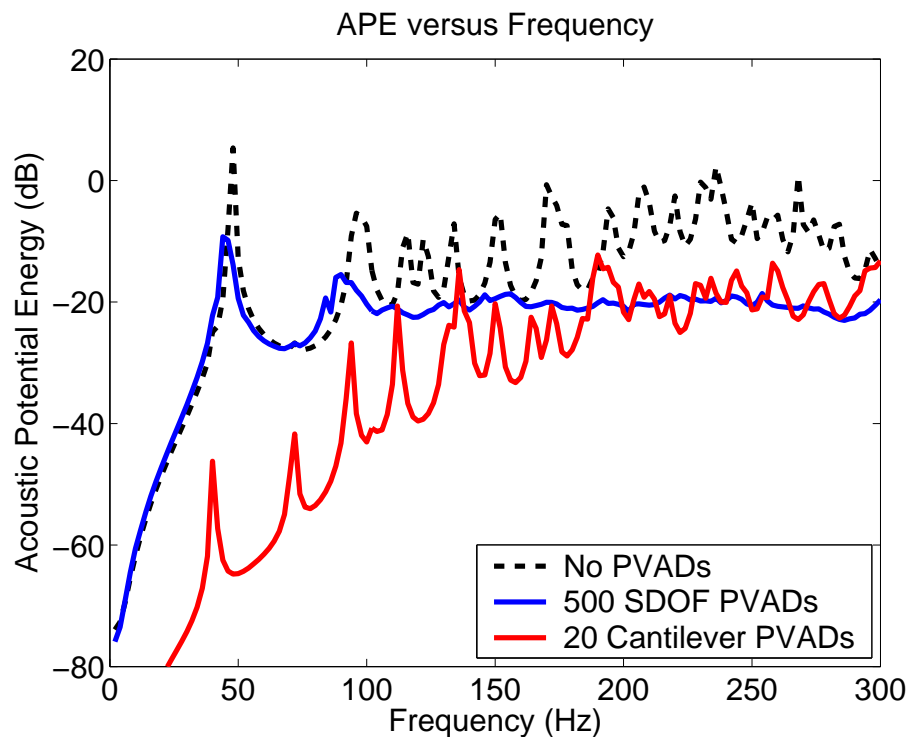
FIG. 2.12: Acoustic potential energy versus frequency for no PVADs, 500 single degree of freedom PVADs, and 20 cantilever PVADs.

2.6   Conclusions

Figure 2.3 and 2.8 show that there is a linear distribution of resonance frequencies for the cantilever TMDs and the HRs, which is consistent with the trends identified in Section 1.10 for the single degree of freedom TMDs. Figure 2.12 shows that the spectral shapes for the large number of single DOF PVADs and the small number of multiple DOF PVADs are different, indicating that the energy removal mechanisms are different. The large number of single DOF PVADs have the effect of "smearing" the vibrational energy into the large number of vibration dampers attached to the structure. The small number of multiple DOF PVADs have the effect of mode "splitting", which is evident by the creation of new peaks in the APE, indicating that new resonances have been created.

Figure 2.13 shows the total APE within the fairing versus the number of PVADs, for the single degree of freedom PVADs and the cantilever PVADs that have 4 masses per PVAD. The results indicate that the cantilever PVADs have the potential to provide the same or better noise reduction than the single DOF PVADs, however there is a practical limit to the size of the cantilever PVADs. If it were possible to create miniature lightweight cantilever PVADs, then one would expect the same "smearing" effect could be created as shown in Figure 2.12 for the large number of single DOF PVADs. The results show that the greatest noise reduction was achieved using 20 cantilever PVADs. However, further investigation is warranted to investigate the sensitivity of the noise reduction for varying acoustic loading conditions. The optimal solution should be insensitive to loading conditions. This will be investigated in a future task, as described in Section 3.2.
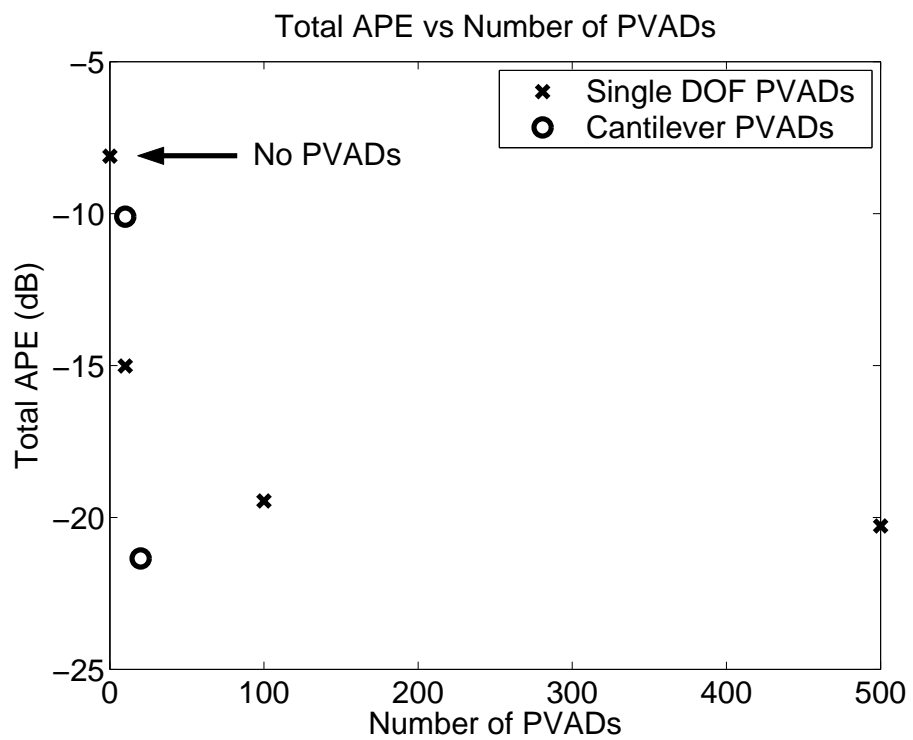
FIG. 2.13: Comparison of the total APE versus the number of PVADs for the single degree of freedom PVADs and the cantilever PVADs.

Chapter 3

Conclusions

3.1 Current Findings

This report contains the results from the optimisation of passive noise and vibration control devices attached to the walls of a Representative Scale Launch Vehicle Fairing. The devices are used to improve the noise reduction characteristics of the fairing walls, so as to minimise the sound pressure level inside the fairing due to an external acoustic excitation.

The first task described in this report included the development of an improved numerical method to calculate the coupled vibro-acoustic response of a structure-cavity system. The new method that was developed reduced the calculation time by about half compared to the method that was used in previous stages of this project. This analysis was tool was used with a genetic algorithm on a distributed computing network to calculate the optimum parameters for the noise control devices that would minimise the acoustic potential energy in the cavity. These tools were applied to an example problem to identify trends in the results of the optimisations. The example problem was a model of a rectangular cavity and rectangular plate system, with tuned mass dampers attached to the plate. The results showed that greatest noise reduction could be achieved by attaching a large number of light-weight absorbers to the panel, compared to attaching a small number of heavy-weight absorbers. An additional advantage was that the noise reduction that was

achieved using a large number of light-weight absorbers was relatively insensitive to the locations of the dampers on the plate.

The second task described in this report involved the development of a theoretical model of a multiple degree of freedom tuned mass damper that is capable of transmitting both translational forces and rotational moments to the structure to which it is attached. The realisation of such a device was based on a device that had been built and tested in this school of mechanical engineering for the attenuation of noise from electrical transformers. The device had four cantilever arms with masses attached to the ends of each of the arms. A theoretical analysis of such a device was undertaken here and the dynamics of the device was incorporated into the coupled vibro-acoustic equations developed in the first task. Optimisations were conducted using 10 and 20 of these devices attached to the walls of the fairings.

In summary, the notable results from this report are

- The time taken to calculate the cost function was reduced by 50% by re-formulating the problem, which reduced the number of matrix multiplications.

- The occurrence of 'fuzzy structure' behaviour with a large number of dampers attached to a vibrating structure was identified and described.

- The results of the optimisation that had the best noise reductions were obtained when the resonance frequencies for the tuned vibration dampers and the Helmholtz resonators had a linear distribution over the frequency range of interest.

- A theoretical framework for the application of multiple degree of freedom dampers attached to the vibrating fairing was developed.

- The results from the optimisation with the multiple degree of freedom tuned mass dampers showed that the same amount of noise reduction could be achieved using 20 multiple DOF PVADs as using 500 single-DOF PVADs. However, the sensitivity of these devices to variations in the acoustic excitation of the fairing is yet to

be investigated. This investigation is planned for the updated Task 4.4, which is described in Section 3.2.

3.2 Future Work

The remaining three tasks listed in the original contract documents are:

Task 4.3: Incorporation of Practical Phenomenon into the Modeling and Design Process

Having developed efficient computation methods in Task 4.1, and having developed improved PVAD devices in Task 4.2, the contractor shall study the effects of the following practical phenomena:

- *structural anomalies - including a vent, a separation seam, and / or a variation in the boundary conditions, and*

- *Acoustic fill - including the determination of the effect of having a rigid payload and a resonant payload in the interior volume.*

Task 4.4: Incorporation of Measured Data into Modeling and Design Tools

The contractor shall replace the FE modal data with actual measured modal data for the structure, cavity and VADs to provide a more accurate prediction of the performance and determine the optimal configuration of the VADs for best performance.

Task 4.5: Final Report

The contractor shall prepare a final report documenting Stage 4 results and providing a summary of relevant earlier stage work.

As agreed with Dr Steve Lane of Kirtland Air force base, the project technical monitor and part sponsor, Task 4.4 will be replaced with

4.4 Sensitivity of results to various acoustic loading conditions. The contractor shall examine the sensitivity of the acoustic performance to several acoustic loading conditions

such as perpendicular plane harmonic waves, oblique plane harmonic waves, and oblique plane waves with random phase that strike the circumference of the rocket fairing and determine the optimal configuration of VADs for best performance.

Appendix A

Dirac Delta Function Properties

The model of the Tuned Mass Dampers used in this report assumes that they vibrate only along one translational axis. It is possible to extend the mathematical framework to include multiple degrees of freedom, including torsional vibration. To include torsional vibration, one can convert point moments into force couples using Dirac delta functions as described below. The force couples are then applied to the model the same way as the translational forces are applied to the model as described in this report. References [6, 7] provide further details.

1. Figure A.1 shows a point force F_z acting in the Z direction on point $\sigma_J(x_J, y_J)$ on a support structure which is equivalent to a distributed load $F_z\delta(x - x_J, y - y_J)$.
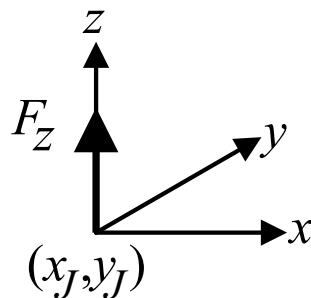
FIG. A.1: Point force F_z

2. Figure A.2 shows a point moment M_y, around the Y axis, which is equivalent to a pair of point forces in the Z direction of $\frac{M_y}{2\epsilon}\delta(x - x_J + \epsilon, y - y_J)$ and $-\frac{M_y}{2\epsilon}\delta(x - x_J - \epsilon, y - y_J)$ when $\epsilon \overset{\lim}{\to} 0$, they correspond to a distributed load

$$\lim_{\epsilon \to 0} \frac{M_y}{2\epsilon} \delta(x - x_J + \epsilon, y - y_J) - \frac{M_y}{2\epsilon}\delta(x - x_J - \epsilon, y - y_J)$$
$$\to M_y \frac{\partial \delta(x - x_J, y - y_J)}{\partial x} \tag{A.1}$$
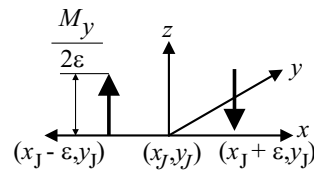
FIG. A.2: Point moment M_y

3. Similarly, a point moment around the X axis, M_x, is equivalent to a distributed load in the Z direction

$$-M_x \frac{\partial \delta(x - x_J, y - y_J)}{\partial y} \tag{A.2}$$

4. Integral of Dirac delta functions

$$\int_\sigma \Gamma_k(\sigma)\delta(\sigma - \sigma_J)d\sigma = \Gamma_k(\sigma_J) \tag{A.3}$$

5. Integral of the partial derivatives of Dirac delta functions

$$\int_\sigma \Gamma_k(\sigma)\frac{\partial \delta(\sigma - \sigma_J)}{\partial x}\, d\sigma$$
$$= \lim_{\epsilon \to 0} \int_\sigma \frac{1}{2\epsilon}\Gamma_k(\sigma)\Big\{ \delta(x - x_J + \epsilon, y - y_J)$$
$$\qquad\qquad -\delta(x - x_J - \epsilon, y - y_J) \Big\}d\sigma$$
$$= \lim_{\epsilon \to 0} \frac{1}{2\epsilon}\{\Gamma_k(x_J - \epsilon, y_J) - \Gamma_k(x_J + \epsilon, y_J)\}$$
$$= -\frac{\partial \Gamma_k(\sigma_J)}{\partial x}$$
$$= -\Gamma_{kx}(\sigma_J) \tag{A.4}$$

Appendix B

Cantilevered Vibration Damper

This appendix contains the derivation of the equations of motion of a tuned vibration damper that has point masses attached to the ends of cantilever arms. The device under consideration here consists of two cantilever arms, which can transmit both translational forces and rotational moments to the structure to which it is attached. The method of influence coefficients is used to derive the equations of motion [31]. These equations of motion are implemented in a Matlab program and the results of static and dynamic analyses are compared with an equivalent model implemented in the ANSYS FEA software. The results of the two models are identical, indicating that the method of modelling the cantilevered vibration dampers is correct. The equations that describe the stiffness of the various components of the cantilever tuned vibration damper are used in the mathematical model in Section 2.3.

A model of one such tuned-vibration damper is shown in Figure B.1. This ANSYS model has four cantilevers extending from a central shaft. Each opposite pair of cantilevers can vibrate in phase, which generates a translational force along the central shaft, or it can vibrate out of phase, which generates a rotational moment. Note that the graphical representation from ANSYS shows that the central column has a square section, however mathematically it is calculated as a shaft with a circular cross section.

For the present, we shall only consider a tuned vibration damper that has two cantilever arms, and the theory will be extended to include four cantilever arms in Section 2.4.
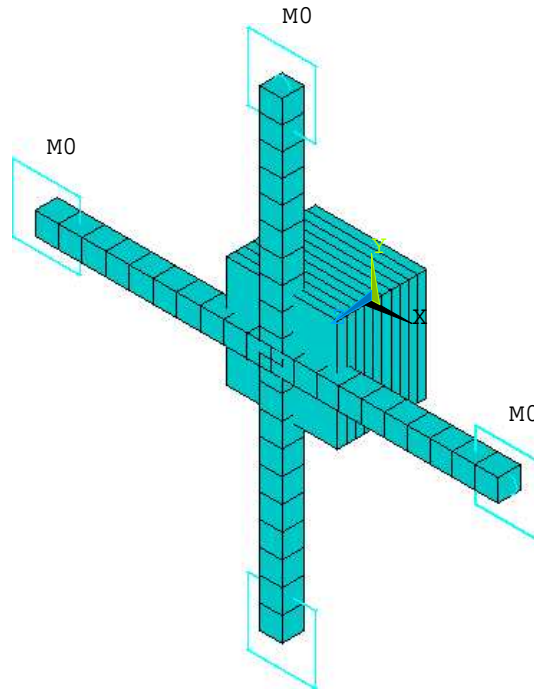
FIG. B.1: ANSYS model of the 4 cantilevered arms with masses on the ends.

The equations for the deflection of cantilevers was obtained from Ref [32]. In the development of the equations of motion, it shall be assumed that:

- the axial deflection along the support shaft is negligible and hence has infinite stiffness,

- the mass (and hence inertia) of each shaft is small compared to the effect of the masses on the ends of the cantilevers,

- the system only has small deflections and hence one can approximate $\sin\theta = \theta$

- ignore the drilling motion of the masses,

- base of support shaft is clamped to provide force and moment restraints.

The deflections due to force F_1 applied at mass m_1 are given by

$$\theta_{11} = \frac{(F_1 L_1)L_3}{E_3 I_3} \tag{B.1}$$

$$d_{11} = \frac{F_1 L_1^3}{3E_1 I_1} + L_1 \left[\frac{(F_1 L_1)L_3}{E_3 I_3} \right] \tag{B.2}$$

$$\theta_{21} = \frac{(F_1 L_1)L_3}{E_3 I_3} \tag{B.3}$$

$$d_{21} = -L_2 \left[\frac{(F_1 L_1)L_3}{E_3 I_3} \right] \tag{B.4}$$

The deflections due to force F_2 applied at mass m_2 are given by

$$\theta_{22} = -\frac{(F_2 L_2)L_3}{E_3 I_3} \tag{B.5}$$

$$d_{22} = \frac{F_2 L_2^3}{3E_2 I_2} + L_2 \left[\frac{(F_2 L_2)L_3}{E_3 I_3} \right] \tag{B.6}$$

$$\theta_{12} = -\frac{(F_2 L_2)L_3}{E_3 I_3} \tag{B.7}$$

$$d_{12} = -L_1 \left[\frac{(F_2 L_2)L_3}{E_3 I_3} \right] \tag{B.8}$$

Using Eqs. (B.1) to (B.8) the matrix of influence coefficients can be formed as

$$\mathbf{D} = \begin{bmatrix} d_{11} & d_{12} \\ d_{21} & d_{22} \end{bmatrix} \tag{B.9}$$

The stiffness matrix is the inverse of the matrix of influence coefficients given by

$$\mathbf{K} = (\mathbf{D})^{-1} \tag{B.10}$$

The mass matrix contains the masses of the cantilevers along the diagonal entries of the matrix.

$$\mathbf{M} = \begin{bmatrix} m_1 & 0 \\ 0 & m_2 \end{bmatrix} \tag{B.11}$$

B.1 Verification

This section contains an example problem using the theory described in the previous section. A theoretical model implemented in Matlab is compared with an ANSYS FEA model to ensure that identical results are obtained from the two methods.

The first part of this section considers the cantilever vibration damper under static loads and the displacements at the ends of the arms are calculated using a Matlab implementation and a FE model.

Table B.1 contains the parameters used in the verification of the cantilever tuned vibration damper.

Table B.1: Values of the parameters used in the verification of the equations of motion of the cantilever vibration damper.

Parameter	Value	Units
Cantilever Arms		
arm3 len	0.053	m
arm thick	0.005	m
arm area	2.50E-05	m^2
arm I	5.21E-11	m^4
arm dens	100	$\mathrm{kg/m}^3$
arm mass	0.01	kg
arm E	7.00E+10	Pa
Upright Arm		
upr E	1.30E+11	Pa
upr thick	0.025	m
upr area	6.25E-04	m^2
upr I	3.26E-08	m^4
upr dens	100	$\mathrm{kg/m}^3$
arm height	0.02	m

Figure B.2 shows the finite element model of the cantilever tuned vibration damper.

The following sub-sections show the results of the static analyses.

ANSYS 7.0SP11
PLOT NO.   1

M0

Y

X

M0

-.607E-04   -.472E-04   -.337E-04   -.202E-04   -.673E-05
        -.539E-04   -.405E-04   -.270E-04   -.135E-04   .100E-07
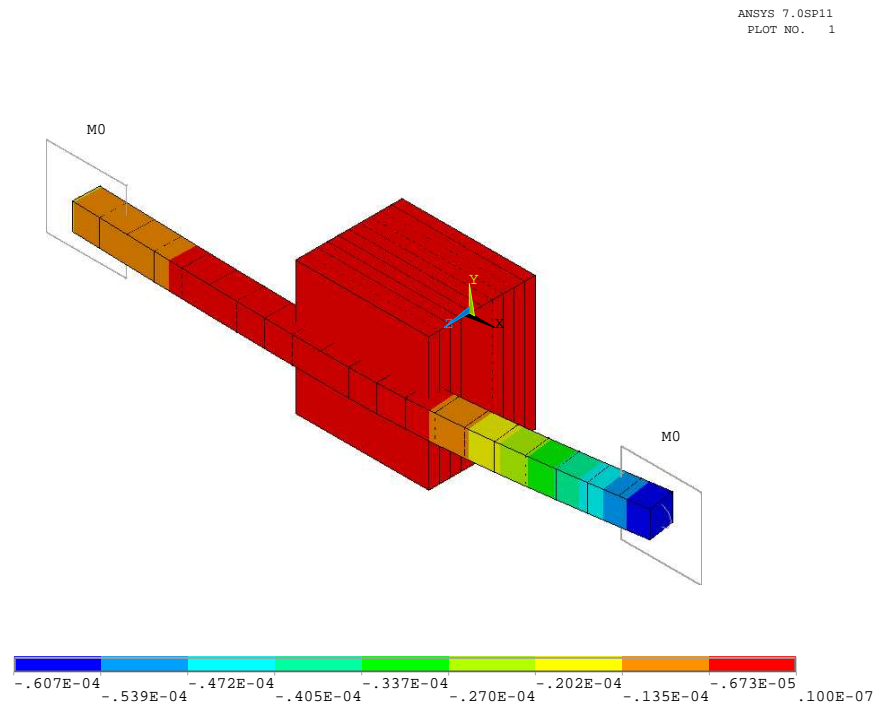
FIG. B.2: ANSYS model of 2 cantilevered arms with masses on the ends with forces applied at both ends.

B.1.1   Single Load

A single load was applied to the cantilevered tuned vibration damper of $F_1 = 1$N. Table B.2 lists the results of the theoretical and FE models and are identical, which provides confirmation that theoretical model is accurate.

Table B.2: Comparison of theory implemented in Matlab and the ANSYS results for single load on the cantilevered tuned mass damper.

Location	Matlab	ANSYS results
Y1	1.3625E-05	1.3625E-05

B.1.2 Double Load

Two static loads were applied to the cantilever tuned vibration damper of $F_1 = 1$N and $F_2 = 5$N. Figure B.2 shows the ANSYS results of the displacement of the two masses due to the applied forces. Table B.3 lists the results of the theoretical and FE models and are identical, which provides confirmation that theoretical model is accurate.

Table B.3: Comparison of theory implemented in Matlab and the ANSYS results for two loads on the cantilevered tuned mass damper.

Location	Matlab	ANSYS results
Y1	1.3561E-05	1.3562E-05
Y2	6.0689E-05	6.0691E-05

B.1.3 Resonance Frequencies

The resonance frequencies of the tuned vibration damper were calculated using the theoretical model and the FE model. Table B.4 shows that the resonance frequencies are within 0.2% of each other, which indicates that the theoretical model is accurate.

Table B.4: Comparison of theory implemented in Matlab and the ANSYS results for resonance frequencies the cantilevered tuned mass damper.

Mode No.	Matlab	ANSYS
1	431.17 Hz	430.42 Hz
2	456.78 Hz	456.01 Hz

The formula for the lowest resonance frequency of mass suspended at the end of a clamped-free beam is [33, p715]

$$f = \frac{1}{2\pi} \sqrt{\frac{3EI}{Ml^3 + 0.236\rho Al^4}} \tag{B.12}$$

where E and I are the Young's modulus and moment of inertia of the beam, respectively,

M is the mass at the end of the beam, ρ is the density of the beam, and l is the length of the cantilever.

As an example problem, physical parameters will be assigned to the dimensions of the cantilever arms as listed in Table B.5.

Table B.5: Physical properties of the arms

Parameter	Value
Arm 1 length	0.054 m
Arm 2 length	0.053 m
Arm 3 length	0.052 m
Arm 4 length	0.051 m
Mass on end of arms	0.01 kg
Young's modulus of arm	70 GPa
Thickness of arm	t = 5 mm
Cross sectional area	t^2 m^2
Moment of inertia	$t^4/12$ m^4
Density of arms	100 kg/m^3

The resonance frequencies of four cantilevers was calculated using ANSYS and theory from Eq. (B.12). In the ANSYS model, the hub at the centre of the four arms had boundary conditions applied to provide a fully clamped constraint. Table B.6 lists the comparison and shows that ANSYS correctly predicts the resonance frequencies within 0.2%.

Table B.6: Comparison of resonance frequencies predicted using ANSYS and theoretical values.

Arm No.	ANSYS (Hz)	Theory (Hz)
1	418.8	419.5
2	430.7	431.4
3	443.2	443.9
4	456.3	457.0

B.2   Verification of Rotational Mode Shapes

The analyses of the application of moment loading to the structure requires the rotational mode shape data. The structural mode shapes are calculated using ANSYS and while it is easy to verify that the translational mode shapes are accurate of a real system, it is not obvious whether the results for the mode shapes of the rotational degrees of freedom are representative of a real system.

This appendix shows the comparison of the calculated rotational mode shapes and compares them with an estimated rotational mode shape that is calculated using the translational mode shape data. It is shown that the two sets of results give similar results, and hence the calculated rotational mode shape data is correct.

It is important to ensure that the rotational displacements calculated by ANSYS are in fact representative of the distorted angular mode shape.

The longbox model was analysed to extract the mode shapes and natural frequencies. Fortunately in the results for the mode shapes the rotational degrees of freedom are included. Figure B.3 shows the ANSYS model mode shape for the 2,1 mode at 197Hz.
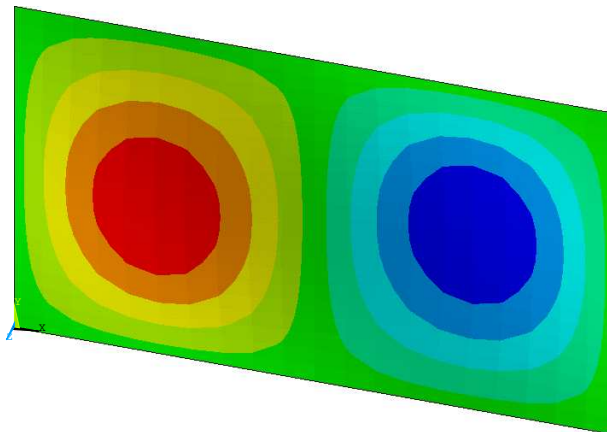
FIG. B.3: ANSYS model of a simply supported plate showing the 2,1 vibration mode.

Figure B.4 shows the out of plane displacement of the nodes along the line $y = 0.15$m. The abscissa (x-axis) is the distance from the origin along the x-axis of the plate. The

ordinate (y-axis) is the displacement of the node normalised to the mass matrix. The graph indicates that the displacement of the plate resembles a sine wave and hence is vibrating in the 2 mode in this direction.

Figure B.5 shows the results from the ANSYS modal analysis which shows the calculated rotational displacement of each node and an estimated rotational displacement. The estimated rotational displacement was calculated by evaluating the slope $(\partial z / \partial x)$ using the out-of-plane displacement of the two nearest nodes and the spacing between these two nodes. The spacing between two adjacent nodes is 0.025m. The results in Figure B.5 show that the calculated ANSYS rotational displacement is accurate.

FIG. B.4: Results from ANSYS mode shapes showing the out-of-plane displacement at $y = 0.15$m.

FIG. B.5: Results from ANSYS mode shapes showing the actual rotational displacement for the mode and the estimated rotational displacement calculated from the out-of-plane displacement from the two nearest nodes.
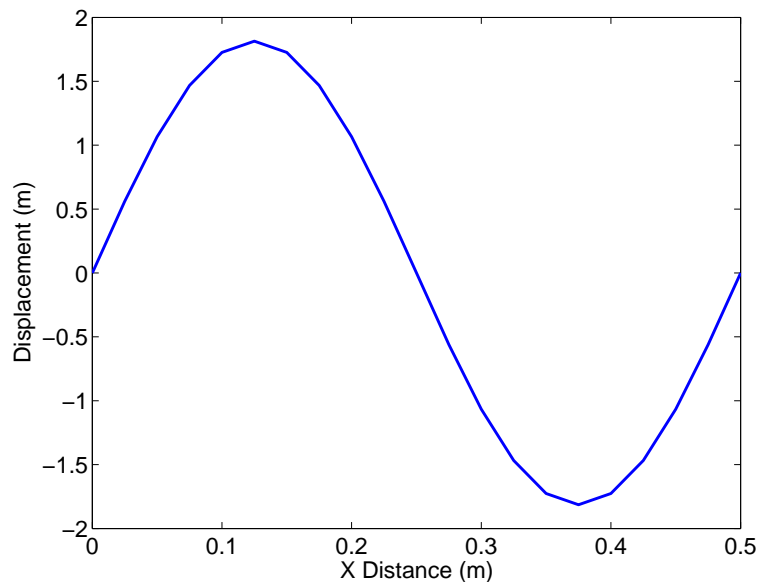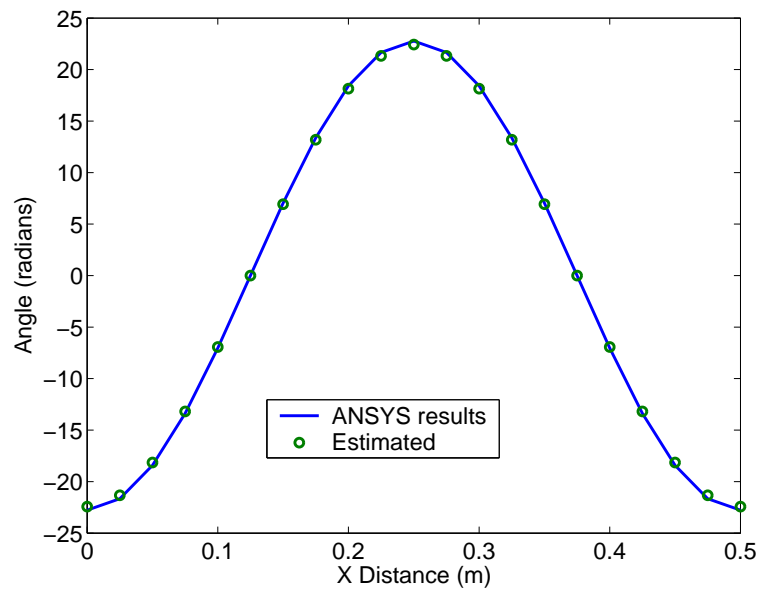
B.3   Verification of Moment Loading

A model of a simply supported plate was used to demonstrate that the response of moments applied to the plate could be calculated correctly using a modal model. The model that was investigated was the plate from the vibro-acoustic system shown in Figure 1.6. A Matlab model and the ANSYS model were compared.

Figure B.6 shows the comparison between the ANSYS and Matlab models of the out-of-plane displacement (U_z) of the plate when a vertical force of $F_z = 1$N was applied at $(0.1, 0.075)$. The results show that the Matlab model calculates the same displacement as predicted by the ANSYS model.
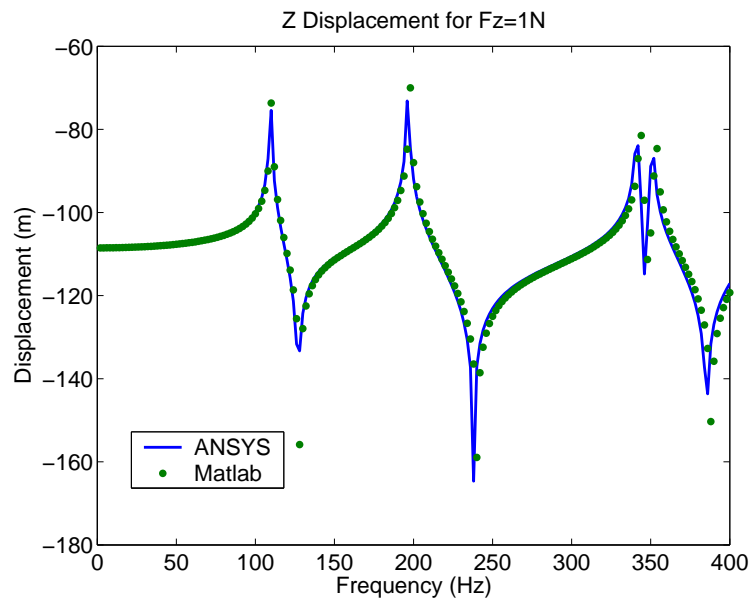
FIG. B.6: Displacement of the plate for a force $F_z = 1$N.

Figures B.7 and B.8 show the comparison between the ANSYS and Matlab models for the out-of-plane displacement (U_z) of the plate when moments $M_x = 0.1$Nm and $M_y = 0.1$Nm were applied to the plate, respectively. The results show that the Matlab model calculates the same displacement as predicted by the ANSYS model.

The previous results showed that the displacement at a single point on the plate could be predicted accurately. The next step in the verification process was to ensure that the overall structural kinetic energy for both methods are the same. Figures B.9 and B.10 show the total structural kinetic energy of the plate due to moment loadings of
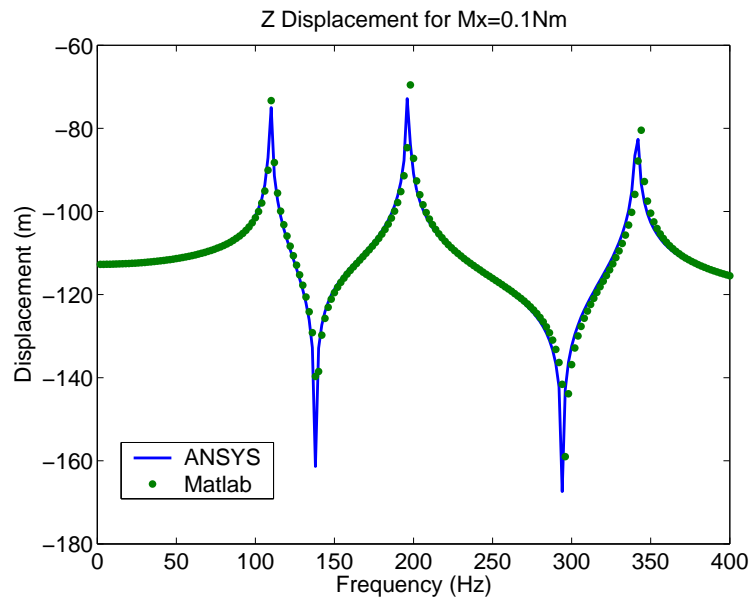
FIG. B.7: Displacement of the plate for a moment of $M_x = 0.1$Nm.
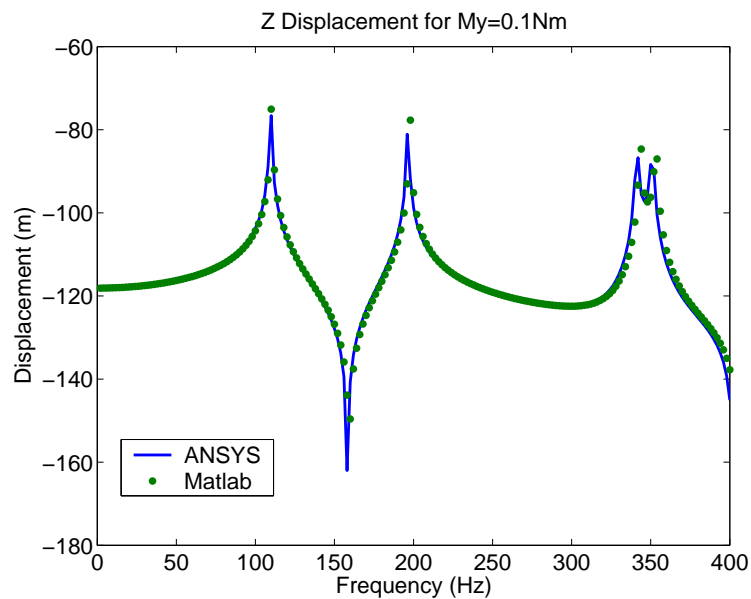
FIG. B.8: Displacement of the plate for a moment of $M_y = 0.1$Nm.

$M_x = 0.1$Nm and $M_y = 0.1$Nm, respectively. These results show that the Matlab modal coupling model predicts the same results as the ANSYS model.

The conclusion from this analysis is that the method of applying the moment loading to the plate is correct.
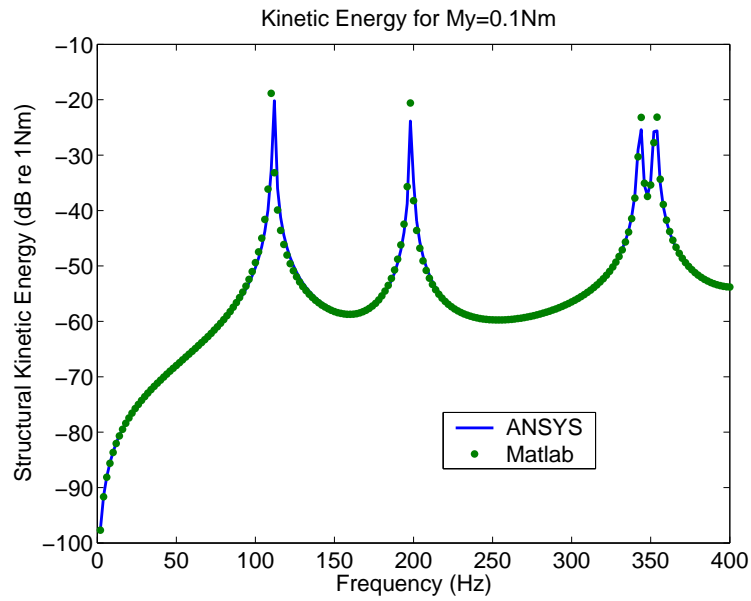
FIG. B.9: Kinetic energy of the plate for a moment of $M_x = 0.1\text{Nm}$.
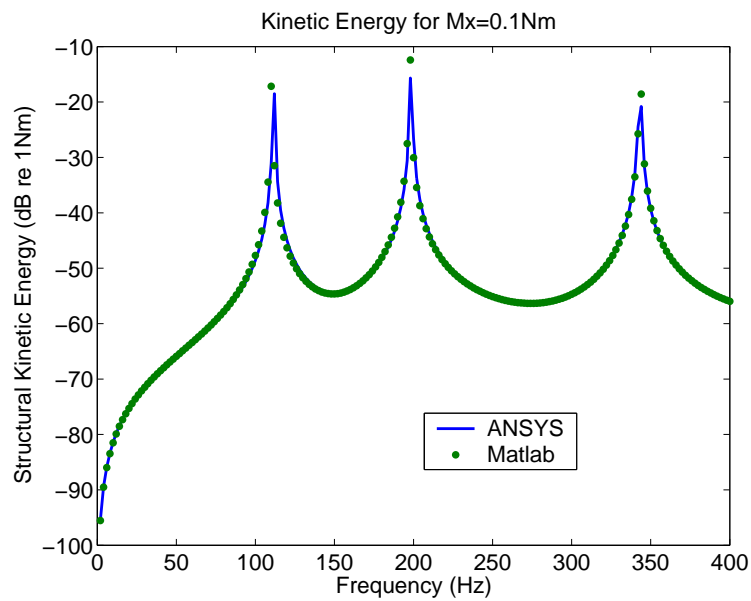
FIG. B.10: Kinetic energy of the plate for a moment of $M_y = 0.1\text{Nm}$.
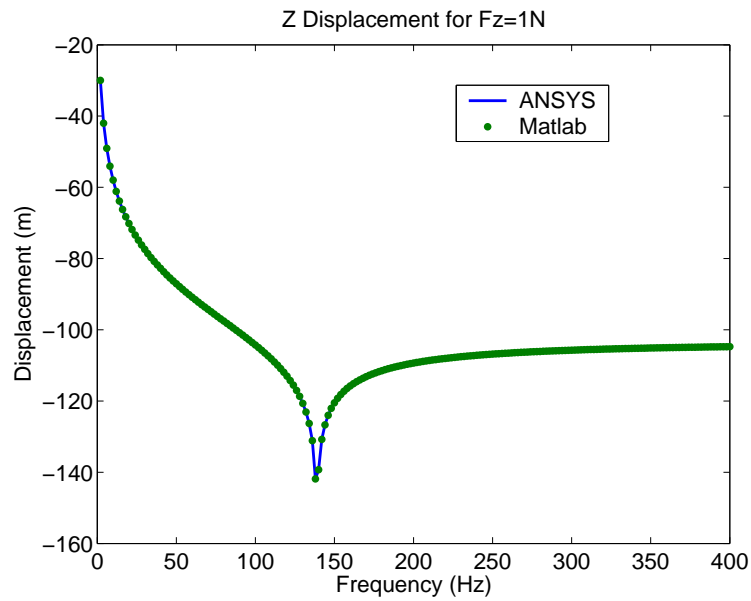
FIG. B.11: Verification using the large 5×5 matrix for $F_z = 1$N, displacement along U_z at the base.
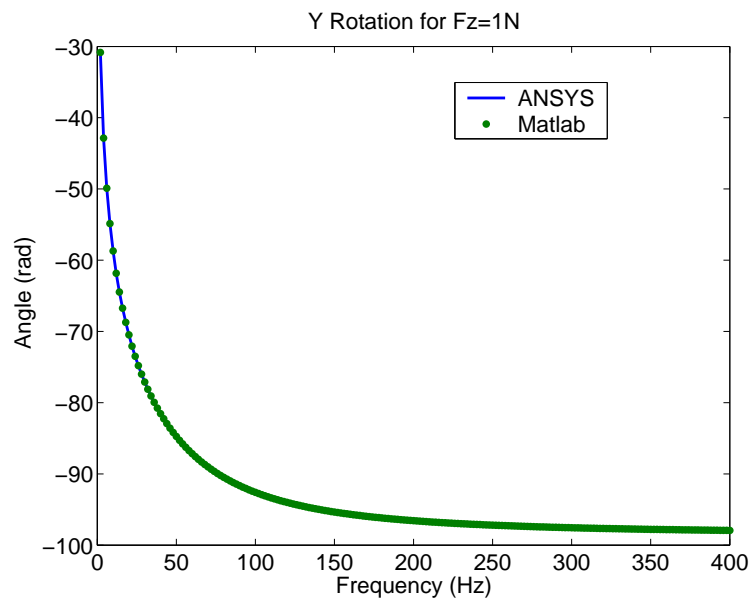
FIG. B.12: Verification using the large 5×5 matrix for $F_z = 1$N, displacement along θ_y at the base.
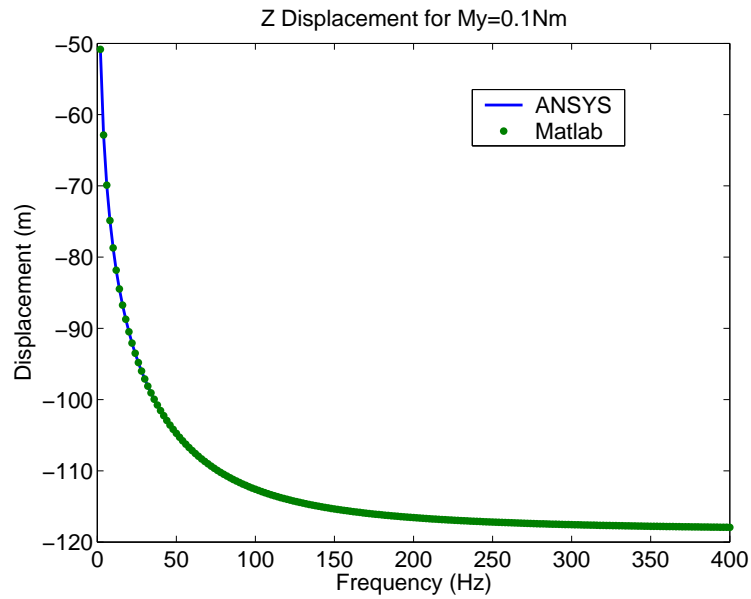
FIG. B.13: Verification using the large 5×5 matrix for $M_y = 0.1$Nm, displacement along U_z at the base.
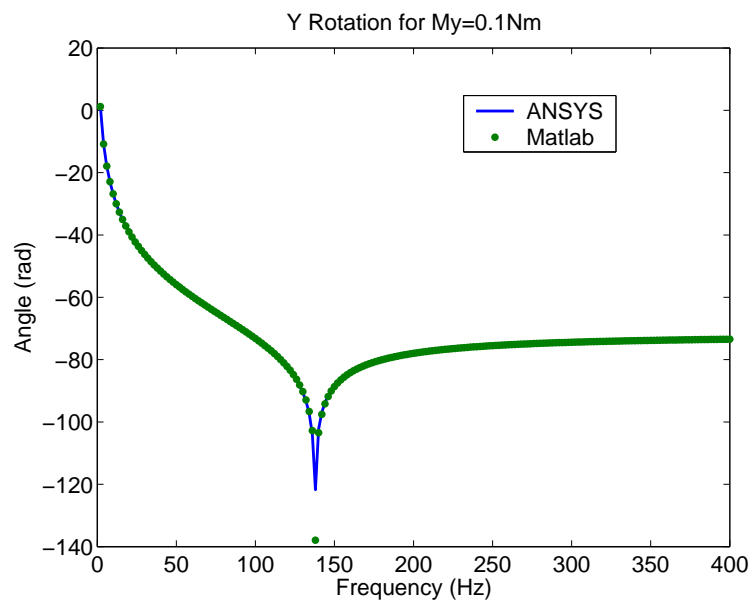
FIG. B.14: Verification using the large 5×5 matrix for $M_y = 0.1$Nm, displacement along θ_y at the base.

B.4   Transformation of Rotational Mode Shapes

The rotational mode shapes that are calculated in ANSYS are described in the global Cartesian coordinate system. The structural model that is under investigation here is the composite Representative Scale Launch Vehicle Fairing, which is similar in shape to a cylinder.

In order to apply the moment loading onto the fairing, it is convenient to transform the mode shapes from the Cartesian coordinate system into an (almost) cylindrical coordinate system. By doing so, the moment loads can be resolved into two orthogonal rotational axes. The third rotational axis, which is the drilling moment into the faring, is redundant.

The Cartesian coordinate system is rotated such that the x-axis is always pointing outwards along the normal to the surface of the structure. The z-axis always points to the top of the fairing and is tangent to the surface of the structure and the normal vector.

Figure B.15 shows the rotation of the XY and XZ axes through angles θ and ϕ, respectively.
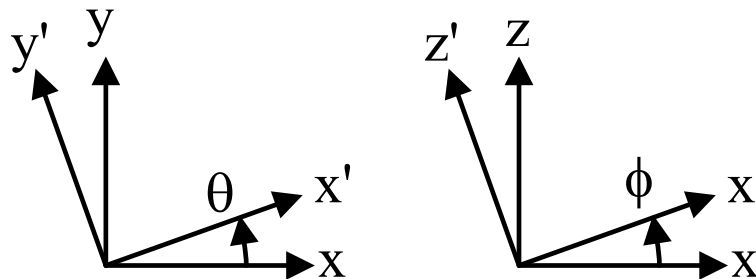
FIG. B.15: Rotated coordinate systems in the XY and XZ planes.

The transformed coordinates in the XY plane are given [25, p222]:

$$\begin{bmatrix} x' \\ y' \\ z' \end{bmatrix} = \begin{bmatrix} \cos\theta & \sin\theta & 0 \\ -\sin\theta & \cos\theta & 0 \\ 0 & 0 & 1 \end{bmatrix} \begin{bmatrix} x \\ y \\ z \end{bmatrix} \tag{B.13}$$

The transformed coordinates in the XZ plane are given :

$$
\begin{bmatrix} x' \\ y' \\ z' \end{bmatrix} = \begin{bmatrix} \cos\phi & 0 & \sin\phi \\ 0 & 1 & 0 \\ -\sin\phi & 0 & \cos\phi \end{bmatrix} \begin{bmatrix} x \\ y \\ z \end{bmatrix} \tag{B.14}
$$

where the rotation angles θ and ϕ are calculated using the vector normal to the surface of the structure.

The transformation of the rotational mode shapes from the Cartesian coordinate system to the pseudo-cylindrical coordinate system is achieved by using Eqs. (B.13) and (B.14).

For example, we shall examine the response of the third structural mode of the fairing at the node locations where $x = 0$m, $y = 0.776$m, between $1 < z < 3$m, which roughly corresponds to the outer edge of the fairing along the y axis, as shown in Figure B.16.
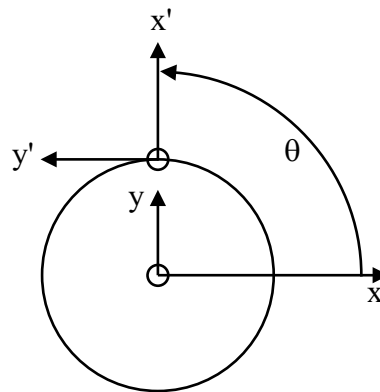
FIG. B.16: Rotated coordinate system for the RSLVF.

Figure B.17 shows three mode shapes with the abscissa corresponding to the modal amplitude and the ordinate corresponding to the height (z coordinate) along the fairing. The translational mode shape along the radial axis is shown by the dot points on the far left of the graph, which reach a peak displacement at approximately $z = 2.4$m. The rotational mode shape along the θ_x axis corresponds to the derivative of the radial mode shape and the results calculated using ANSYS are shown in Figure B.17 as circles. It can be seen that when the modal amplitude equals zero at $z = 2.4$m, this point corresponds
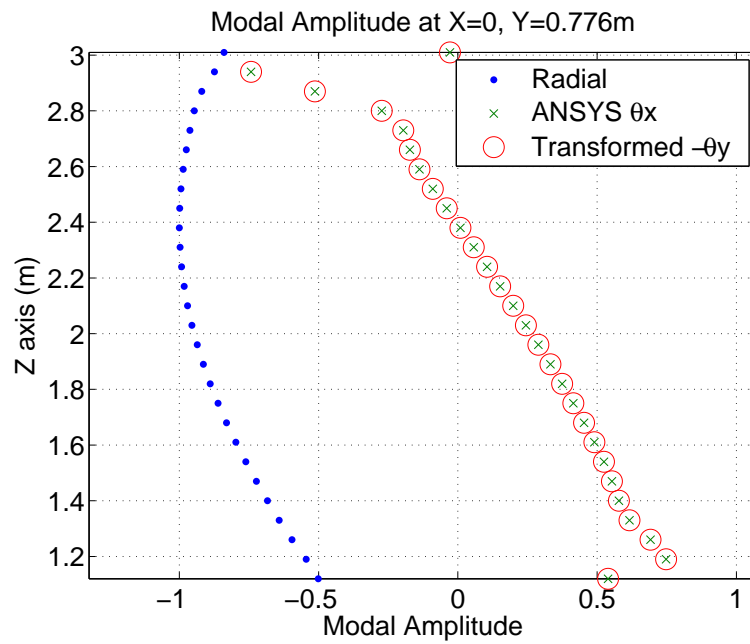
FIG. B.17: Rotated mode shapes showing the radial mode, the θ_x mode shape from ANSYS, and the negated transformed mode shape along θ'_y.

to the maximum radial displacement.

This mode shape was transformed using Eqs. (B.13) and (B.14) and the transformed axes are shown in Figure B.16, with the x' axis pointed radially outwards from the surface of the fairing and the y' axis pointed tangential to the surface. The mode shape was transformed and the negative amplitude of the θ'_y is plotted in Figure B.17 to show that the points coincide with the θ_x results calculated in ANSYS.

B.5 Derivation of Equations of Motion for Cantilevered Vibration Damper

The following pages contain the algebraic derivation of the equations of motion for the cantilevered vibration damper.

Carl Howard   Cantilever Eqs of Motion

The equations of motion for the cantilever can be written in matrix form as

$$
\begin{bmatrix}
k_1 - \omega^2 \cdot m_1 & 0 & -k_1 & -L_1 \cdot k_1 & 0 \\[4pt]
0 & k_2 - \omega^2 \cdot m_2 & -k_2 & L_2 \cdot k_2 & 0 \\[4pt]
-k_1 & -k_2 & k_1 + k_2 & L_1 \cdot k_1 - L_2 \cdot k_2 & 0 \\[4pt]
-L_1 \cdot k_1 & L_2 \cdot k_2 & \begin{array}{c} L_1 \cdot k_1 \dots \\ +-L_2 \cdot k_2 \end{array} & \begin{array}{c} L_1^2 \cdot k_1 \dots \\ +L_2^2 \cdot k_2 \dots \\ +-k_{3\theta} \end{array} & k_{3\theta} \\[14pt]
0 & 0 & 0 & k_{3\theta} & \begin{array}{c} -k_{3\theta} \dots \\ +-L_3^2 \cdot (m_1 + m_2) \cdot \omega^2 \end{array}
\end{bmatrix}
\cdot
\begin{bmatrix} x_1 \\ x_2 \\ x_3 \\ \theta_B \\ \theta_3 \end{bmatrix}
=
\begin{bmatrix} F_1 \\ F_2 \\ F_3 \\ 0 \\ M_3 \end{bmatrix}
$$

$$
\begin{bmatrix}
x_1 \cdot k_1 - x_1 \cdot \omega^2 \cdot m_1 - k_1 \cdot x_3 - L_1 \cdot k_1 \cdot \theta_B \\[4pt]
x_2 \cdot k_2 - x_2 \cdot \omega^2 \cdot m_2 - k_2 \cdot x_3 + L_2 \cdot k_2 \cdot \theta_B \\[4pt]
-x_1 \cdot k_1 - x_2 \cdot k_2 + k_1 \cdot x_3 + k_2 \cdot x_3 + L_1 \cdot k_1 \cdot \theta_B - L_2 \cdot k_2 \cdot \theta_B \\[4pt]
\begin{array}{c} -L_1 \cdot k_1 \cdot x_1 + L_2 \cdot k_2 \cdot x_2 + x_3 \cdot L_1 \cdot k_1 - x_3 \cdot L_2 \cdot k_2 \dots \\ + \theta_B \cdot L_1^2 \cdot k_1 + \theta_B \cdot L_2^2 \cdot k_2 - \theta_B \cdot k_{3\theta} + k_{3\theta} \cdot \theta_3 \end{array} \\[14pt]
\theta_B \cdot k_{3\theta} - k_{3\theta} \cdot \theta_3 - \theta_3 \cdot L_3^2 \cdot \omega^2 \cdot m_1 - \theta_3 \cdot L_3^2 \cdot \omega^2 \cdot m_2
\end{bmatrix}
=
\begin{bmatrix} F_1 \\ F_2 \\ F_3 \\ 0 \\ M_3 \end{bmatrix}
$$

Take the 4th line and solve for θ_B

$$
0 = -L_1 \cdot k_1 \cdot x_1 + L_2 \cdot k_2 \cdot x_2 + x_3 \cdot L_1 \cdot k_1 - x_3 \cdot L_2 \cdot k_2 \dots \\
+ \theta_B \cdot L_1^2 \cdot k_1 + \theta_B \cdot L_2^2 \cdot k_2 - \theta_B \cdot k_{3\theta} + k_{3\theta} \cdot \theta_3
$$

$$
\theta_B = \frac{\left(L_1 \cdot k_1 \cdot x_1 - L_2 \cdot k_2 \cdot x_2 - x_3 \cdot L_1 \cdot k_1 + x_3 \cdot L_2 \cdot k_2 - k_{3\theta} \cdot \theta_3 \right)}{\left(L_1^2 \cdot k_1 + L_2^2 \cdot k_2 - k_{3\theta} \right)}
$$

1

Contract Number : F62562-03-C-0029   July 2004

Carl Howard   Cantilever Eqs of Motion

Now work on the 1st line $F_1 = x_1 \cdot k_1 - x_1 \cdot \omega^2 \cdot m_1 - k_1 \cdot x_3 - L_1 \cdot k_1 \cdot \theta_B$

Substitute θ_B into the 1st line and replace $x_3 = \psi_J \cdot w_p$ $\theta_3 = \psi_{J\theta} \cdot w_p$

$$F_1 = \left[k_1 - \omega^2 \cdot m_1 - L_1^2 \cdot \frac{k_1^2}{\left(L_1^2 \cdot k_1 + L_2^2 \cdot k_2 - k_{3\theta} \right)} \right] \cdot x_1 \ldots$$

$$+ L_1 \cdot k_1 \cdot L_2 \cdot \frac{k_2}{\left(L_1^2 \cdot k_1 + L_2^2 \cdot k_2 - k_{3\theta} \right)} \cdot x_2 \ldots$$

$$+ -k_1 \cdot \left(\psi_J \cdot L_2^2 \cdot k_2 - \psi_J \cdot k_{3\theta} + L_1 \cdot \psi_J \cdot L_2 \cdot k_2 - L_1 \cdot k_{3\theta} \cdot \psi_{J\theta} \right) \cdot \frac{w_p}{\left(L_1^2 \cdot k_1 + L_2^2 \cdot k_2 - k_{3\theta} \right)}$$

Now work on the 2nd line $F_2 = x_2 \cdot k_2 - x_2 \cdot \omega^2 \cdot m_2 - k_2 \cdot x_3 + L_2 \cdot k_2 \cdot \theta_B$

Substitute θ_B into the 2nd line and replace $x_3 = \psi_J \cdot w_p$ $\theta_3 = \psi_{J\theta} \cdot w_p$

$$F_2 = \left[k_2 - \omega^2 \cdot m_2 - L_2^2 \cdot \frac{k_2^2}{\left(L_1^2 \cdot k_1 + L_2^2 \cdot k_2 - k_{3\theta} \right)} \right] \cdot x_2 \ldots$$

$$+ -k_2 \cdot \left(\psi_J \cdot L_1^2 \cdot k_1 - \psi_J \cdot k_{3\theta} + L_2 \cdot \psi_J \cdot L_1 \cdot k_1 + L_2 \cdot k_{3\theta} \cdot \psi_{J\theta} \right) \cdot \frac{w_p}{\left(L_1^2 \cdot k_1 + L_2^2 \cdot k_2 - k_{3\theta} \right)} \ldots$$

$$+ L_2 \cdot k_2 \cdot L_1 \cdot k_1 \cdot \frac{x_1}{\left(L_1^2 \cdot k_1 + L_2^2 \cdot k_2 - k_{3\theta} \right)}$$

2

Carl Howard   Cantilever Eqs of Motion

Substitute θ_B into the 5th line and replace $x_3 = \psi_J \cdot w_p$ $\theta_3 = \psi_{J\theta} \cdot w_p$

$$M_3 = \theta_B \cdot k_{3\theta} - k_{3\theta} \cdot \theta_3 - \theta_3 \cdot L_3{}^2 \cdot \omega^2 \cdot m_1 - \theta_3 \cdot L_3{}^2 \cdot \omega^2 \cdot m_2$$

$$M_3 = -L_2 \cdot \frac{k_2}{\left(L_1{}^2 \cdot k_1 + L_2{}^2 \cdot k_2 - k_{3\theta}\right)} \cdot k_{3\theta} \cdot x_2 \,\cdots$$
$$+ -\psi_{J\theta} \cdot L_3{}^2 \cdot \left(m_1 + m_2\right) \cdot w_p \cdot \omega^2 + 0 \,\cdots$$
$$+ 0 + \left[\frac{\left(-\psi_J \cdot L_1 \cdot k_1 + \psi_J \cdot L_2 \cdot k_2 - k_{3\theta} \cdot \psi_{J\theta}\right)}{\left(L_1{}^2 \cdot k_1 + L_2{}^2 \cdot k_2 - k_{3\theta}\right)} \cdot k_{3\theta} - k_{3\theta} \cdot \psi_{J\theta}\right] \cdot w_p \,\cdots$$
$$+ 0 + L_1 \cdot k_1 \cdot \frac{x_1}{\left(L_1{}^2 \cdot k_1 + L_2{}^2 \cdot k_2 - k_{3\theta}\right)} \cdot k_{3\theta}$$

Substitute θ_B into the 3rd line and replace $x_3 = \psi_J \cdot w_p$ $\theta_3 = \psi_{J\theta} \cdot w_p$

$$F_3 = -k_1 \cdot \frac{\left(L_2{}^2 \cdot k_2 - k_{3\theta} + L_2 \cdot k_2 \cdot L_1\right)}{\left(L_1{}^2 \cdot k_1 + L_2{}^2 \cdot k_2 - k_{3\theta}\right)} \cdot x_1 \,\cdots$$
$$+ -k_2 \cdot \frac{\left(L_1{}^2 \cdot k_1 - k_{3\theta} + L_1 \cdot k_1 \cdot L_2\right)}{\left(L_1{}^2 \cdot k_1 + L_2{}^2 \cdot k_2 - k_{3\theta}\right)} \cdot x_2 \,\cdots$$
$$+ \frac{\left[\begin{array}{l} k_2 \cdot \psi_J \cdot L_1{}^2 \cdot k_1 - k_2 \cdot \psi_J \cdot k_{3\theta} \,\cdots \\ + 2 \cdot L_1 \cdot k_1 \cdot \psi_J \cdot L_2 \cdot k_2 - L_1 \cdot k_1 \cdot k_{3\theta} \cdot \psi_{J\theta} \,\cdots \\ + k_1 \cdot \psi_J \cdot L_2{}^2 \cdot k_2 - k_1 \cdot \psi_J \cdot k_{3\theta} + L_2 \cdot k_2 \cdot k_{3\theta} \cdot \psi_{J\theta} \end{array}\right]}{\left(L_1{}^2 \cdot k_1 + L_2{}^2 \cdot k_2 - k_{3\theta}\right)} \cdot w_p$$

3

Carl Howard   Cantilever Eqs of Motion

Multiply the 3rd line by ψ_{JT}
Multiply the 5th line by $\psi_{J\theta T}$

then add them together $\psi_{JT} \cdot F_3 + \psi_{J\theta T} \cdot M_3$

$\psi_{JT} \cdot F_3 + \psi_{J\theta T} \cdot M_3 = \blacksquare$

$$k_1 \cdot \frac{\left(-\psi_{JT} \cdot L_2{}^2 \cdot k_2 + \psi_{JT} \cdot k_{3\theta} - \psi_{JT} \cdot L_2 \cdot k_2 \cdot L_1 + \psi_{J\theta T} \cdot L_1 \cdot k_{3\theta}\right)}{\left(k_1 \cdot L_1{}^2 - k_{3\theta} + L_2{}^2 \cdot k_2\right)} \cdot x_1 \cdots$$

$$+ -k_2 \cdot \frac{\left(\psi_{JT} \cdot k_1 \cdot L_1{}^2 - \psi_{JT} \cdot k_{3\theta} + \psi_{JT} \cdot L_1 \cdot k_1 \cdot L_2 + \psi_{J\theta T} \cdot L_2 \cdot k_{3\theta}\right)}{\left(k_1 \cdot L_1{}^2 - k_{3\theta} + L_2{}^2 \cdot k_2\right)} \cdot x_2 \cdots$$

$$+ \left[\begin{array}{l} \left[\begin{array}{l} \psi_{JT} \cdot \left(L_2 \cdot k_2 \cdot k_{3\theta} - L_1 \cdot k_1 \cdot k_{3\theta}\right) \cdot \psi_{J\theta} \cdots \\ + 0 + \psi_{JT} \cdot \left[\begin{array}{l} k_2 \cdot L_1{}^2 \cdot k_1 - k_2 \cdot k_{3\theta} \cdots \\ + k_1 \cdot L_2{}^2 \cdot k_2 - k_1 \cdot k_{3\theta} \cdots \\ + 2 \cdot L_1 \cdot k_1 \cdot L_2 \cdot k_2 \end{array} \right] \cdot \psi_J \end{array} \right] \cdots \\ + \left[\begin{array}{l} \left[\begin{array}{l} -k_{3\theta} \cdot k_1 \cdot L_1{}^2 - k_{3\theta} \cdot L_2{}^2 \cdot k_2 \cdots \\ + -\omega^2 \cdot L_3{}^2 \cdot \left(m_2 + m_1\right) \cdot \left[\begin{array}{l} L_2{}^2 \cdot k_2 \cdots \\ + L_1{}^2 \cdot k_1 \cdots \\ + -k_{3\theta} \end{array} \right] \\ + k_{3\theta} \cdot \psi_J \cdot L_2 \cdot k_2 - k_{3\theta} \cdot L_1 \cdot k_1 \cdot \psi_J \end{array} \right] \cdot \psi_{J\theta} \cdots \right] \cdot \psi_{J\theta T} \end{array} \right] \cdot \frac{w_p}{\left(k_1 \cdot L_1{}^2 - k_{3\theta} + L_2{}^2 \cdot k_2\right)}$$

4

Carl Howard   Cantilever Eqs of Motion

Put all the results into a matrix
$$\begin{bmatrix} A_{11} & A_{12} & A_{13} \\ A_{21} & A_{22} & A_{23} \\ A_{31} & A_{32} & A_{33} \end{bmatrix} \cdot \begin{bmatrix} x_1 \\ x_2 \\ w_p \end{bmatrix}$$

$$A_{11} = \left[k_1 - \omega^2 \cdot m_1 - L_1^2 \cdot \frac{k_1^2}{\left(L_1^2 \cdot k_1 + L_2^2 \cdot k_2 - k_{3\theta} \right)} \right]$$

$$A_{12} = L_1 \cdot k_1 \cdot L_2 \cdot \frac{k_2}{\left(L_1^2 \cdot k_1 + L_2^2 \cdot k_2 - k_{3\theta} \right)}$$

$$A_{13} = -k_1 \cdot \frac{\left(\psi_J \cdot L_2^2 \cdot k_2 - k_{3\theta} \cdot \psi_J + L_1 \cdot \psi_J \cdot L_2 \cdot k_2 - k_{3\theta} \cdot L_1 \cdot \psi_{J\theta} \right)}{\left(L_2^2 \cdot k_2 + L_1^2 \cdot k_1 - k_{3\theta} \right)}$$

$$A_{21} = L_1 \cdot k_1 \cdot L_2 \cdot \frac{k_2}{\left(L_2^2 \cdot k_2 + L_1^2 \cdot k_1 - k_{3\theta} \right)}$$

$$A_{22} = \left[k_2 - \omega^2 \cdot m_2 - L_2^2 \cdot \frac{k_2^2}{\left(L_1^2 \cdot k_1 + L_2^2 \cdot k_2 - k_{3\theta} \right)} \right]$$

$$A_{23} = -k_2 \cdot \frac{\left(\psi_J \cdot L_1^2 \cdot k_1 - k_{3\theta} \cdot \psi_J + L_1 \cdot \psi_J \cdot L_2 \cdot k_1 + L_2 \cdot k_{3\theta} \cdot \psi_{J\theta} \right)}{\left(L_2^2 \cdot k_2 + L_1^2 \cdot k_1 - k_{3\theta} \right)}$$

5

Carl Howard   Cantilever Eqs of Motion

$$A_{31} = k_1 \cdot \frac{\left(-\psi_{JT} \cdot L_2^2 \cdot k_2 + \psi_{JT} \cdot k_{3\theta} - \psi_{JT} \cdot L_2 \cdot k_2 \cdot L_1 + \psi_{J\theta T} \cdot L_1 \cdot k_{3\theta}\right)}{\left(k_1 \cdot L_1^2 - k_{3\theta} + L_2^2 \cdot k_2\right)}$$

$$A_{32} = -k_2 \cdot \frac{\left(\psi_{JT} \cdot k_1 \cdot L_1^2 - \psi_{JT} \cdot k_{3\theta} + \psi_{JT} \cdot L_1 \cdot k_1 \cdot L_2 + \psi_{J\theta T} \cdot L_2 \cdot k_{3\theta}\right)}{\left(k_1 \cdot L_1^2 - k_{3\theta} + L_2^2 \cdot k_2\right)}$$

$$A_{33} = \left[\begin{bmatrix} \psi_{JT} \cdot \left(L_2 \cdot k_2 \cdot k_{3\theta} - L_1 \cdot k_1 \cdot k_{3\theta}\right) \cdot \psi_{J\theta} \cdots \\ + 0 + \psi_{JT} \cdot \begin{bmatrix} k_2 \cdot L_1^2 \cdot k_1 - k_2 \cdot k_{3\theta} \cdots \\ + k_1 \cdot L_2^2 \cdot k_2 - k_1 \cdot k_{3\theta} \cdots \\ + 2 \cdot L_1 \cdot k_1 \cdot L_2 \cdot k_2 \end{bmatrix} \cdot \psi_J \\ + \begin{bmatrix} \begin{bmatrix} -k_{3\theta} \cdot k_1 \cdot L_1^2 - k_{3\theta} \cdot L_2^2 \cdot k_2 \cdots \\ + -\omega^2 \cdot L_3^2 \cdot \left(m_2 + m_1\right) \cdot \begin{bmatrix} L_2^2 \cdot k_2 \cdots \\ + L_1^2 \cdot k_1 \cdots \\ + -k_{3\theta} \end{bmatrix} \end{bmatrix} \cdot \psi_{J\theta} \cdots \\ + k_{3\theta} \cdot \psi_J \cdot L_2 \cdot k_2 - k_{3\theta} \cdot L_1 \cdot k_1 \cdot \psi_J \end{bmatrix} \cdot \psi_{J\theta T} \end{bmatrix} \cdots \right] \cdot \frac{1}{\left(k_1 \cdot L_1^2 - k_{3\theta} + L_2^2 \cdot k_2\right)}$$

6

Bibliography

[1] B. Henderson, C. Gerhart, S. Lane, and E. Jensen. Vibro-acoustic launch protection experiment (VALPE). *Journal of the Acoustical Society of America*, 114(4):2384, 2003.

[2] Carl Olsard, Rick Morgans, Anthony Zander, and Colin Hansen. Investigation of passive control devices for potential application to a launch vehicle structure to reduce the interior noise levels during launch: Final report for Stage 3A. Technical report, Department of Mechanical Engineering, University of Adelaide, Adelaide, S.A. 5005, Australia, September 2003.

[3] Carl Q. Howard, Colin H. Hansen, Rick Morgans, and Anthony C. Zander. Investigation of passive control devices for potential application to a launch vehicle structure to reduce the interior noise levels during launch: Final report for Stage 3B. Technical report, Department of Mechanical Engineering, University of Adelaide, Adelaide, S.A. 5005, Australia, November 2003.

[4] Ben S. Cazzolato. *Sensing systems for active control of sound transmissino into cavities*. PhD thesis, Department of Mechanical Engineering, University of Adelaide, Adelaide, South Australia, Australia, 1999.

[5] Frank J. Fahy. *Sound and Structural Vibration: Radiation, Transmission and Response*. Academic Press, San Diego, California, USA, 1994. ISBN 0122476719.

[6] Carl Q. Howard. *Active isolation of machinery vibration from flexible structures*.

PhD thesis, Department of Mechanical Engineering, University of Adelaide, Adelaide, South Australia, Australia, 1999.

[7] Carl Q. Howard, Colin H. Hansen, and J. Q. Pan. Power transmission from a vibrating body to a circular cylindrical shell through active elastic isolators. *Journal of the Acoustical Society of America*, 101(3):1479–1491, 1997.

[8] Leo L. Beranek and Istvan L. Ver, editors. *Noise and vibration control engineering. Principles and applications.* John Wiley and Sons, U.S.A., 1992.

[9] J. P. Den Hartog. *Mechanical Vibrations.* McGraw-Hill Book Company, Inc., USA, 4th edition, 1956.

[10] F. J. Fahy and C. Schofield. A note on the interaction between a helmholtz resonator and an acoustic mode of an enclosure. *Journal of Sound and Vibration*, 72(3):365–378, 1980.

[11] C.R. Fuller C.R., S.J. Elliot, and P.A. Nelson. *Active Control of Vibration.* Academic Press, 1996.

[12] J.P. Carneal, F. Charette, and C.R. Fuller. Minimization of sound radiation from plates using adaptive tuned vibration absorbers. *Journal of Sound and Vibration*, 270(4-5):781–792, 2004.

[13] Ben S. Cazzolato and Colin H. Hansen. Structural sensing of sound transmission into a cavity for ASAC. In *Proceedings of the 5th International Congress of Sound and Vibration*, pages 2391–2402, 1997.

[14] Colin H. Hansen and Ben S. Cazzolato. Recent advances in the active control of interior noise. In *Proceedings of the 6th International Congress on Sound and Vibration*, pages 85–126, 1999.

[15] M.R. Jolly and J.Q. Sun. Passive tuned vibration absorbers for sound radiation

reduction from vibrating panels. *Journal of Sound and Vibration*, 191(4):466–472, 1996.

[16] Roger Ohayon and Christian Soize. *Structural acoustics and vibration.* Academic Press, San Diego, California, USA, 1998. ISBN 0125249454.

[17] A. D. Pierce, V. W. Sparrow, and D. A. Russell. Fundamental structural-acoustic idealiszations for structures with fuzzy internals. *Journal of Vibration and Acoustics*, 117:339–348, July 1995.

[18] Christian Soize. A model and numerical method in the medium frequency range for vibroacostuic predictions using the theory of structural fuzzy. *Journal of the Acoustical Society of America*, 94(2):849–865, August 1993.

[19] R. L. Weaver. Mean and mean-square responses of a prototypical master/fuzzy structure. *Journal of the Acoustical Society of America*, 101(3):1441–1449, March 1997.

[20] M. Strasberg and D. Feit. Vibration damping of large structures induced by attached small resonant structures. *Journal of the Acoustical Society of America*, 99(1):335–344, January 1996.

[21] R. L. Weaver. The effect of an undamped finite degree of freedom "fuzzy" substructure: Numerical solutions and theoretical dissussion. *Journal of the Acoustical Society of America*, 100(5):3159–3164, November 1996.

[22] Robin S. Langley and Paul Bremner. A hybrid method for the vibration analysis of complex structural-acoustic systems. *Journal of the Acoustical Society of America*, 105(3):1657–1671, March 1999.

[23] J. J. McCoy and B. Z. Steinberg. Addressing complexity in structural acoustics - fuzzy structure and effective impedance theories. *Computers and Structures*, 65(3): 403–421, 1997.

[24] David A. Bies and Colin H. Hansen. *Engineering Noise Control, Theory and Practice.* E and F Spon, 2nd edition, 1997.

[25] Howard Anton. *Elementary Linear Algebra.* John Wiley and Sons, 4th edition, 1984.

[26] Werner Soedel. *Vibration of Shells and Plates.* Marcel Dekker Inc, New York, 1993.

[27] A. W. Leissa. *Vibration of shells.* SP-288. NASA, 1973.

[28] C. Ting-Kong. Design of an adaptive dynamic vibration absorber. Master's thesis, The University of Adelaide, 1999.

[29] Simon G. Hill and Scott D. Snyder. Design of an adaptive vibration absorber to reduce electrical transformer structural vibration. *Transactions of the ASME, Journal of Vibration and Acoustics*, 124(4):606–611, 2002.

[30] Simon Hill, Scott Snyder, and Ben S. Cazzolato. An adaptive vibration absorber. In *Proceedings of the Annual Australian Acoustical Society Conference, Adelaide, Australia, Nov 13-15*, pages 34–41, 2002.

[31] F. S. Tse, I. E. Morse, and R. T. Hinkle. *Mechanical Vibrations: theory and applications, 2nd edn.* Allyn and Bacon Inc., Boston, Massachusetts, 1995.

[32] Joseph E. Shigley. *Mechanical engineering design: first metric edition.* McGraw Hill, 1988.

[33] Warren C Young. *Roark's Formulas for Stress and Strain.* McGraw Hill International, 6th edition, 1989.